

**GAS CORROSION KINETICS OF  $\text{Fe}_2\text{O}_3$   
BY GRAIN BOUNDARY GROOVING**

by  
**Melissa R. Youree**

ProQuest Number: 10794544

All rights reserved

INFORMATION TO ALL USERS

The quality of this reproduction is dependent upon the quality of the copy submitted.

In the unlikely event that the author did not send a complete manuscript and there are missing pages, these will be noted. Also, if material had to be removed, a note will indicate the deletion.



ProQuest 10794544

Published by ProQuest LLC (2018). Copyright of the Dissertation is held by the Author.

All rights reserved.

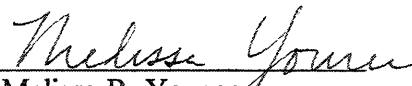
This work is protected against unauthorized copying under Title 17, United States Code  
Microform Edition © ProQuest LLC.

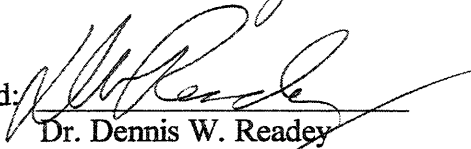
ProQuest LLC.  
789 East Eisenhower Parkway  
P.O. Box 1346  
Ann Arbor, MI 48106 – 1346

A thesis submitted to the Faculty and Board of Trustees of the Colorado School of Mines in partial fulfillment of the requirements for the degree of Master of Science (Metallurgical and Materials Engineering).

Golden, Colorado

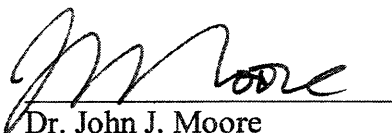
Date 11/13/00

Signed:   
Melissa R. Youree

Approved:   
Dr. Dennis W. Readey  
Thesis Advisor

Golden, Colorado

Date: 11/13/00

  
Dr. John J. Moore  
Professor and Head,  
Department of Metallurgical and  
Materials Engineering

## ABSTRACT

The active gas corrosion of ceramics is an understudied area that is becoming increasingly important to today's technology. However, few efforts have been made to model or characterize gaseous corrosion of ceramics. The purpose of this investigation was to determine the possibility of using grain boundary grooving as a means to study the kinetics of active gas corrosion of ceramics.

Iron oxide ( $\text{Fe}_2\text{O}_3$ ) was chosen as a model material and HCl as the corroding gas. Iron oxide was used because of its availability, ease in making dense ceramics, and previous experience has indicated a significant reaction between  $\text{Fe}_2\text{O}_3$  and HCl. Polycrystalline samples of  $\text{Fe}_2\text{O}_3$  were formed by typical ceramic powder processing techniques. Grain boundary grooves were formed in air and HCl/Ar atmospheres on a polished surface of the iron oxide samples. Samples were subjected to HCl in two different systems: a flow system and an ampoule-enclosed system. The surfaces exposed to the HCl flow system suffered severe preferential grain corrosion that made groove width measurements difficult. Thus, to prevent significant bulk material loss, sealed ampoules were used. In addition, samples were annealed prior to HCl-etching to minimize preferential attack at polish damaged surfaces. Grooves were measured with an atomic force microscope and surface/microstructural features were analyzed by scanning electron microscopy.

Experimental results were compared with literature data to assess their validity and attempt to identify the kinetic mechanisms of active corrosion at various times and

temperatures. Air-etched grain boundary grooves were remarkably close to Fe diffusion through solid phase predictions (oxygen would most likely diffuse through the gas phase). Similarly, the HCl-etched groove widths were within a factor of two of that predicted by gas diffusion control kinetics. However, the experimental data showed a stronger temperature dependence than gas diffusion predicts.

This research has successfully demonstrated that grain boundary grooving is a viable technique to predict active corrosion of ceramics, specifically at low corrosion rates.

## TABLE OF CONTENTS

	Page
ABSTRACT.....	ii
LIST OF FIGURES.....	vii
LIST OF TABLES.....	ix
ACKNOWLEDGEMENTS.....	x
<b>Chapter 1 INTRODUCTION</b>	
1.1 Objectives.....	1
1.2 Rationale.....	1
1.3 Scope of Research.....	2
<b>Chapter 2 THEORY</b>	
2.1 Thermodynamic Considerations.....	4
2.2 Kinetics.....	8
2.3 Rate Controlling Mechanism.....	12
2.3.1 Controlling Step Models.....	12
2.3.2 Gaseous Diffusion Control.....	13
2.3.3 Surface Reaction Control.....	14
2.4 Grain Boundary Grooving.....	14
<b>Chapter 3 LITERATURE REVIEW</b>	
3.1 Theoretical Models.....	17
3.2 Previous Experimental Work.....	19
3.2.1 Active Corrosion.....	19
3.2.2 Grain Boundary Grooving.....	20
<b>Chapter 4 EXPERIMENTAL METHOD</b>	

4.1 Sample Preparation.....	23
4.1.1 Powder.....	23
4.1.2 Pellet Densification/Preparation.....	23
4.1.3 Reactive/Inert Atmosphere Systems.....	26
4.2 Analytical Techniques.....	34
4.2.1 Atomic Force Microscope.....	34
4.2.2 Scanning Electron Microscope.....	34
4.2.3 Groove Width Measurement.....	35
4.2.4 Thermodynamic Calculations.....	35
 Chapter 5 RESULTS	
5.1 Experimental Results.....	41
 Chapter 6 DISCUSSION	
6.1 Groove Widths in Air.....	59
6.2 Groove Widths in HCl.....	63
6.2.1 Comparison of Calculated and Measured Groove Widths.....	63
6.2.2 Comparison of Grain Boundary Grooving and Weight Loss.....	67
 Chapter 7 CONCLUSIONS	
7.1 Summary.....	69
7.2 Recommendations for Future Work.....	70
 Chapter 8 REFERENCES.....	71
 Chapter 9 APPENDICES	

Appendix A: Error Analysis.....	76
Appendix B: Thermodynamic Calculations.....	79
Appendix C: Groove Measurement Data.....	80
Appendix D: Groove Images and Profiles.....	85



## LIST OF FIGURES

	Page
Figure 1: General Corrosion Rate Illustration.....	5
Figure 2: Product Partial Pressures for Fe <sub>2</sub> O <sub>3</sub> /Air System.....	6
Figure 3: Product Partial Pressures for Fe <sub>2</sub> O <sub>3</sub> /HCl Reaction.....	7
Figure 4: Concentration Profile of Fe <sub>2</sub> O <sub>3</sub> in HCl.....	10
Figure 5: Mullins Grooving Model.....	15
Figure 6: SEM of Fe <sub>2</sub> O <sub>3</sub> Powder.....	24
Figure 7: Particle Size Distribution Plot.....	25
Figure 8: Light Micrograph of Polished Fe <sub>2</sub> O <sub>3</sub> Surface.....	27
Figure 9: Air Atmosphere System Diagram.....	28
Figure 10: Furnace Temperature Profile.....	29
Figure 11: Light Micrograph of Cut Edge.....	31
Figure 12: Light Micrograph of Annealed Sample.....	32
Figure 13: Ampoule Gas Delivery Schematic.....	33
Figure 14: AFM Software Screen of Groove Measurement.....	36
Figure 15: Iron Chloride Partial Pressures for Fe <sub>2</sub> O <sub>3</sub> /HCl Reaction.....	39
Figure 16: Flow System, HCl-Etched Grooves at 873 K for 5 minutes.....	42
Figure 17: AFM 3-Dimensional Image of an Etched Surface in a HCl Flow System at 1073 K for 5 minutes.....	43
Figure 18: SEM Image of Non-Annealed, HCl-Etched Sample.....	45

Figure 19:	Closed System, HCl-Etched Grooves at 873 K for 10 minutes.....	46
Figure 20:	Closed System, HCl-Etched Grooves at 973 K for 10 minutes.....	47
Figure 21:	Closed System, HCl-Etched Grooves at 1073 K for 10 minutes.....	48
Figure 22:	Air Etched Sample at 1473 K for 30 minutes.....	49
Figure 23:	Air Etched Sample at 1473 K for 180 minutes.....	50
Figure 24:	Air Groove Width vs. Time for 1273 K Temperature.....	51
Figure 25:	Air Groove Width vs. Time for 1373 K Temperature.....	52
Figure 26:	Air Groove Width vs. Time for 1473 K Temperature.....	53
Figure 27:	Air Groove Width vs. Temperature for 30 min Etch Time.....	54
Figure 28:	Air Groove Width vs. Temperature for 60 min Etch Time.....	55
Figure 29:	Air Groove Width vs. Temperature for 180 min Etch Time.....	56
Figure 30:	Air Groove Width vs. Temperature for 540 min Etch Time.....	57
Figure 31:	HCl Groove Width vs. Temperature for 10 min Etch Time.....	58
Figure 32:	Comparison of Calculated and Experimental Air Groove Data for 180 minutes.....	62
Figure 33:	Comparison of Calculated and Experimental HCl Groove Data for 10 minutes.....	66

## LIST OF TABLES

	Page
Table 1: Mullins Models for Various Rate Controlling Mechanisms.....	18
Table 2: Experimental Width Compared to Analytical Width for Air Atmosphere.....	60
Table 3: Experimental Width Compared to Analytical Width for an HCl Atmosphere.....	64

## ACKNOWLEDGEMENTS

I would like to show my great appreciation towards my advisor, Dr. Dennis Readey, on his efforts to guide and support me through my research as well as his generosity of time for our many non-thesis conversations.

I would like to thank the National Science Foundation (NSF), Division of Materials Research, for their financial backing

I want to thank the members of my thesis committee, Dr. Kelly Miller and Dr. Mark Eberhart, for their help throughout this process. A big thanks is in order to Alice Jensen for her professional and personal counseling with my graduate *and* undergraduate studies. I would also like to thank Steve Donalson, Scott Pawelka and Bob McGrew for their good nature and many efforts to help my experiments and analysis along its way. A special thanks goes to Catherine Tuell who has been my lab/office partner and good friend over my graduate studies.

I owe a huge thank you to my entire family for their encouragement and confidence in me. Most of all, I am greatly indebted to my parents, Lanny and Judy, whom because of them I have found myself where I am today.

## CHAPTER 1

### INTRODUCTION

#### 1.1 Objective

The objective of this research is to ascertain the fundamental degradation mechanisms and the rate-controlling steps in active gaseous corrosion of ceramics (where all products are gaseous species). Once the mechanism of degradation is understood, in principle, the composition and/or the structure of a ceramic may be modified to minimize degradation. If this cannot be accomplished, a comprehension of the mechanisms can render guidance for restricting a specific ceramic's use in a given environment.

#### 1.2 Rationale

This study focuses on corrosion of ceramics, specifically  $\text{Fe}_2\text{O}_3$ , in halogen-containing gases such as HCl. The rationale behind this approach is two-fold. First, more ceramics corrode in halogens than in either reducing or oxidizing environments allowing for an easy comparison between a wide scope of different ceramic materials (which might not otherwise corrode under similar conditions). Second, since the equilibrium product gas pressures produced in reactions with HCl are expected to be high over a large temperature range, the transition from diffusion-controlled kinetics to surface reaction-controlled kinetics should be possible to observe. As a result, the research will lead to an understanding of the environmental conditions in which surface reaction or mass transfer controls corrosion.

The halogen corrosion of ceramics is becoming ever more important in a large number of industrial areas. Many chemicals are processed in halogen environments at high temperatures, which promotes refractory corrosion (e.g.  $\text{TiO}_2$  powders for paint pigments,  $\text{SiO}_2$  for thickening agents, and fluorocarbons). Also, ceramics are used for supports and fixtures for silicon wafers during integrated circuit processing where many of the steps are executed in halogen-containing gases (frequently at high temperatures). The behavior of ceramics in burners, combustors, and other high temperature components for waste incinerators is becoming of increasing importance. The incineration of polyvinyl chloride and other polymers in the waste stream produce halogens in the combustion gases. [1] Lastly, high temperature systems will always pick up an amount of NaCl from the atmosphere, when operating near salt water, generating various halogen gases causing a certain level of degradation.

### 1.3 Scope of Research

Little data exist on active gaseous corrosion of ceramics. However, the data that do exist show that gas diffusion of the product gases away from the reaction surface governs the rate of reaction at high temperatures. From this, the rate of corrosion can be predicted from the kinetic theory of gases and thermodynamic data.

The method being used is to compare, when possible, experiments with existing models. Thermodynamic calculations predict that the corrosion of most oxide ceramics (as well as nitride and carbide ceramics) at high temperatures will be regulated by

diffusion of the reaction product gases away from the reaction surface. In this case, the reaction kinetics can be easily modeled and compared with experimental data.

## CHAPTER 2

### THEORY

#### 2.1 Thermodynamic Considerations

Chemical processes follow two forms of reaction sequences: concurrent reactions or 'in parallel' and successive reactions or 'in series'. Both reaction sequences yield different rate controlling steps. For instance, in parallel processes, the fastest reaction is rate controlling, while in series processes, the slowest reaction is rate controlling. Active corrosion is a series process and is depicted in Figure 1. As demonstrated in Figure 1, at higher temperatures, gas diffusion is the rate controlling step while, at low temperatures, the surface reaction is rate controlling. This is the case because surface reactions are usually exponentially temperature dependent while gas diffusion is weakly temperature dependent.

The pressures of gaseous species over  $\text{Fe}_2\text{O}_3$  in an air atmosphere are very low until extraordinarily high temperatures are reached. Therefore, gas corrosion in air is unlikely. Conversely, there are many possible reactions in the active corrosion of iron oxide in an HCl gas atmosphere. Their product partial pressures were calculated with a commercial program and are plotted in Figures 2 and 3 against temperature (see Section 4.2.4 for details). In these plots, the following assumptions are made: i) 1 atm total pressure, and ii) equilibrium conditions ( $\text{Fe}_2\text{O}_3$  activity is 1). As can be seen in Figure 3, the two most stable and dominant products within the experimental temperature range are



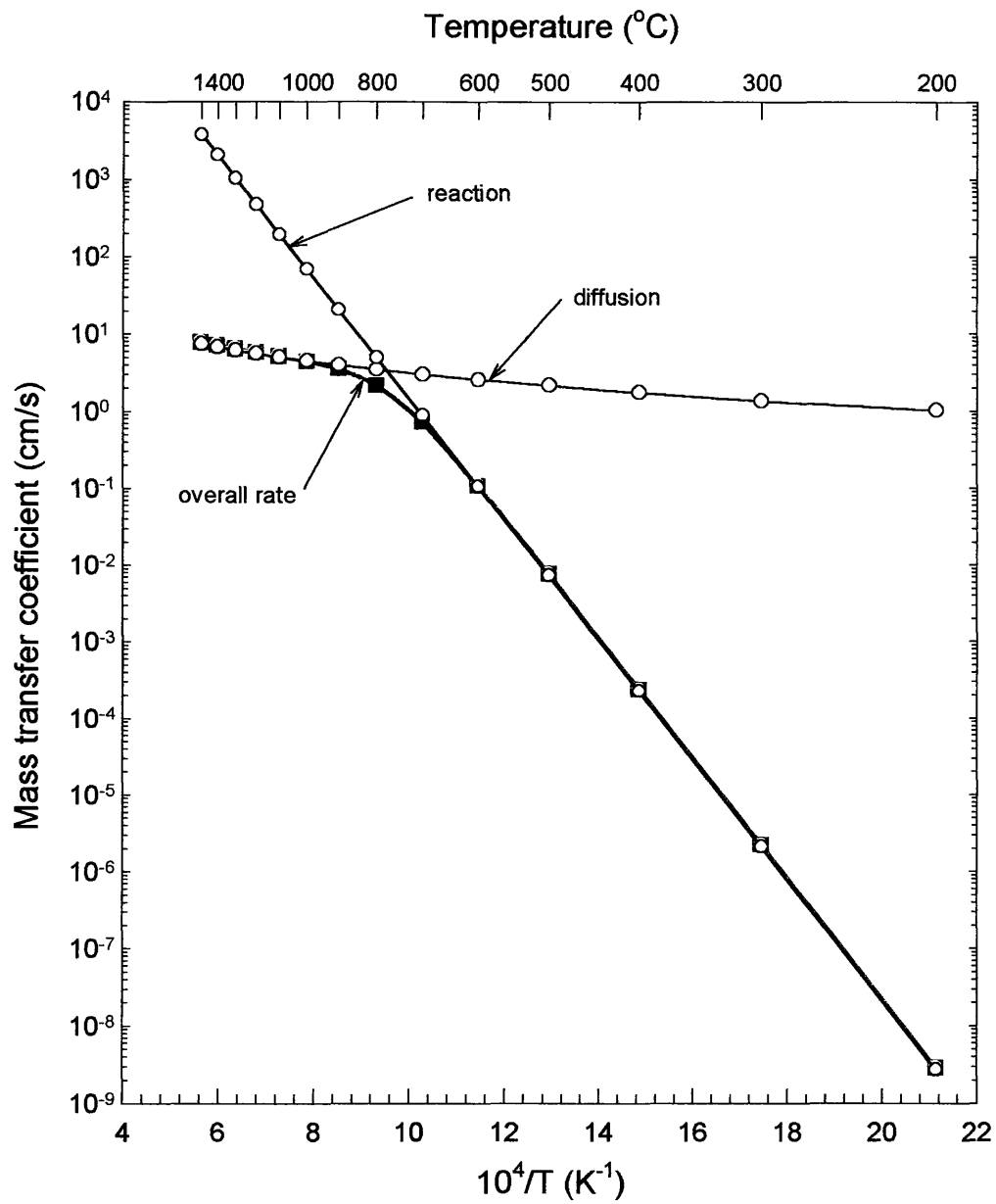


Figure 1: General Corrosion Rate Illustration for a Gas-Solid Reaction.

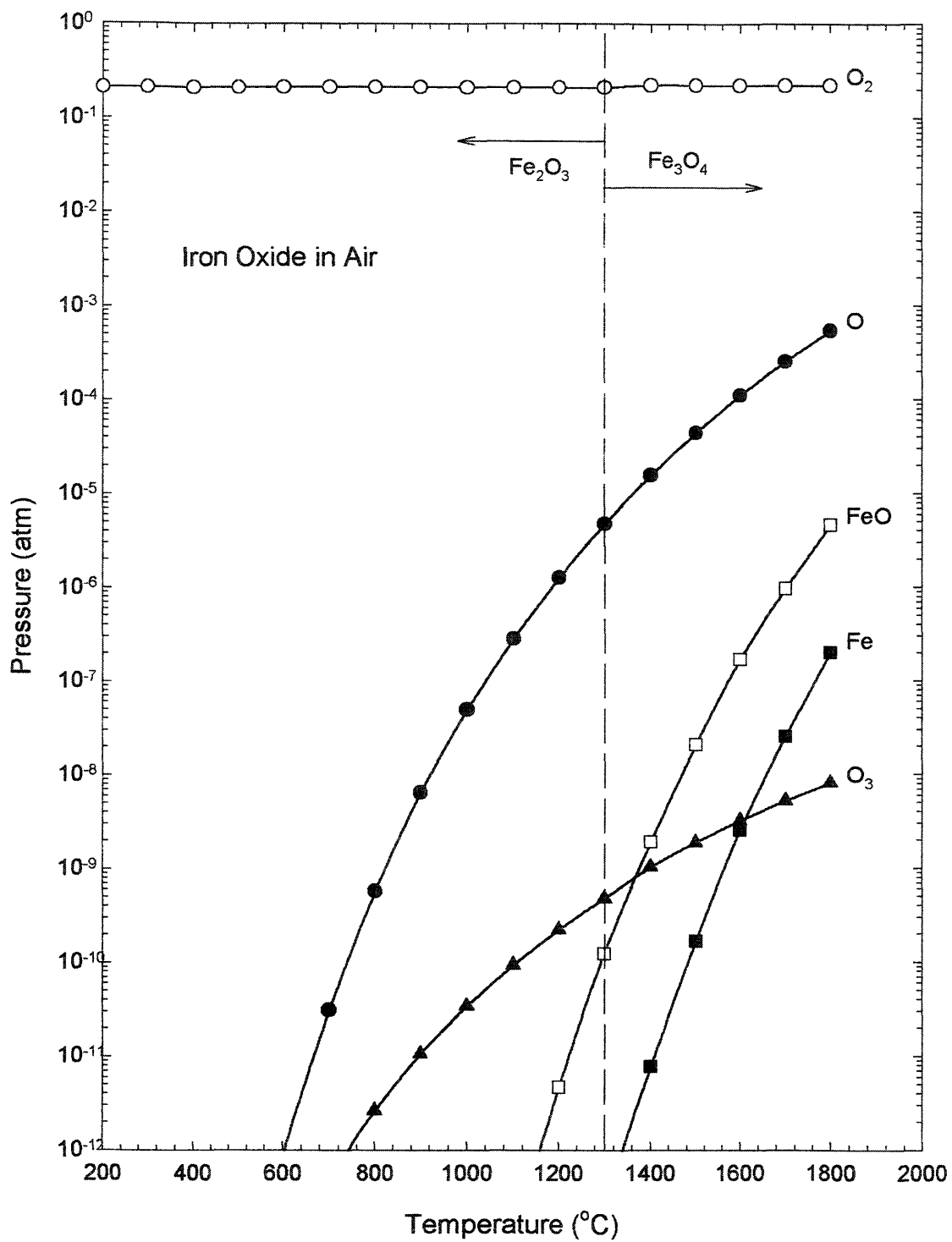


Figure 2: Calculated Product Partial Pressures for  $\text{Fe}_2\text{O}_3/\text{Air}$  System

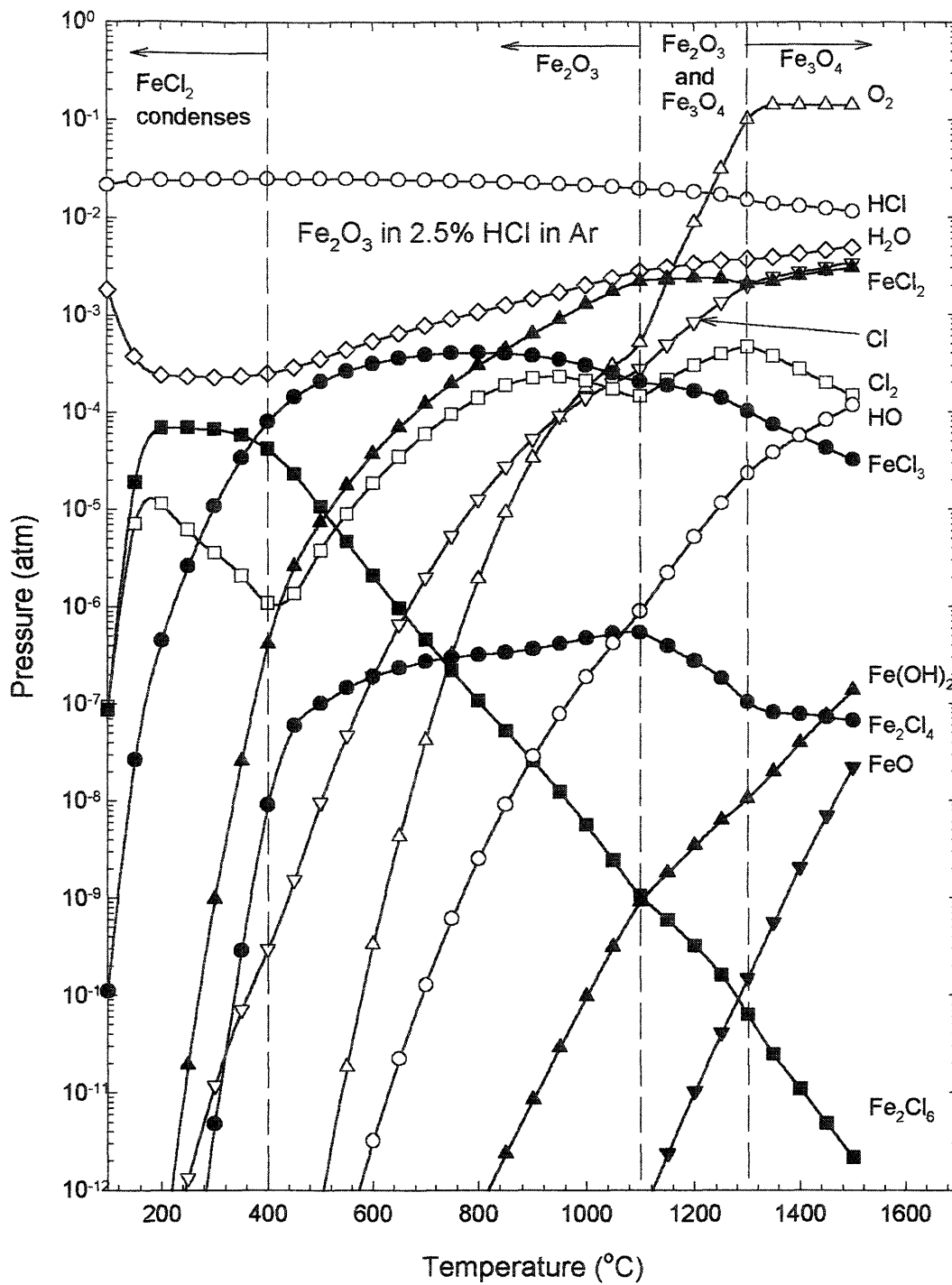
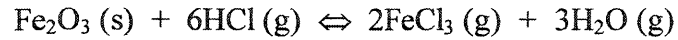


Figure 3: Calculated Product Partial Pressures for  $\text{Fe}_2\text{O}_3$  in 0.025 atm HCl in Ar.

H<sub>2</sub>O (g) and FeCl<sub>3</sub> (g). Thus, for all practical purposes, the reaction being dealt with in this study is:



$$K_e = [ p(\text{FeCl}_3)^2 p(\text{H}_2\text{O})^3 ] / [ a(\text{Fe}_2\text{O}_3) p(\text{HCl})^6 ] = \exp(\Delta S^\circ/R) \exp(-\Delta H^\circ/RT)$$

## 2.2 Kinetics

For most gas-solid reactions, the flux density in the gas phase can be represented by [2]:

$$N_i = J_i + v c_i \text{ [mol/cm}^2\text{/s]}$$

where  $N_i$  is molar flux relative to stationary coordinates,  $J_i$  is the diffusion or reaction flux in moving coordinates,  $c_i$  is the molar concentration of species  $i$ , and  $v$  is the velocity of the gas phase with respect to stationary coordinates. Two terms make up the gas velocity: i) the actual gas-solid interface motion [3] and ii) the net destruction/creation of moles of gas during the reaction [4, 5]. The gas-solid interface motion is negligible in the system being used here. However, because there are 5 moles of gas product (2FeCl<sub>3</sub> + 3H<sub>2</sub>O) for every 6 moles of gas reactant (6HCl), there is an accumulated flow of gas to the solid surface that will influence the concentration profiles and the rate of material degradation. Thus the velocity is modeled as:

$$v = \Sigma N_i / c$$

where  $c$  is the total concentration in the phase, which is constant (at a constant pressure). However, the gas product pressures and resulting fluxes are small and, as a result, the net gas velocity can be ignored. In other words,  $N_i = J_i$ .

Consequently, the rate of corrosion can be represented by the corrosion flux density,  $J(\text{Fe}_2\text{O}_3)$ . Fick's first law, shown below, is the starting point for analysis of diffusional mass transfer, and hence, corrosion [6]:

$$J_i = -(1 / A) (dm_i / dt) = D_i (dc_i / dx)$$

where  $J_i$  is mass flux of species  $i$ ,  $A$  is the area normal to the direction of diffusion,  $(dm_i/dt)$  is the rate of change of mass of species  $i$ ,  $D_i$  is the diffusion coefficient of species  $i$  in the surrounding medium, and  $(dc_i / dx)$  is the concentration gradient parallel to the direction of diffusion. Figure 4 is an illustrated explanation of the components of Fick's first law and general reaction steps that occur in active corrosion.

Because the concentration profile from the solid surface to the fluid surrounding is often not well defined, Fick's first law can be rewritten as:

$$-(dm_i / dt) = S D_i (C_i - C_i^0)$$

where  $S$  is the shape factor (dependent on the geometry of the system),  $C_i$  is the concentration of species  $i$  in the surrounding fluid, and  $C_i^0$  is the concentration of species  $i$  at the solid surface. This study deals with a planar interface between the solid and the fluid, thus,  $A / \delta$  can be substituted for  $S$  (where  $\delta$  is the boundary layer width).

The boundary layer is the 'film' between the solid surface and the fluid medium where a concentration gradient is observed. (See Figure 4.) Its thickness depends on the geometry of the solid and the fluid's properties and velocity as seen in the following equation [7, 8]:

$$\delta = \delta_0 + 3.09 \text{Re}^{-1/2} \text{Sc}^{-1/3}$$

## Concentration Profiles for $\text{Fe}_2\text{O}_3$ in HCl

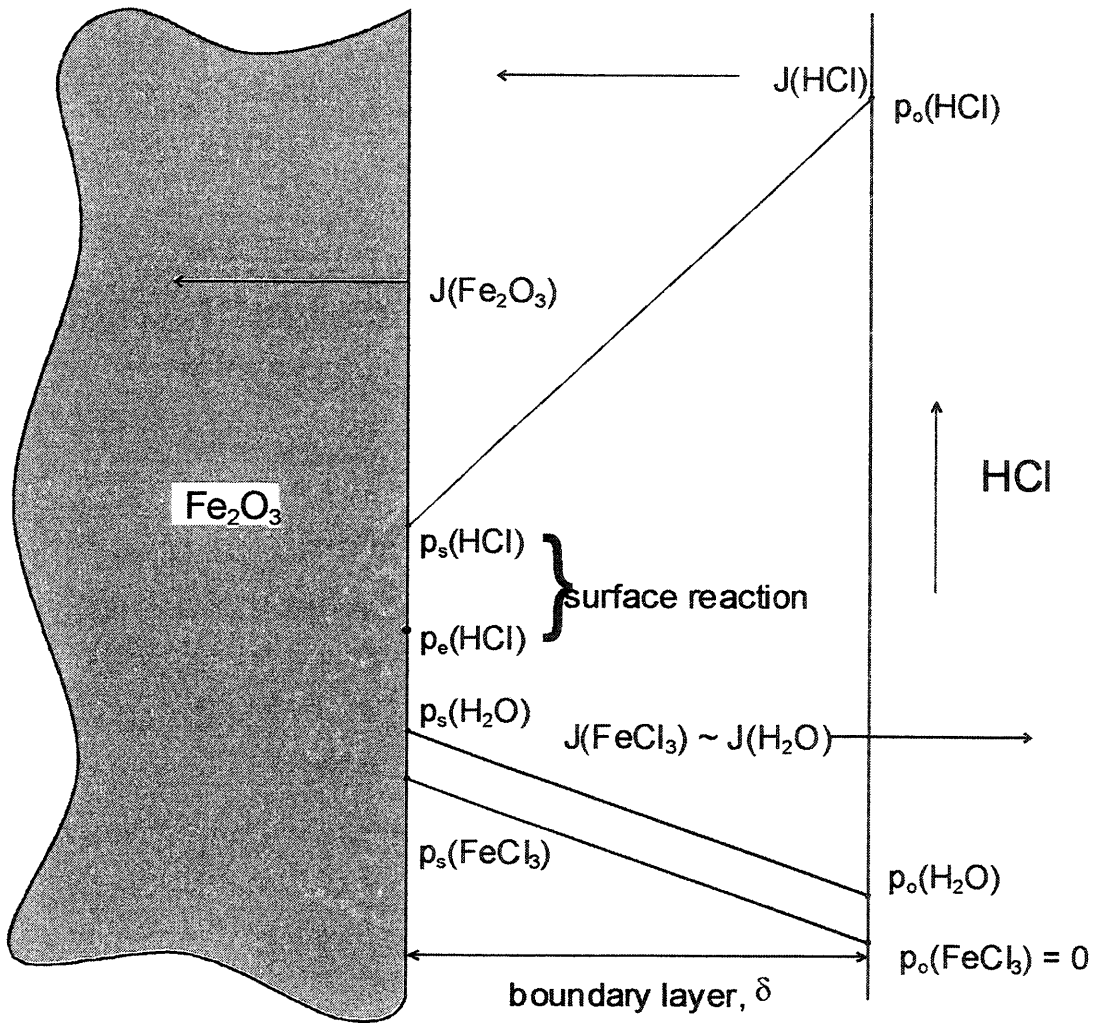


Figure 4: Concentration Profile of  $\text{Fe}_2\text{O}_3$  in HCl

where  $\delta_o$  is the boundary layer for diffusional mass transport in a stagnant fluid,  $Re$  is Reynold's number, and  $Sc$  is the Schmidt number. The Schmidt number is simply the kinematic viscosity of the fluid divided by the diffusion coefficient.

From the modified Fick's first law seen above, the following expression can be found for the mass flux:

$$J_i = (D_i / \delta) (C_i - C_i^o)$$

where  $(D_i / \delta)$  is equal to the mass transfer coefficient,  $h_i$ .

The mass transfer coefficient ( $h$ ) is:

$$h = D Sh / d RT \quad [\text{mol/cm}^2/\text{s}/\text{atm}]$$

where  $D$  is gas diffusion coefficient ( $\text{cm}^2/\text{s}$ ),  $Sh$  is Sherwood coefficient and  $d$  is a characteristic distance for the geometry. The Sherwood coefficient is a term that deals with the effect of convective gas flow on mass transfer. Therefore, it is desirable to have very low flow rates so as that  $Sh \cong 2.0$  (essentially pure diffusion conditions). Also, the mass transfer coefficients,  $h$ , are solely dependent on interdiffusion coefficients and the boundary layer at the solid surface will be  $d/2$  ( $d$  is the sample diameter).

For the purpose of the system at hand, the fluxes for the reaction can be expressed in terms of the various gas pressures (which includes the possibility of a surface reaction,  $J_s$ ):

$$J(\text{HCl}) = -h(\text{HCl}) [ p_o(\text{HCl}) - p_s(\text{HCl}) ]$$

$$J_s(\text{HCl}) = k [ p_s(\text{HCl}) - p_e(\text{HCl}) ]$$

$$J(\text{FeCl}_3) = -h(\text{FeCl}_3) [ p_o(\text{FeCl}_3) - p_s(\text{FeCl}_3) ]$$

$$J(\text{H}_2\text{O}) = -h(\text{H}_2\text{O}) [ p_o(\text{H}_2\text{O}) - p_s(\text{H}_2\text{O}) ]$$

where  $p_o$  is pressure in the gas phase far from the solid surface (atm),  $p_s$  is gas-solid interface pressure (atm),  $p_e$  is equilibrium pressure (atm),  $J_s$  is surface reaction flux, and  $k$  is surface reaction rate constant.

Because the above fluxes are first order and in series, then

$$J(\text{H}_2\text{O}) = 2 J(\text{FeCl}_3) = -6 J(\text{HCl}) = -6 J_s(\text{HCl}) = -J(\text{Fe}_2\text{O}_3)$$

### 2.3 Rate Controlling Mechanism

As illustrated in Figure 4, solid-gas reactions normally have one of the subsequent rate-controlling steps: i) mass transfer to the solid surface, through the boundary layer, ii) boundary layer heat transfer, iii) adsorption of gas reactants on the solid surface, iv) surface diffusion of the reactants or products to the reaction site, v) the actual gas-solid reaction, and vi) product desorption from the solid surface. [9] Diffusion controlled corrosion will be governed by step (i). Surface reaction controlled will have one of steps (ii) through (vi) regulating the process.

#### 2.3.1 Controlling Step Models

Corrosion rates and their temperature dependence, as mentioned earlier, can be dictated by one of two reaction steps, gas transport or surface reaction. Gas diffusion controlled processes have been proven easy to model based on thermodynamic calculations and known diffusion values. [10] On the other hand, surface reactions have many possible rate-controlling steps. [11] For that reason surface reactions normally have a large amount of ambiguity in their interpretation.



### 2.3.2 Gaseous Diffusion Control

Under gas diffusion (of products and/or reactants) controlled corrosion, two scenarios should be considered. In the first case the reaction could go to completion (which seems to be the case with metals in halogen atmospheres [12]). The diffusion of reactants to the reaction surface is rate controlling and the temperature dependence relies on the mass transfer coefficient for gas reactant diffusion,  $h(\text{HCl})$ ; because  $D \propto T^{3/2}$ ,  $h \propto T^{1/2}$  (which is a very weak temperature dependence). In the event that empirical data is not accessible, the mass transfer coefficients can be computed from the kinetic theory of gases. [13]

In situations where the equilibrium constants are small, the reaction does not go to completion and, as a result, the product gas pressures are low. Thus, the diffusion of the product gases from the reaction surface is rate-controlling and the temperature dependence of the reaction rate comes from the equilibrium constant  $K_e$ . This dependency yields an easy comparison between quantitative experimental data and theoretical models because the values of  $\Delta G^\circ$ ,  $\Delta H^\circ$ , and  $\Delta S^\circ$  can be obtained from existing thermodynamic data for most reactions. [14]

Consequently, a quantitative comparison can be made between the rates of corrosion and those calculated from the model. In addition, a quantitative comparison can be made for the observed activation energy and the enthalpy. Such transport-controlled reactions are some of the few in which thermodynamics leads directly to kinetics.

### 2.3.3 Surface Reaction Control

If, for instance, the surface reaction dominates the rate, the temperature dependence rests on the surface reaction rate constant ( $k$ ).

$$k = k_0 e^{-Q/RT}$$

Since so many surface reaction step possibilities are not well understood, it is very difficult to predict  $k$ .

If surface reaction control is indicated by functional dependencies, then further comparison between a model and experiment becomes more difficult. Except in rare cases, it is virtually impossible to experimentally observe the activated state at the atomic or molecular level. Even for sublimation [15], which serial reaction step controls the rate is not clear. Therefore, the kinetic mechanism can only be inferred from agreement between experimental and model dependency of the reaction rate constant with experimental variables. Nevertheless, great progress has been made with this “macroscopic” [16] approach to understand the mechanisms of both homogeneous and heterogeneous chemical reactions. [17, 18, 19]

### 2.4 Grain Boundary Grooving

Grain boundary grooves are formed when temperatures reach a point where mass transport mechanisms are working ( $T / T_m > 0.5$ ). [20] At such temperatures, the grooves are created along grain boundaries where they intersect the surface to equilibrate surface and grain boundary energies. The following equation demonstrates this energy balance (see Figure 5):

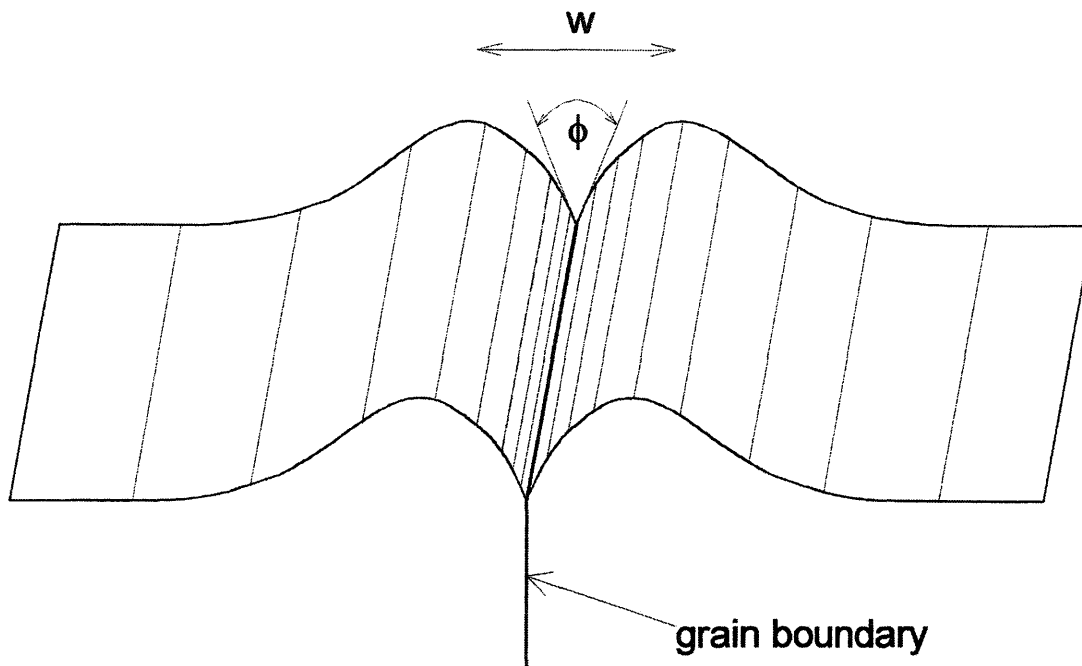


Figure 5: Mullins Grooving Model [3, p.354]

$$\gamma_{ss} / \gamma_{sv} = 2 \cos \phi / 2$$

where  $\gamma_{ss}$  is the grain boundary energy,  $\gamma_{sv}$  is the surface energy and  $\phi$  is the groove angle.

The kinetics of the groove formation will determine the shape and width of the groove.

[10, 21] If diffusion through the vapor phase controls groove growth, then the width of the groove,  $w$ , is given by [21]:

$$w^3 = 125 (\Omega / RT)^2 D \gamma p_s t$$

where  $w$  is the groove width,  $\gamma$  is the surface energy,  $\Omega$  is the molar volume,  $t$  is time, and the other terms were previously defined.

Grain boundary grooving kinetics depend on the experimental variables in essentially the same way as gas corrosion. [10, 21, 22] Consequentially, grain boundary grooving can be used to monitor particularly low corrosion rates at either low temperatures or low HCl gas pressures. In point of fact, the first model of grain boundary grooving kinetics was created to establish how boundary grooving would effect weight loss during vaporization of metals. [10]

Also, if grooving kinetics follow gas phase diffusion, the surface free energy,  $\gamma$ , can be determined from grooving kinetics. This is, in part, because  $D$  and  $p_s$  can be calculated from kinetic theory and thermodynamics. Therefore, from the surface free energy and the angle,  $\phi$ , shown in Figure 5 at the root of the groove, fixed thermodynamically, the grain boundary energy can be ascertained. [22]

## CHAPTER 3

### LITERATURE REVIEW

The corrosion of ceramics and ceramic composites in high temperature reactive gases is an important limitation to the use of these materials in advanced systems. Unfortunately, the fundamental mechanisms controlling the gaseous corrosion of ceramics are not well understood except in a few isolated cases. [50]

This section provides a brief overview of others' efforts to better grasp ceramic corrosion kinetics.

#### 3.1 Theoretical Models

As the forerunner in research for grain boundary grooving, Mullins first formed a model in the 1950's. He proposed that grooving at grain boundary intersections with surfaces occurred in order to equilibrate the difference in energies between the two surface tensions (of neighboring grains) and the grain boundary energy, thus forming an equilibrium angle (which was discussed in the previous section). [10]

Mullins mathematically modeled groove profiles for evaporation-condensation and surface diffusion mechanisms. [10] He found that, although equilibrium angles are quickly achieved, grooves are forced to deepen because the evaporation and surface diffusion mechanisms tend to flatten the ridges produced from the groove (disturbing the equilibrium angle). He later developed other groove equations based on volume diffusion mechanisms. [21] Surface scratch smoothing [23], flattening of a nearly planar surface [24], linear facet growth [25], grain boundary motion [26], and the effects of

stress on grooving [27] were likewise examined by Mullins under analogous processes.

All these models were established with the following assumptions made:

- 1) the system is closed and in quasi-equilibrium with its vapor
- 2) the properties of the interface are independent of its orientation
- 3) the initial groove slope is essentially flat
- 4) crystalline imperfections are ignored.

Although the second and fourth assumptions are rarely the case, for all practical purposes, the models still hold somewhat valid and provide for a less complicated view/comparison of the kinematic effects of different rate-controlling mechanisms.

Aldrich compiled a table that lists the models for an easy comparison. [28] The equations are in the form of groove width ( $w$ ) as a function of time ( $t$ ):

$$w \propto A t^n$$

where  $A$  is a constant based on fundamental material properties and  $n$  is an exponent based on the transport mechanism.

Table 1: Mullins Grooving Models for Different Rate Controlling Mechanisms [28]

Mechanism	Constant (A)	Exponent (n)
Viscous flow	$\gamma_s / 2\mu$	1
Evaporation-condensation	$p_o \gamma_s \Omega^2 / (2\pi M)^{1/2} (kT)^{3/2}$	1/2
Volume diffusion (in the solid)	$125 D_v \gamma \Omega / kT$	1/3
Volume diffusion (external phase)	$125 C_o \gamma_s \Omega^2 D / kT$	1/3
Surface diffusion	$4.6 D_s \gamma_s \Omega^2 v / kT$	1/4

## 3.2 Previous Experimental Work

### 3.2.1 Active Corrosion

More and more, active corrosion of ceramics is becoming an increasingly popular science due to industrial demand. In past research, active corrosion has been measured by bulk weight loss of a specimen through gravimetry methods or simple post-corrosion weight analysis. Case in point, D. Park, M. McNallan, C. Park and W. Liang examined active corrosion of silicon carbide by way of thermogravimetric analysis. [29] By measuring a weight change as a function of time, they could observe a variation in corrosion rates based on flow properties and oxygen/chlorine concentrations. Nonetheless, a time dependency was not established and the kinetic, rate-controlling mechanisms driving the corrosion were not investigated in depth.

Subsequently, Sickafoose and Readey investigated gaseous corrosion of silicon carbide in an  $H_2$ - $H_2O$  atmosphere using a microbalance. [30] Here, the rate of weight loss was compared to a kinetic model. By combining three weight-loss rates based on different regions of the SiC samples, the external region, the  $SiO_2$  layer, and the SiC core, they contrived a model that yielded calculated results within two orders of magnitude of their experimental data.

In 1996, Say and Liu studied active corrosion mechanisms of SiC in  $V_2O_5$  and  $Na_2SO_4$  environments. [31] The weight loss was calculated using pre- versus post-corrosion bulk weight measurements.

More recently, Readey compared mechanisms controlling “microstructural and strength degradation of composites in reactive atmospheres” through the reduction of  $TiO_2$ - $NiTiO_3$  and the oxidation of MgO-SiC and MgO-carbon. [p.312, 32] Readey also

explored the gaseous corrosion of ceramics in halogen atmospheres through an in depth examination of the thermodynamic behavior of active corrosion for single and multi-component oxides. [33]

### 3.2.2 Grain Boundary Grooving

One of the first experimental studies on grain grooving of ceramics was carried out by Readey and Jech, who investigated the growth kinetics of grooves in a NiO bicrystal. [22] The controlled bicrystal allowed for less error due to surface energy anisotropies. A diamond stylus (with a radius of  $1\mu\text{m}$ ) profilometer was used to traverse across the grain boundary and decipher the groove profile. Although the radius of the stylus was a hindrance, the data agreed well with the volume diffusion mechanism model for grooving kinetics.

Interference optical microscopy was employed by Robertson in order to observe the thermal grooving of Si, SiC, and  $\text{Si}_3\text{N}_4$ . [34, 35] The Si and SiC were etched under vacuum conditions ( $\sim 10^{-3}$  Pa) while the  $\text{Si}_3\text{N}_4$  was etched in a 94%  $\text{N}_2$  – 6%  $\text{H}_2$  gas mixture ( $\sim 10^5$  Pa). Results showed that Si grooves were formed via surface diffusion with an activation energy of  $\sim 298$  kJ/mol. Silicon carbide samples had very little grooving, but exhibited texturing when exposed to temperatures of  $1900^\circ\text{C}$ . Finally, the  $\text{Si}_3\text{N}_4$  was also textured; however, the grooves were more evident than those in SiC and seemed to be formed by an evaporation process (which no other study has shown since). The kinetics of evaporation was later found could be avoided by packing the samples in their parent powders. It should be noted that these conclusions are only based on two data points per material.



The Metal Reference Line (MRL) technique is another, more accurate, way to profile grooves as demonstrated by Handwerker, Dynys, Cannon and Coble who compared MRL with optical interferometry. [36] MRL deposits a metal line onto a thermally grooved surface using photolithography where it conforms to the contours of the grain-boundary groove. This metal line furnished a high-contrast reference line for gauging groove angles ( $\phi_s$ ) by a scanning electron microscope (SEM). Handwerker, Dynys, Cannon and Coble used this technique to measure grooves formed on  $\text{Al}_2\text{O}_3$  and  $\text{MgO}$ . [37] As shown in the below equation, measuring the groove angles can yield to relative energy calculations:

$$\gamma_{\text{gb}} = 2\gamma_s \cos(\phi_s/2)$$

where  $\gamma_{\text{gb}}$  is the grain boundary energy and  $\gamma_s$  is the surface free energy. Tsoga and Nikolopoulos, similarly, employed the MRL technique to measure the groove angles and widths of  $\text{Al}_2\text{O}_3$  etched in air, under vacuum ( $\sim 10^{-3}$  Pa). [38] They found that surface diffusion is rate-controlling for temperatures ranging between 1200 K and 1800 K. The surface diffusion coefficient ( $D_o$ ) and activation energy (Q) were also calculated from the data, which were  $D_o = 0.48 \text{ cm}^2/\text{s}$  and  $Q = 256 \text{ kJ/mol}$  (for low temperatures).

Aldrich and Readey analyzed grain boundary grooving of  $\text{Al}_2\text{O}_3$  and  $\text{Fe}_2\text{O}_3$  in an air and HCl atmosphere. [39] Atomic force microscopy (AFM) analysis was practiced to measure groove widths and observe groove angles. The AFM scanned a sample surface with silicon cantilever tips and the groove was profiled by measuring the deflection in the tip. The widths in air were, as expected, much narrower than those found in HCl. The data lent itself to being surface reaction controlled. Furthermore, Jin, Shimada and Ikuma

## CHAPTER 4

### EXPERIMENTAL METHOD

#### 4.1 Sample Preparation

##### 4.1.1 Powder

Submicron, high-purity  $\text{Fe}_2\text{O}_3$  powder was used in the experiments. The initial powder can be seen in the SEM micrograph shown in Figure 6 and the particle size distribution is displayed in Figure 7.

Uniform powder processing methods were employed to insure all samples start with identical structures and properties. This 'green state processing' has proven to be a very consequential step(s) in the creation of ceramics.

##### 4.1.2 Pellet Densification/Preparation

Green body 'pellets' were formed by uniaxially pressing 1.8 grams of  $\text{Fe}_2\text{O}_3$  powder in a 1.27 cm (0.5 in.) diameter stainless steel die to a pressure of 49 MPa (7100 psi), without die lubricant. Typical green body densities are on the order of 45-55% of theoretical. The  $\text{Fe}_2\text{O}_3$  pellets were stored in a drying oven at 100 °C for a minimum of 3 hours to remove any excess water. The pellets were then sintered in air at 1200 °C for 3 hours to greater than 96% theoretical density. The excess time provided for sintering was for grain growth purposes.

Upon densification of the  $\text{Fe}_2\text{O}_3$  pellets, the samples were ground and polished starting with a 600-grit paper leading to a series of diamond pastes ranging from 6  $\mu\text{m}$  to

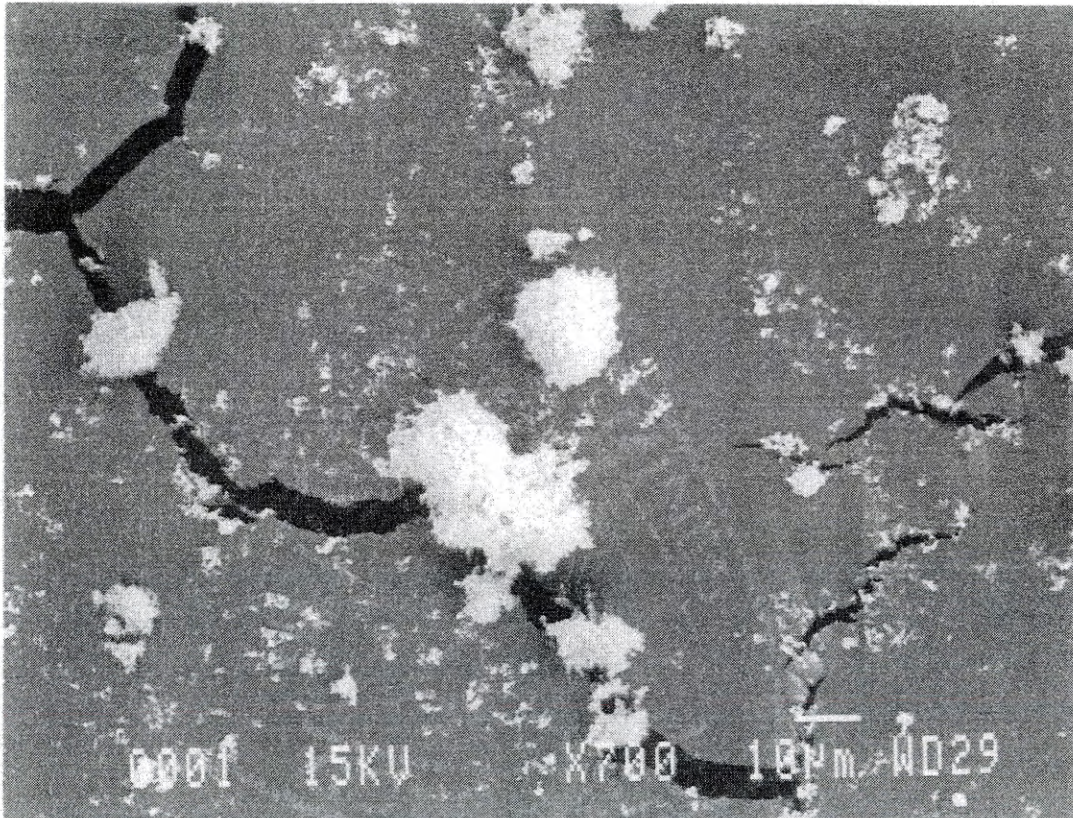


Figure 6: SEM Image of Fe<sub>2</sub>O<sub>3</sub> Powder

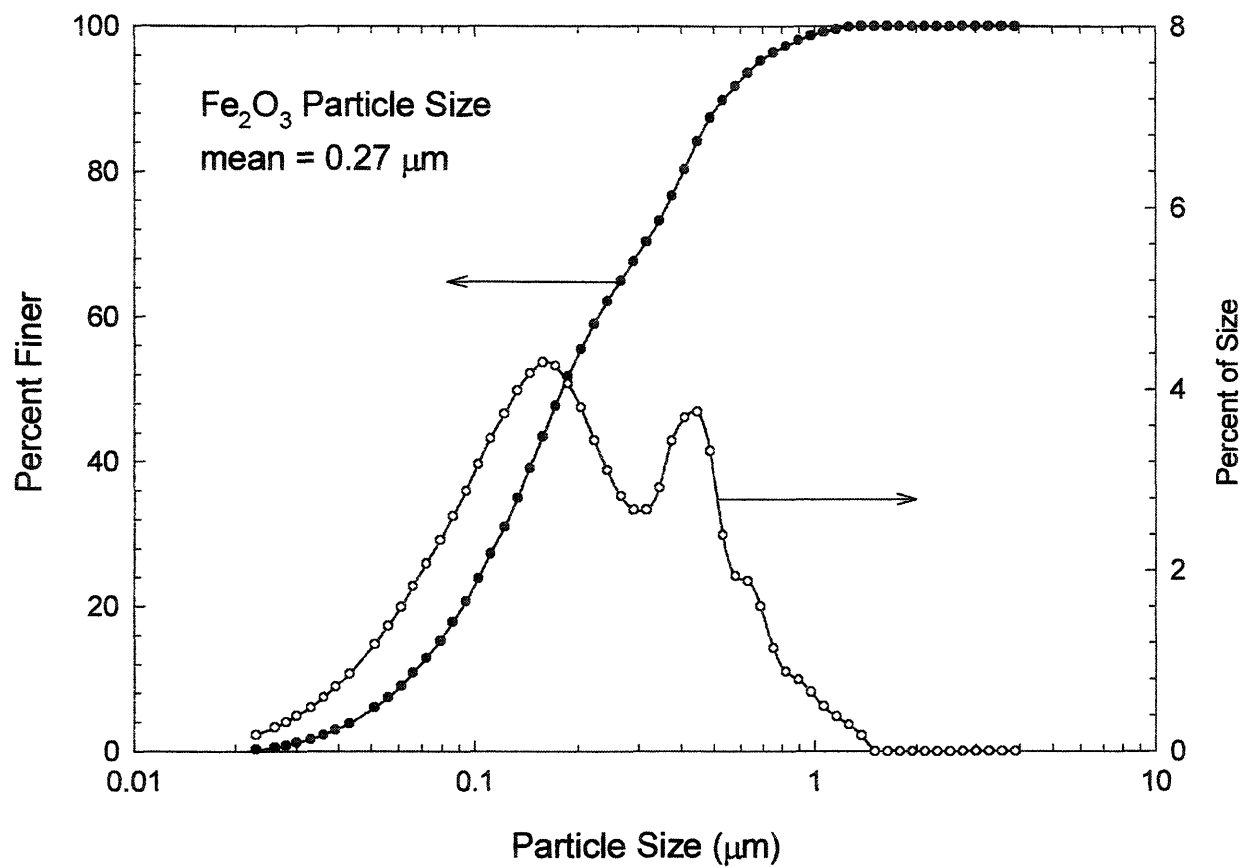


Figure 7: Fe<sub>2</sub>O<sub>3</sub> Particle Size Distribution Plot [Jeff Phillips, Coors Tech]

0.25  $\mu\text{m}$ . Pellets were thoroughly cleaned before and after each polishing step with distilled water and methanol. Once polishing was completed (see Figure 8), the samples were placed in a drying oven at 100 °C for a minimum of 12 hours, again, to eliminate any water.

#### 4.1.3 Reactive/Inert Atmosphere Systems

Samples were thermally etched in one of two atmospheres, air and 5% HCl – 95% Ar. In the air environment, samples were situated in a closed-ended, high-purity alumina furnace tube, where the open end was exposed to the atmosphere (only fiberfax insulation was placed between the atmosphere and the tube environment). Figure 9 illustrates the schematic of the air atmosphere system and Figure 10 is a graphical representation of the furnace temperature during its ramp up to etching temperature, hold, and cool down.

Two different approaches were used for the reactive atmosphere tests. The first approach entailed as-polished,  $\text{Fe}_2\text{O}_3$  pellets centered in an open-ended alumina tube furnace. The tube was sealed at both ends with teflon caps and neoprene gaskets (which will not react with HCl). Next, the tube was flushed (with argon) and pumped down to vacuum pressure several times. A constant flow of 23.5 mL/min was then allowed through the tube via high accuracy flowmeters. This gave a very low gas velocity in the furnace tube and, for all practical purposes, the gas could be considered stagnant. The atmosphere in the tube was 5% HCl and 95% Ar with a constant total pressure of 1 atm. The tube furnace was heated to the given temperature and held for a given time.

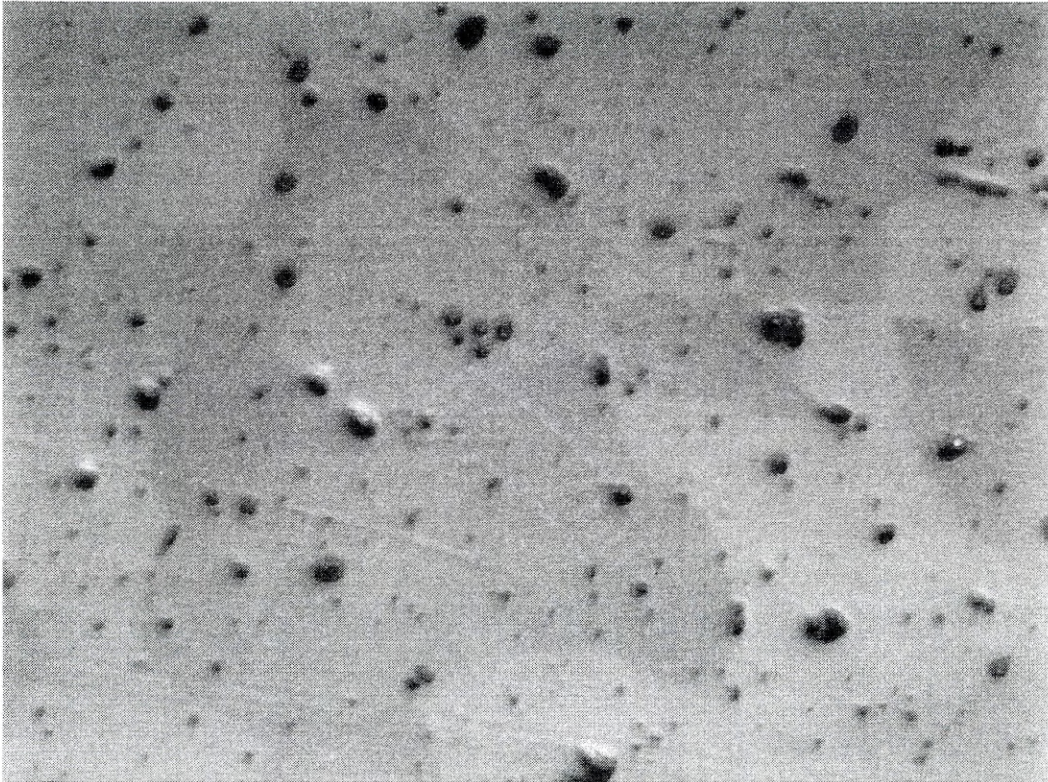


Figure 8: Light Micrograph of Polished Fe<sub>2</sub>O<sub>3</sub> Surface (500x)

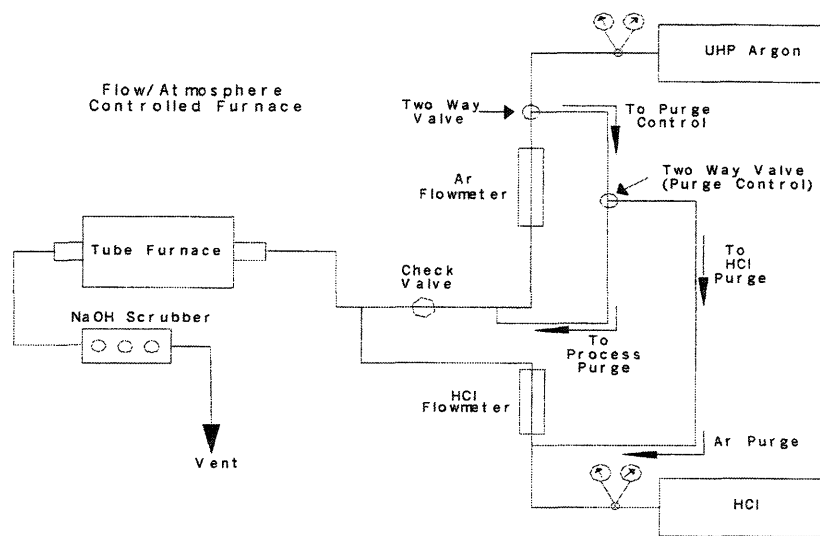


Figure 9: Air Atmosphere System Diagram

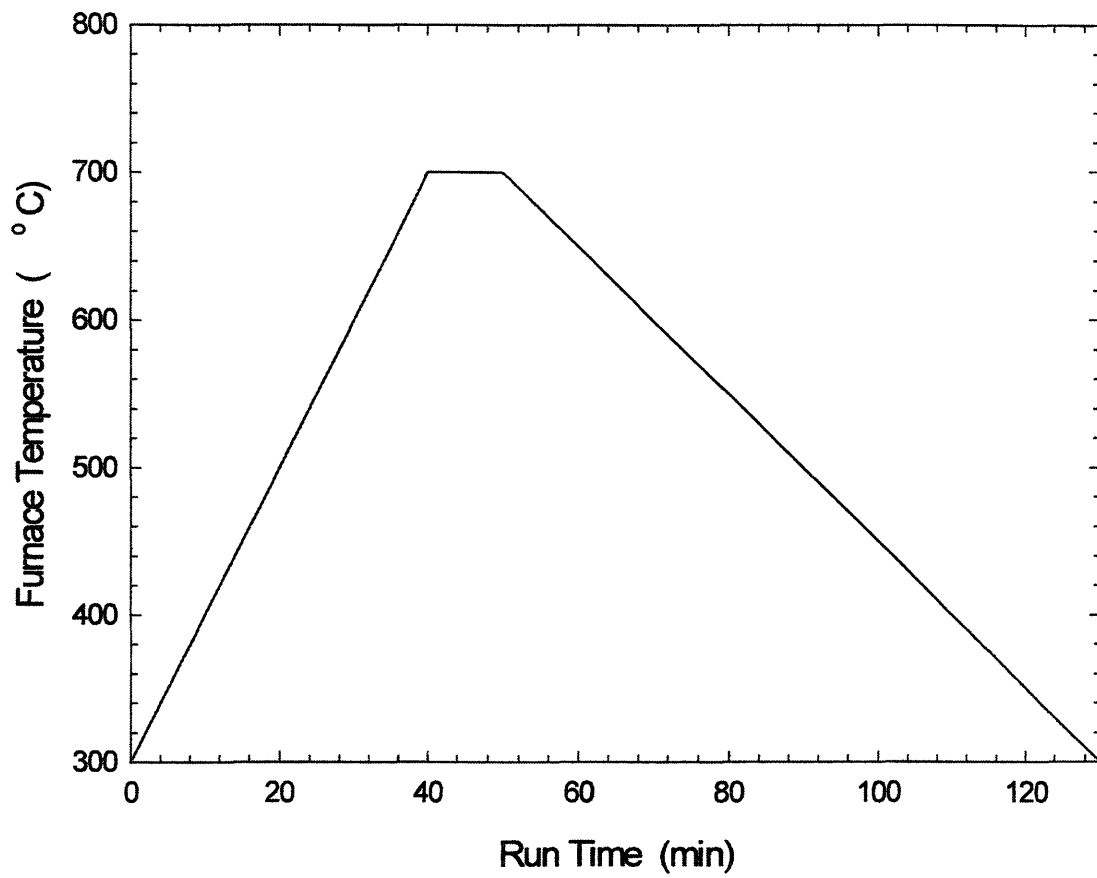


Figure 10: Furnace Temperature Profile (HCl Etch)



Afterwards, the furnace was, again, purged with argon to remove any HCl and allowed time to cool to around 300 °C before removing the samples.

The second approach made use of as-polished Fe<sub>2</sub>O<sub>3</sub> pellets that were cut into thirds with a slow-speed diamond blade saw. Each third was inspected with a light microscope to ensure the polished side had not been badly damaged (refer to Figure 11). Then the pellet sections were placed in an alumina tube furnace (as described above) and annealed in air at 1100 °C for 30 minutes to alleviate polishing damage (see Figure 12). After the annealing step had been completed, the sections were placed in fused SiO<sub>2</sub> ampoules that were filled with 5% HCl-95% Ar mixtures at a calculated pressure that would reach 0.5 atm total pressure at the sintering temperature. (See Figure 13 for the gas delivery schematic for filling the ampoules.) For calculating ampoule pressures the ideal gas law is used:

$$n = (PV) / (RT)$$

where n is the number of moles of gas, P is pressure, V is volume of the ampoule, T is temperature and R is the gas constant. Because the number of moles of gas doesn't change within the ampoule, the following ratio is used to find the initial room temperature pressures in the ampoule that will yield a 0.5 atm pressure at the etching temperature:

$$P_1 / T_1 = P_2 / T_2$$

where P<sub>1</sub> and P<sub>2</sub> (in atm) are the pressures at designated temperatures T<sub>1</sub> and T<sub>2</sub> (in K).

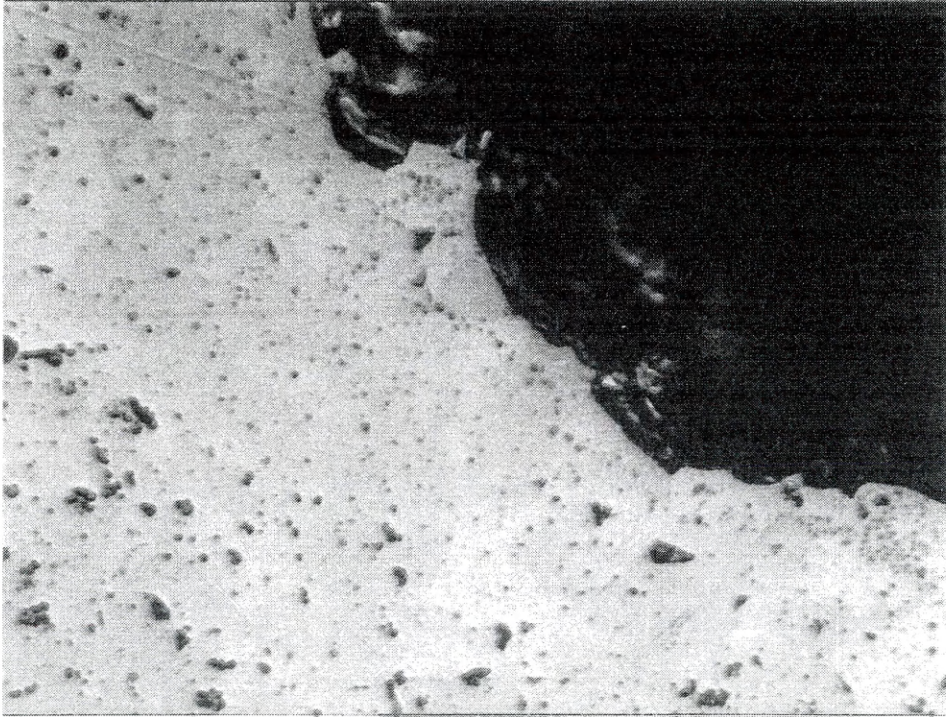


Figure 11: Light Micrograph of Cut Edge (500x)

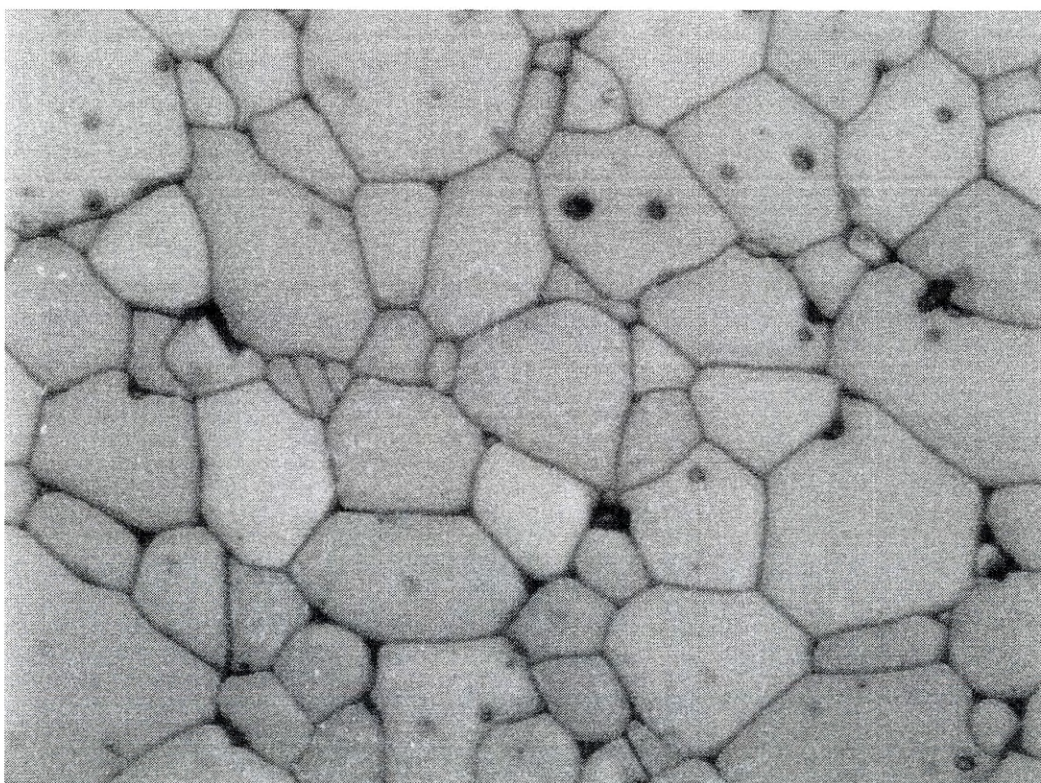


Figure 12: Light Micrograph of Air Annealed Fe<sub>2</sub>O<sub>3</sub> (500x)

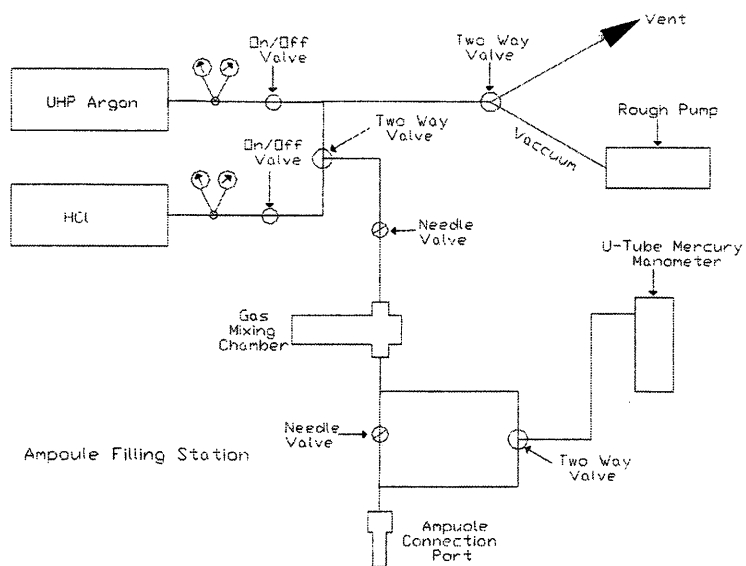


Figure 13: Ampoule Gas Delivery Schematic

The fused SiO<sub>2</sub> ampoules were sealed with an oxygen-acetylene torch after being filled with the gas mixture. These sealed ampoules were placed in the tube furnace at previously mentioned at 300 °C with fiberfax insulation to avoid large temperature gradients in the furnace and fired at the given temperature and time. The samples were also removed after the furnace was cooled to temperatures around 300 °C.

#### 4.2 Analytical Techniques

In order to analyze the experimental samples, an atomic force microscope (AFM) and a scanning electron microscope (SEM) were used. All samples were thoroughly cleaned before assessment. Following are the details of the analytical methods practiced.

##### 4.2.1 Atomic Force Microscope

The Physics Department of the Colorado School of Mines provided an AFM for use in the analysis. The AFM was a Digital Instruments D-3000 Nanoscope (in contact mode), which could profile the topography of the pellets surface producing a very accurate, three-dimensional picture. The tips used were type NP-20, Si<sub>3</sub>N<sub>4</sub> cantilever having stiffnesses ranging from 0.06-0.58 N/m.

##### 4.2.2 Scanning Electron Microscope

Scanning electron microscopy was utilized to characterize the surface microstructure of the samples and confirm the apparent steepness of grooves' edges profiled by AFM. However, before scanning electron microscopy could begin, the samples were gold-coated in order to create a conducting surface. The coating was produced by a Hummer VI argon sputter coater, operating at a 20 mA current, and was

approximately 200 to 400 angstroms in thickness. The scanning electron microscope (SEM) employed was in the Metallurgical and Materials Engineering Department at the Colorado School of Mines. The microscope was a JEOL Model No. JXA-840, operated at an accelerating voltage of 15 kV.

#### 4.2.3 Groove Width Measurement

After obtaining physical data from the AFM, Digital Instruments Nanoscope III, the software associated with the equipment stored the data as a three-dimensional net of points. From this software, three-dimensional images could be created revealing the relatively dramatic grooving at the sample surface (occurring at nanometer/micrometer level). The images were further analyzed by making two-dimensional 'slices' perpendicular to specific grooves. These slices were profiled and width measurements were made. Patterns for material deposition could also be seen from this method. Yet another way of manipulating the three-dimensional data was to take an average profile along a particular groove. Because sampling occurred within a box encompassing a groove, the grooves analyzed had to be straight. Figure 14 shows the results of the software performing this task. Areas of irregularities such as contamination, pores, etc. were avoided.

Statistical data can be seen in Appendix A, which shows standard errors, means, and probable causes for error

#### 4.2.4 Thermodynamic Calculations

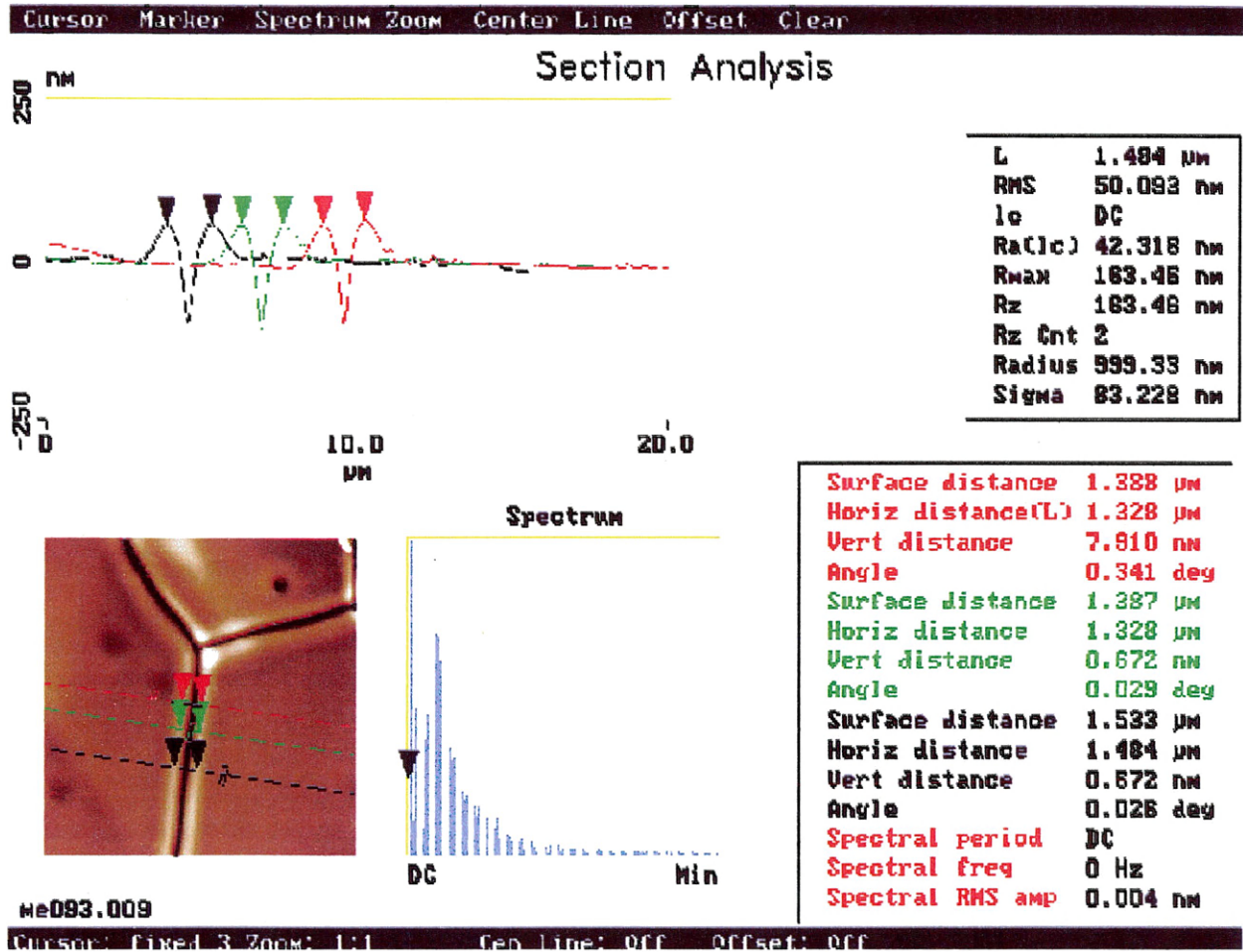
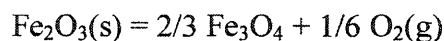


Figure 14: AFM Software Screen of Groove Measurement

The equilibrium pressures of the various gas species were determined with HSC Chemistry [41]. This program uses a total pressure of one atmosphere under equilibrium conditions for its calculation.

Figure 2 is a product partial pressures plot for  $\text{Fe}_2\text{O}_3$  in an air atmosphere. The figure shows that no products are formed and the sole mechanism for grooving is surface or volume (bulk) diffusion.

In Figure 3, the system started with 1 mole of  $\text{Fe}_2\text{O}_3$ , 0.975 moles of Ar, and 0.025 moles of HCl. As the number of moles in the gas phase changes, the volume of the system adjusts to give a total gas pressure of one atmosphere. Therefore, above 1300 °C where  $\text{Fe}_2\text{O}_3$  has decomposed to  $\text{Fe}_3\text{O}_4$ , there is an additional 1/6 moles of oxygen in the system from:



which gives an oxygen pressure of about 0.16 atm.

At temperatures below about 200 °C,  $\text{FeCl}_2$  and  $\text{FeCl}_3$  both condense and are in equilibrium and determine the equilibrium chlorine pressure. Only  $\text{FeCl}_2$  condenses between 200 and 400 °C. Below 1100 °C, the oxygen pressure is determined by the equilibrium between  $\text{Fe}_2\text{O}_3$  and HCl. However, between 1100 and 1300 °C, the oxygen pressure is determined by the equilibrium between  $\text{Fe}_2\text{O}_3$  and  $\text{Fe}_3\text{O}_4$ . Above, 1300 °C the oxygen pressure is essentially constant with a fixed 1/6 mole of  $\text{O}_2$  in the gas phase as shown above.

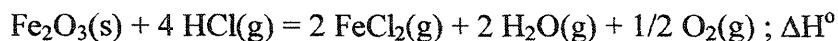


Therefore, experiments on vapor transport can be carried out over the range of 400 °C to 1100 ° C in 0.025 atm partial pressure of HCl in Ar and have Fe<sub>2</sub>O<sub>3</sub> as the only solid phase in equilibrium with the vapor phase.

The calculated vapor pressures over Fe<sub>2</sub>O<sub>3</sub> in 0.025 atm partial pressure of HCl in Ar are plotted versus 1/T in Figure 15. The pressure of FeCl<sub>3</sub> is essentially constant over this temperature range. However, the FeCl<sub>2</sub> pressure and the sum of the FeCl<sub>2</sub> and FeCl<sub>3</sub> pressures give reasonable straight lines on a log p versus 1/T plot over this temperature range. The straight lines on the plot are the least squares fits to the data and the Q<sub>app</sub> are the apparent activation energies calculated from:

$$p = A \exp(-Q_{\text{app}}/RT).$$

For the pressure of FeCl<sub>2</sub>, this is determined essentially by:



where the equilibrium constant, K<sub>e</sub>, is given by:

$$\frac{p(\text{FeCl}_2)^2 p(\text{H}_2\text{O})^2 p(\text{O}_2)^{\frac{1}{2}}}{p(\text{HCl})^4} = K_e.$$

If all of the H<sub>2</sub>O and O<sub>2</sub> are produced by this reaction, then p(H<sub>2</sub>O) = p(FeCl<sub>2</sub>) and p(O<sub>2</sub>) = 1/4 p(FeCl<sub>2</sub>). Substitution of these into the equilibrium constant gives:

$$p(\text{FeCl}_2) = 4^{\frac{1}{9}} p(\text{HCl})^{\frac{8}{9}} e^{\frac{2\Delta S^\circ}{9R}} e^{-\frac{2\Delta H^\circ}{9RT}}$$

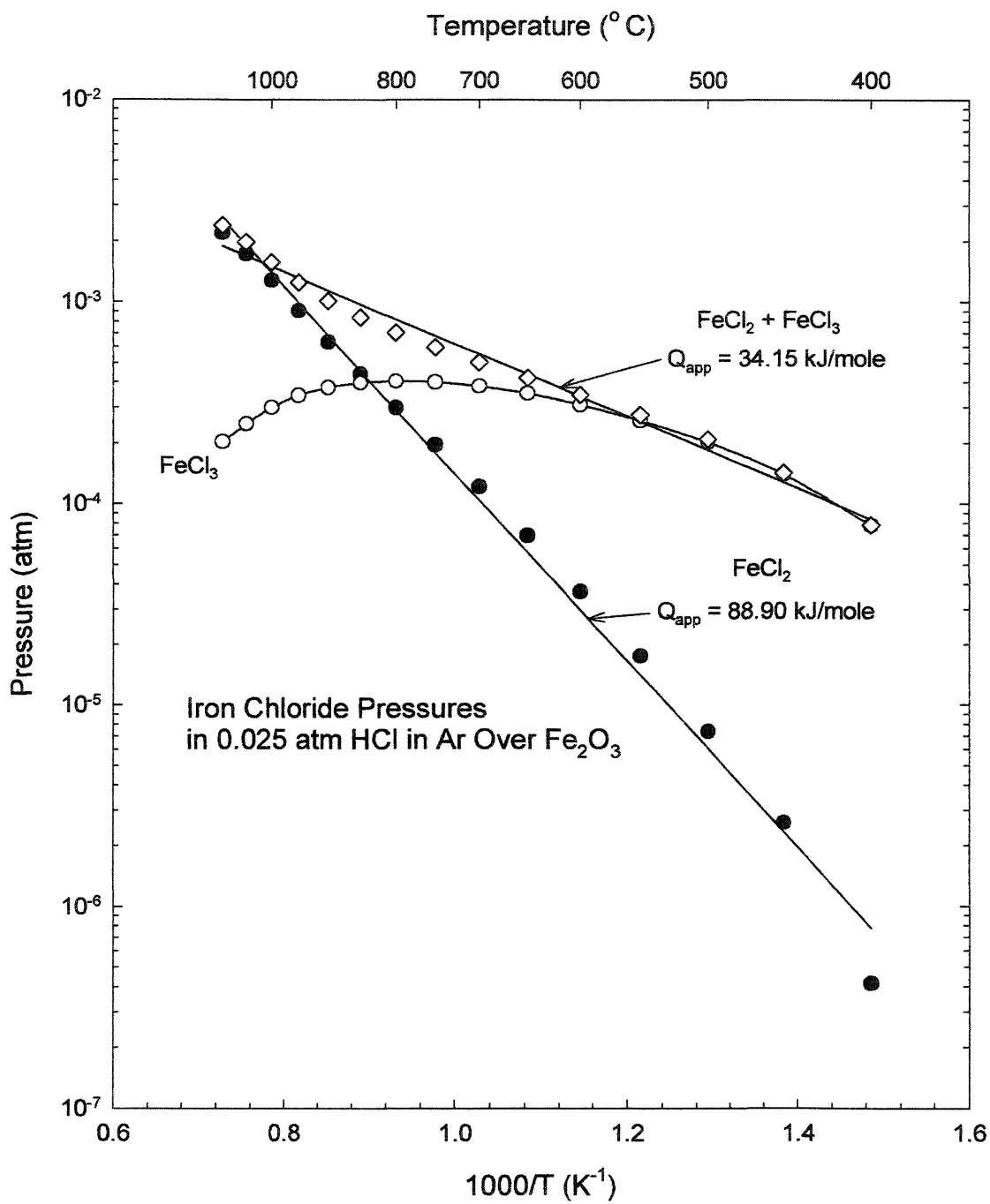


Figure 15: Iron Chloride Partial Pressures for Fe<sub>2</sub>O<sub>3</sub>/HCl Reaction

so  $Q_{\text{app}} = 2/9 \Delta H^\circ$ ; that is, the apparent activation energy for the change in  $\text{FeCl}_2$  pressure with temperature is  $2/9$  of the standard enthalpy for the reaction of  $\text{Fe}_2\text{O}_3$  with  $\text{HCl}$  given above. (Also refer to Appendix B).

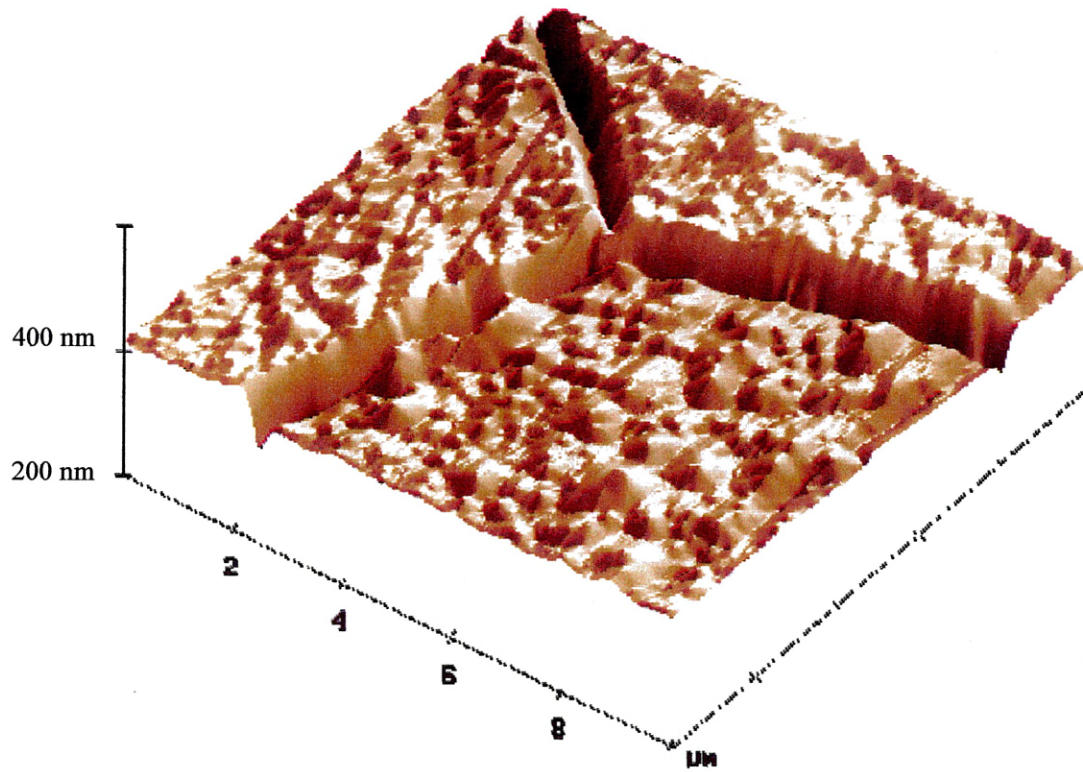
## CHAPTER 5

### RESULTS

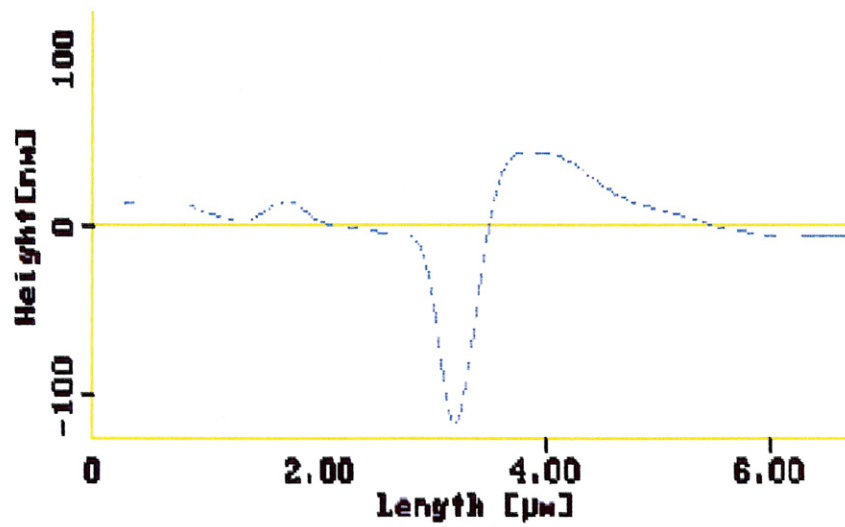
Polished  $\text{Fe}_2\text{O}_3$  surfaces (shown in Figure 8) were etched in air and HCl atmospheres for various times and temperatures yielding data that was analyzed for activation energies, diffusion constants, and rate-controlling mechanisms at certain time and temperature ranges. The experimental results were compared with literature and calculated data.

#### 5.1 Experimental Results

The HCl atmosphere was initially introduced into a “flow” system. The flow chamber, as described earlier, had a very slow flow (so as to simulate static conditions) of 95% Ar-5% HCl gas that seeped through the assembly with a constant total pressure of 1 atm. Although images in Figures 16 and 17 are provided for the specimens produced in this method, no data were taken due to the bulk corrosion and unequilibrated reaction conditions that were present. As can be seen in Figure 17, the grain boundary grooves are almost as large as the grain size. In addition, significant general material loss has occurred as evident by the differences in height of the various grains observed in Figure 17. As a result, an ampoule technique of etching in HCl was developed to prevent extensive material loss. This procedure made the time to reach equilibrium much quicker because of the chamber volume difference between the five-foot long alumina tube, first used, and the estimated two-inch fused silica ampoule utilized in this technique. Also,



a) AFM 3-dimensional image



b) AFM Groove Profile

Figure 16 a and b: Flow System, HCl-Etched Grooves at 873 K for 5 min

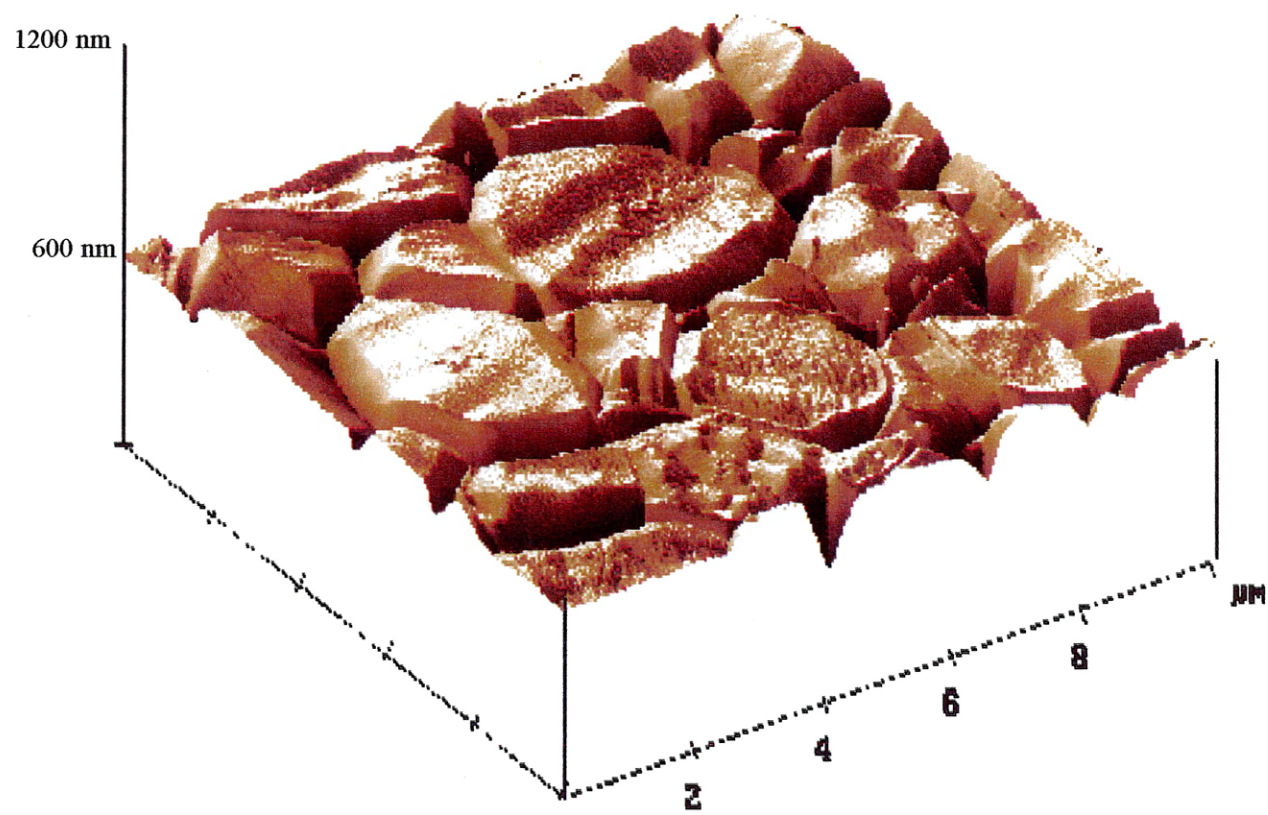


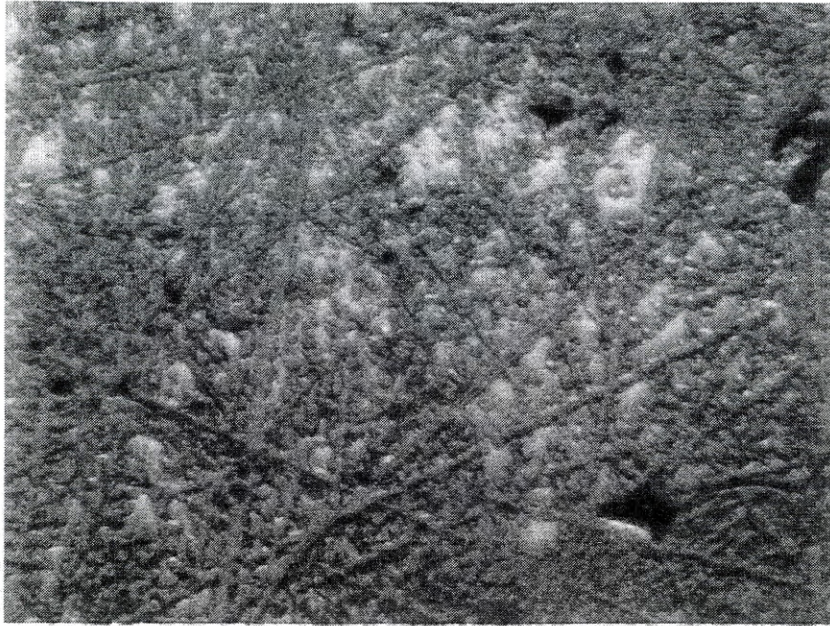
Figure 17: AFM 3-Dimensional Image of an Etched Surface  
in a HCl Flow System at 1073 K for 5 minutes

the ampoule maintained a much more uniform temperature within the volume than the tube, which had cold ends, thus convective currents. The ampoule was filled with the same gas mixture under a total pressure of 0.5 atm (at etching temperature). The first attempt utilized samples, which were not annealed before etching. As shown in Figure 18, these samples underwent preferential etching at the surface scratches and no grain boundary grooving could be measured. It was then established that the samples should be annealed

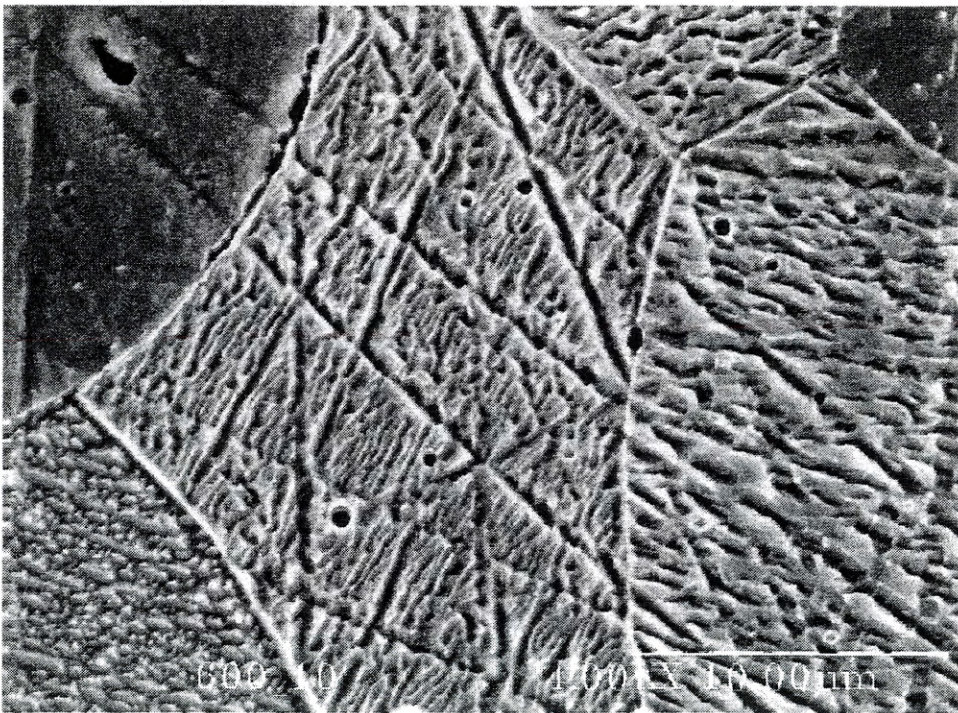
prior to etching to alleviate any initial surface damage. The data that this process acquired could be better related to Mullins model where the other method could not (due to nonequilibrium conditions) and was much more readable. Figures 19 and 21 provide AFM groove profiles, three-dimensional images, and SEM micrographs of the ampoule-sealed samples.

In contrast, Figures 22 and 23 show SEM micrographs, AFM groove profiles, and three-dimensional images for air-fired samples. These grooves are not only smaller in size, but also more symmetrical in shape.

The groove widths have been plotted against time and temperature for both air-etched and HCl-etched specimens. These graphs are presented in Figures 24 through 31. The raw data for groove measurements are found in Appendix D and groove profiles and images for other etched samples are found in Appendix E.



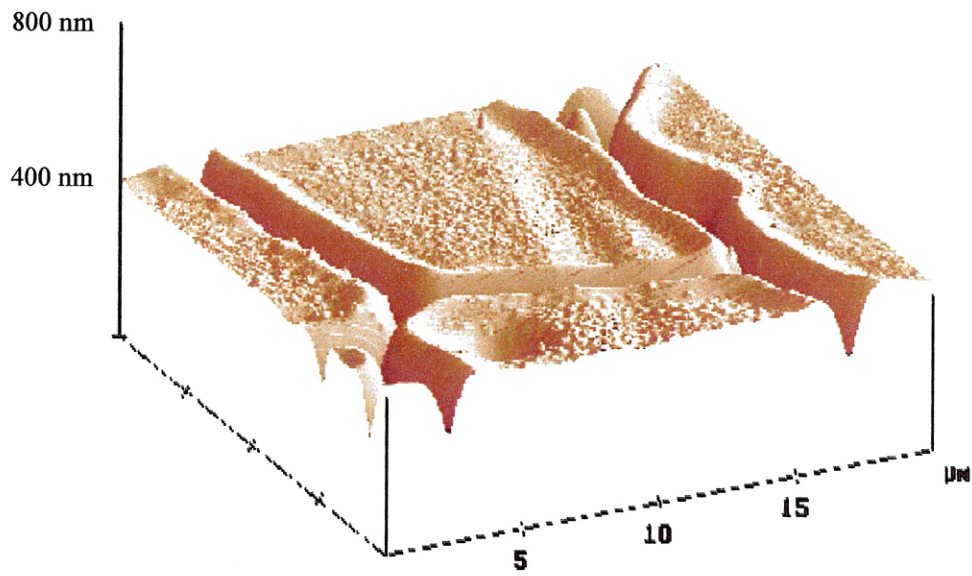
a) Light Micrograph (500x)



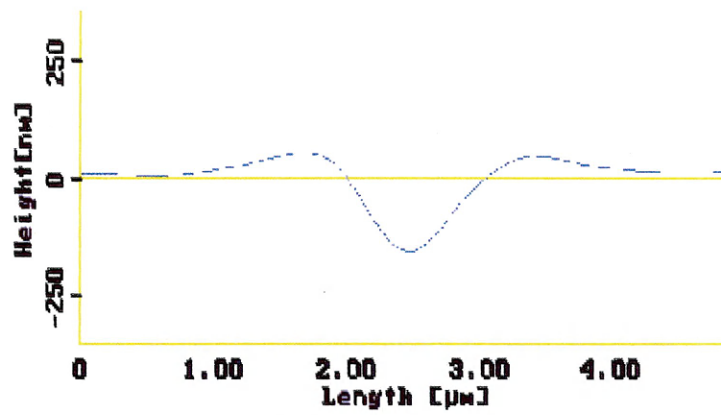
b) SEM Image

Figure 18 a and b: Non-Annealed, HCl-Etched Fe<sub>2</sub>O<sub>3</sub>

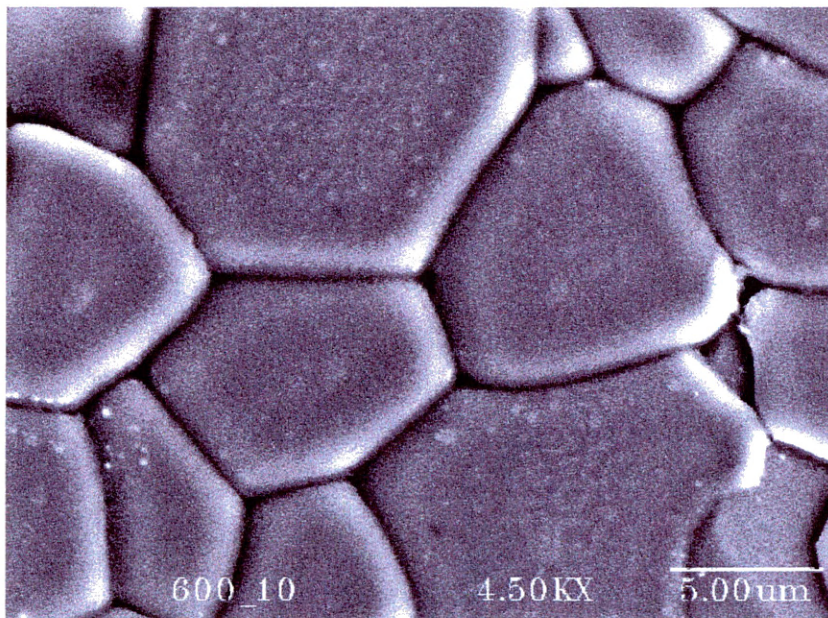




a) 3-dimensional AFM

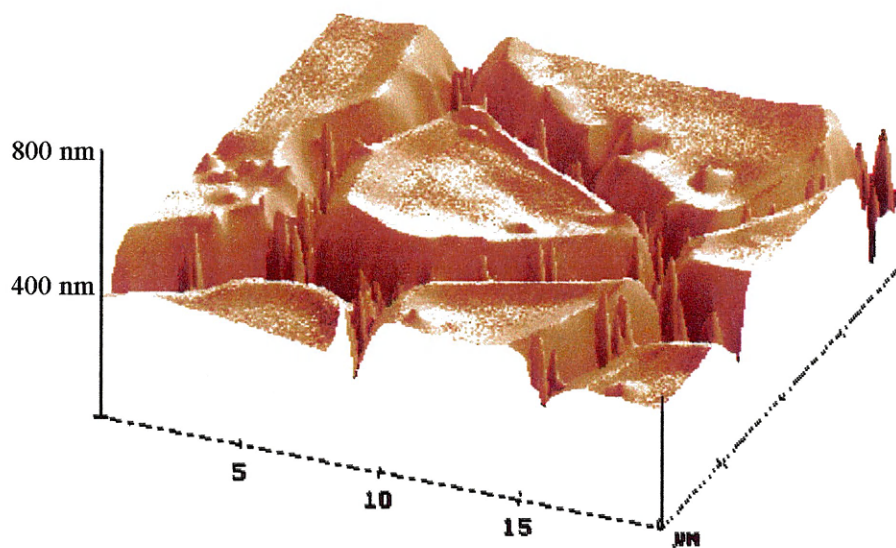


b) AFM groove profile

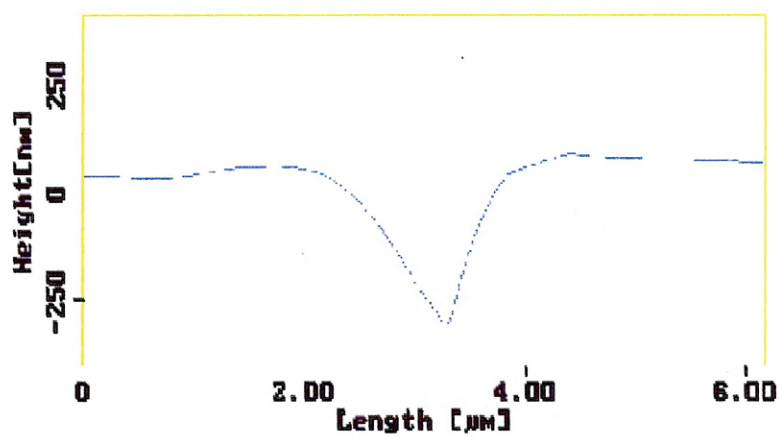


c) SEM

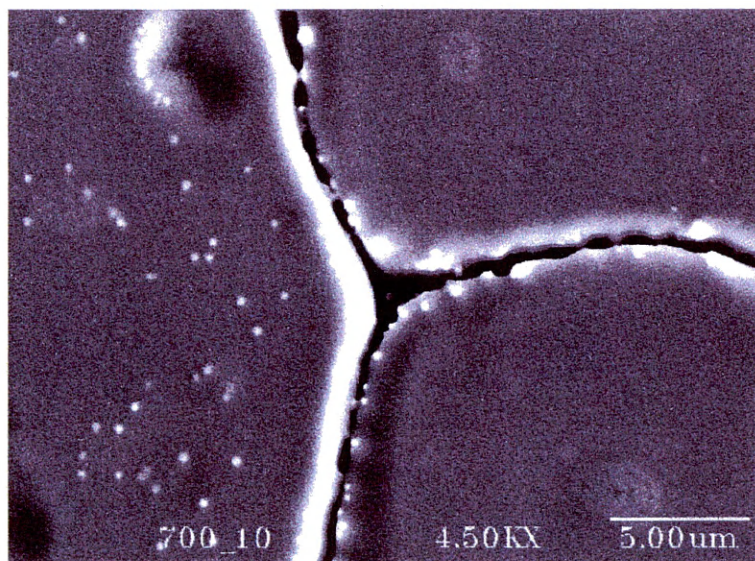
Figure 19 a, b, and c: HCl Etched Samples at 873 K for 10 minutes



a) 3-dimensional AFM

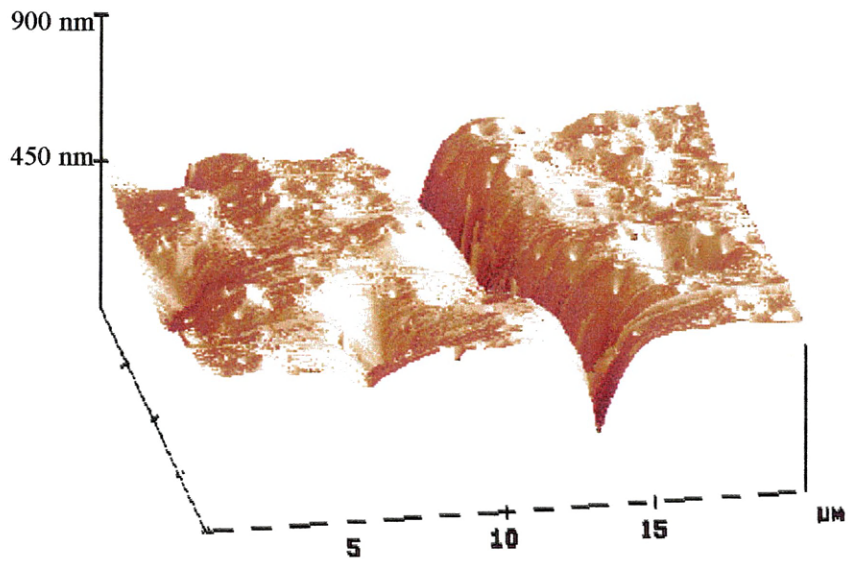


b) AFM groove profile

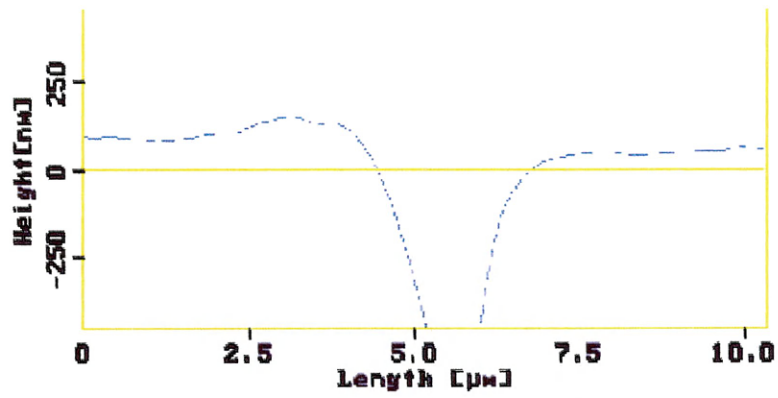


c) SEM

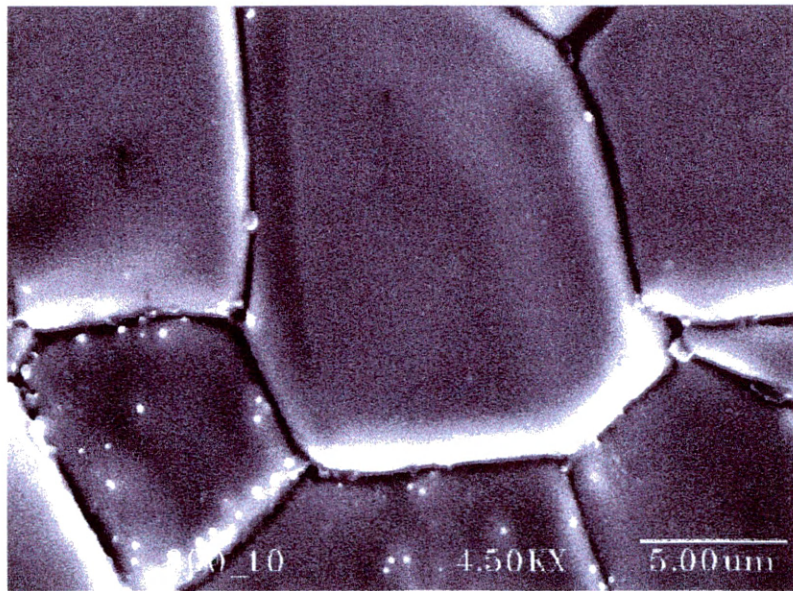
Figure 20 a, b, and c: HCl Etched Samples at 973 K for 10 minutes



a) 3-dimensional AFM

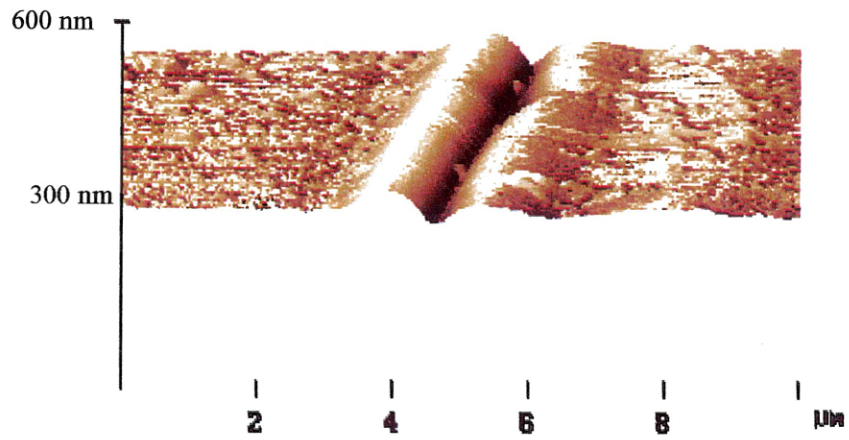


b) AFM groove profile

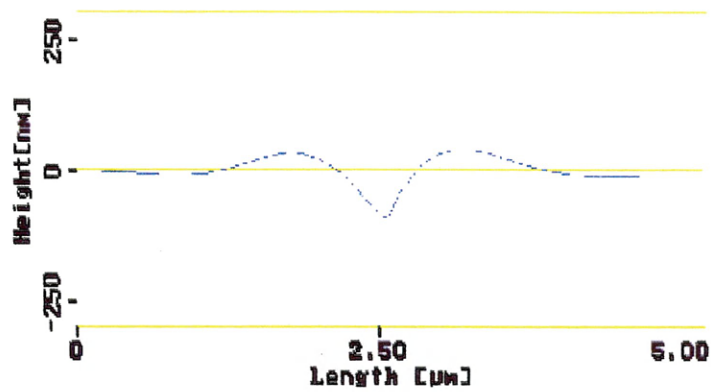


c) SEM

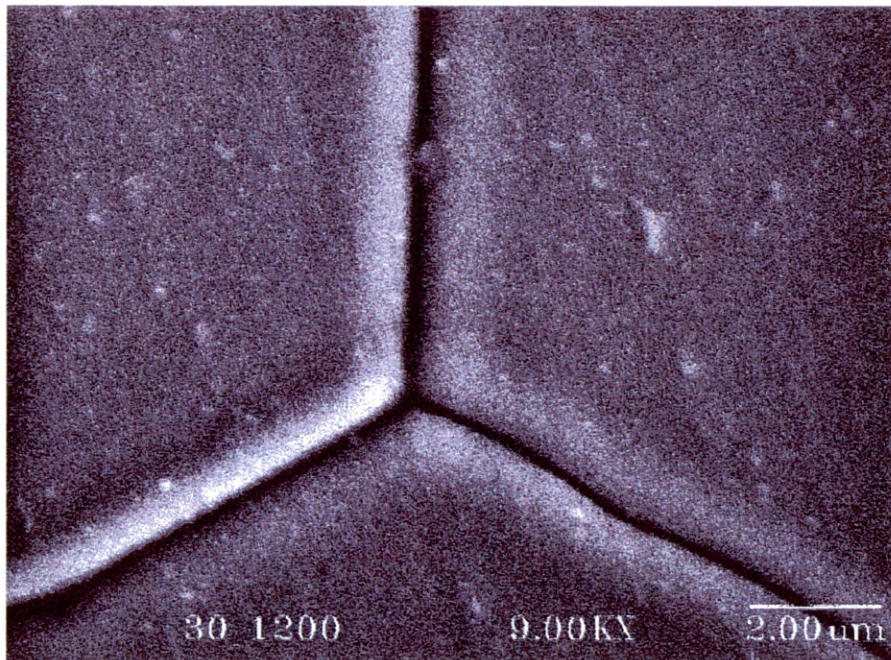
Figure 21 a, b, and c: HCl Etched Samples at 1073 K for 10 minutes



a) 3-dimensional AFM

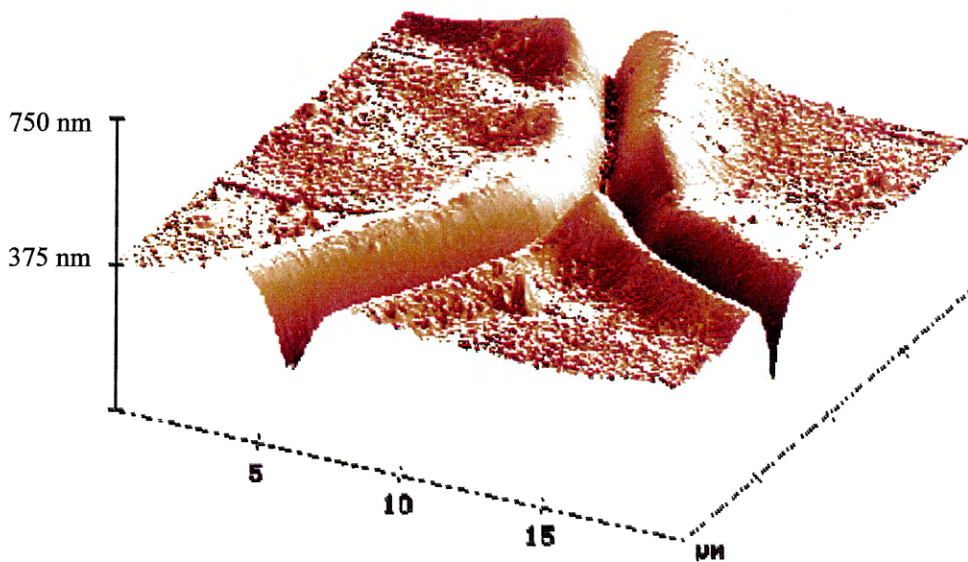


b) AFM groove profile

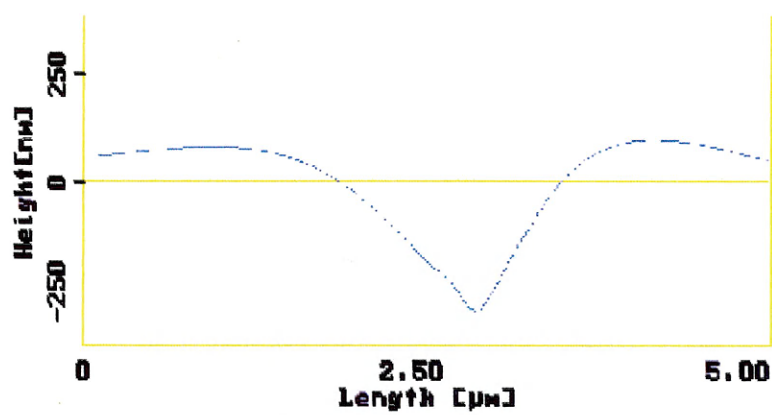


c) SEM

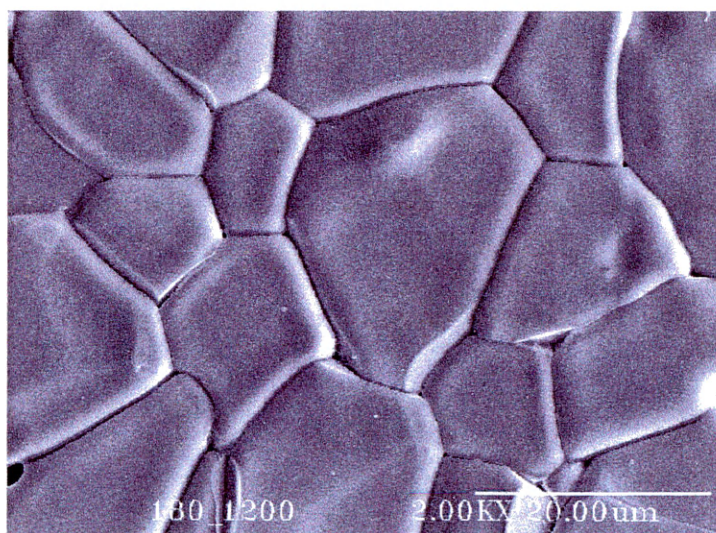
Figure 22 a, b, and c: Air Etched Sample at 1473 K for 30 minutes



a) 3-dimensional AFM



b) AFM groove profile



c) SEM

Figure 23 a, b, and c: Air Etched Sample at 1473 K for 180 minutes

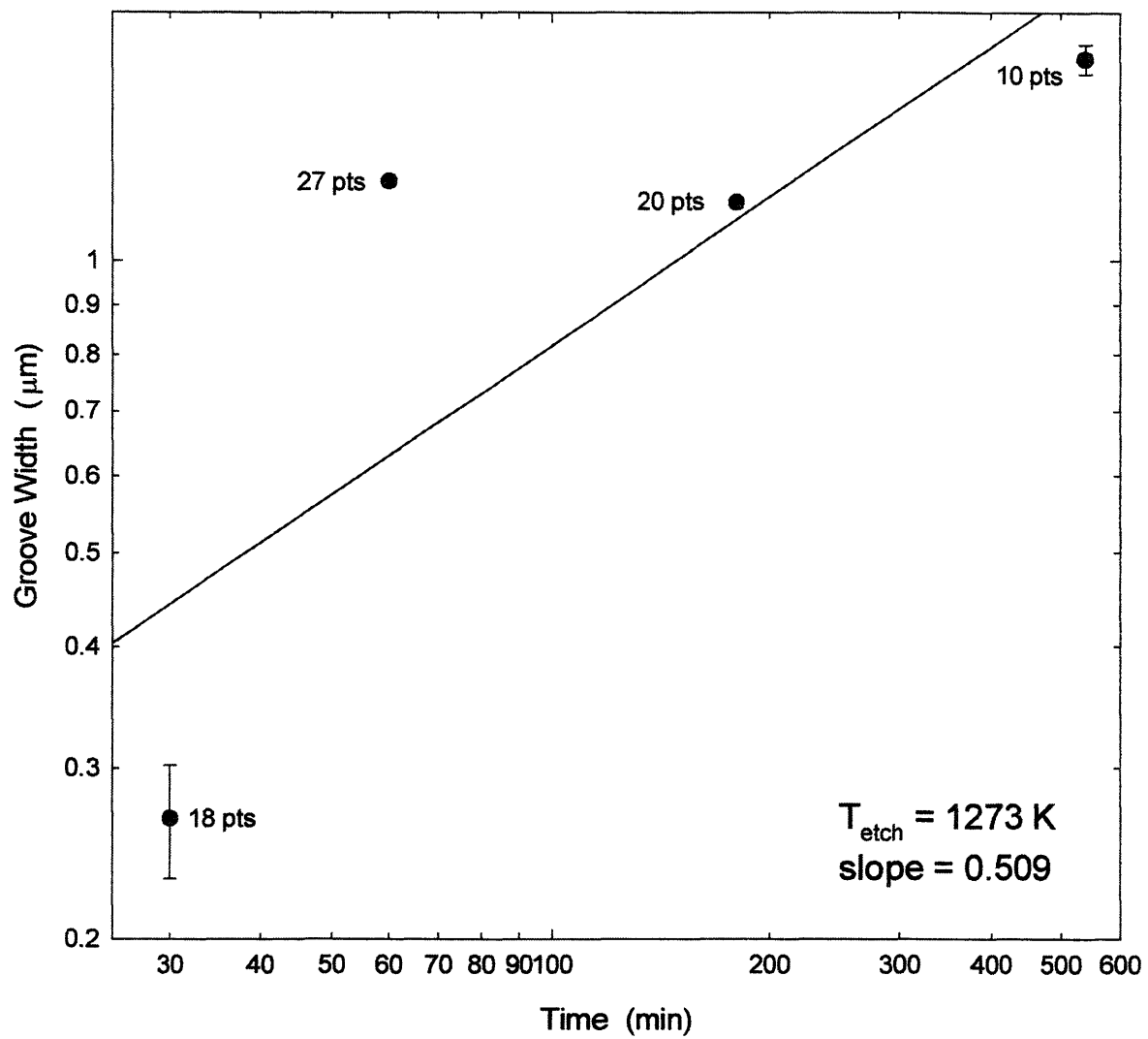


Figure 24: Air Groove Width vs. Time for 1273 K Temperature

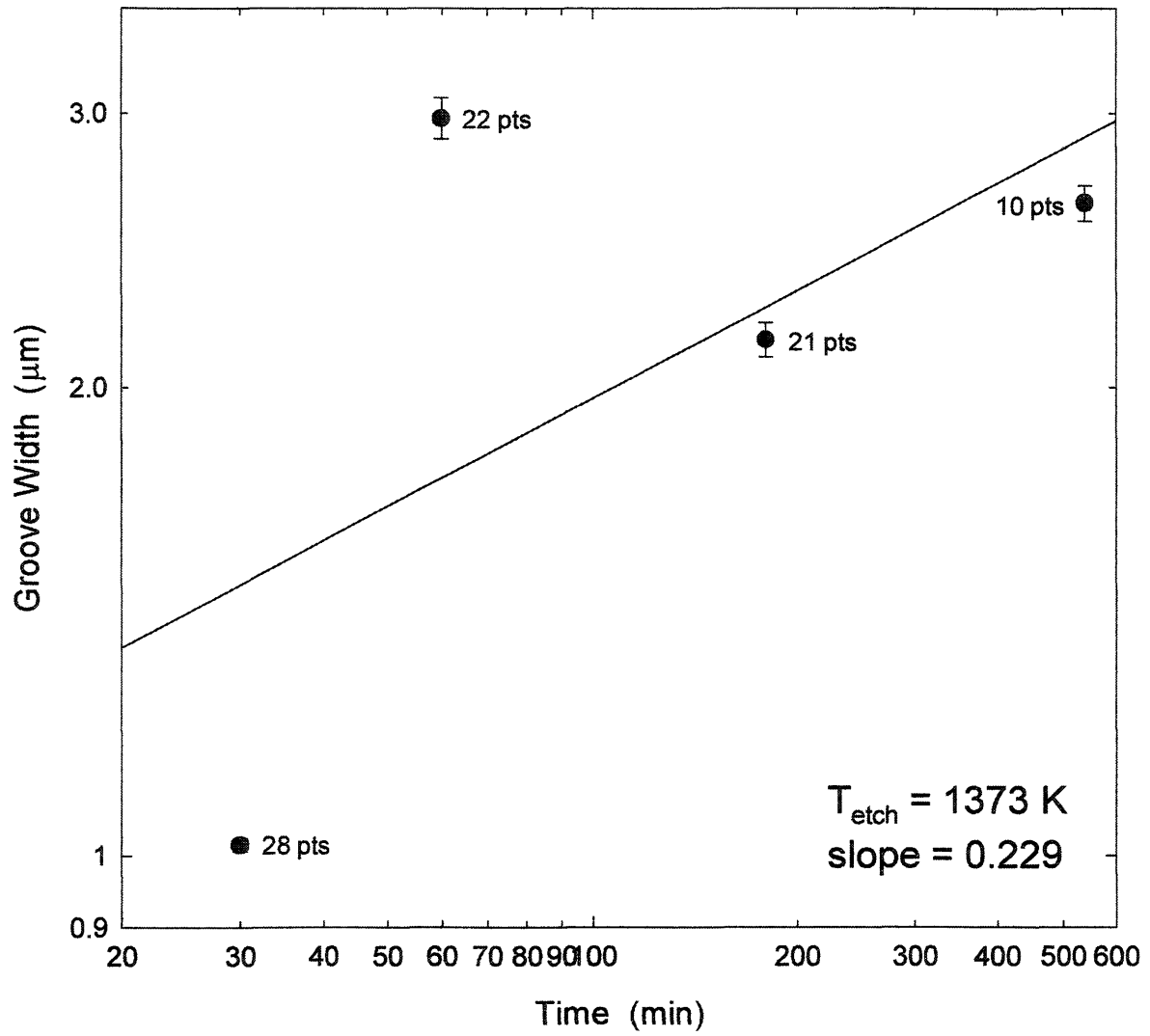


Figure 25: Air Groove Width vs. Time for 1373 K Temperature

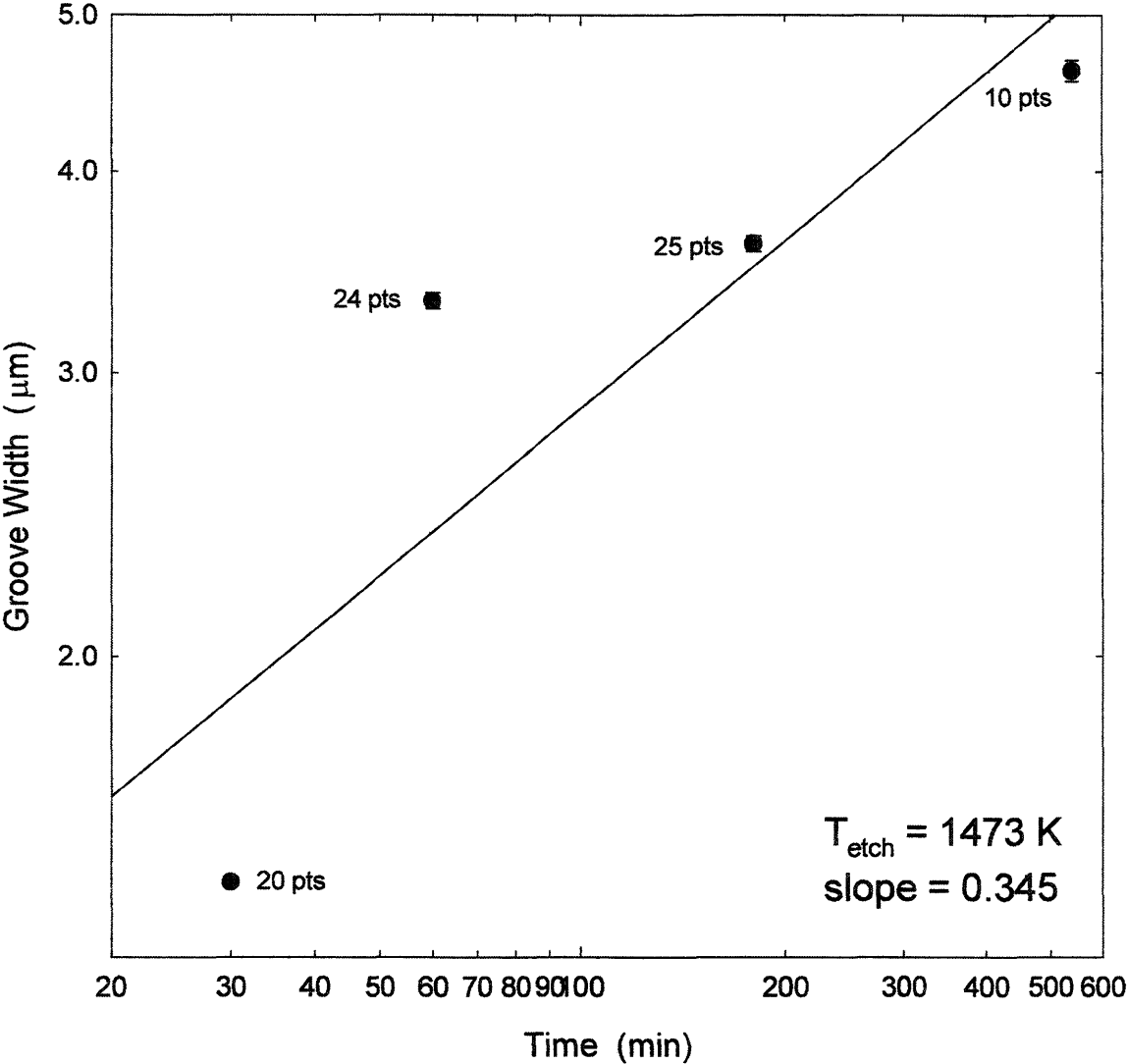


Figure 26: Air Groove Width vs. Time for 1473 K Temperature



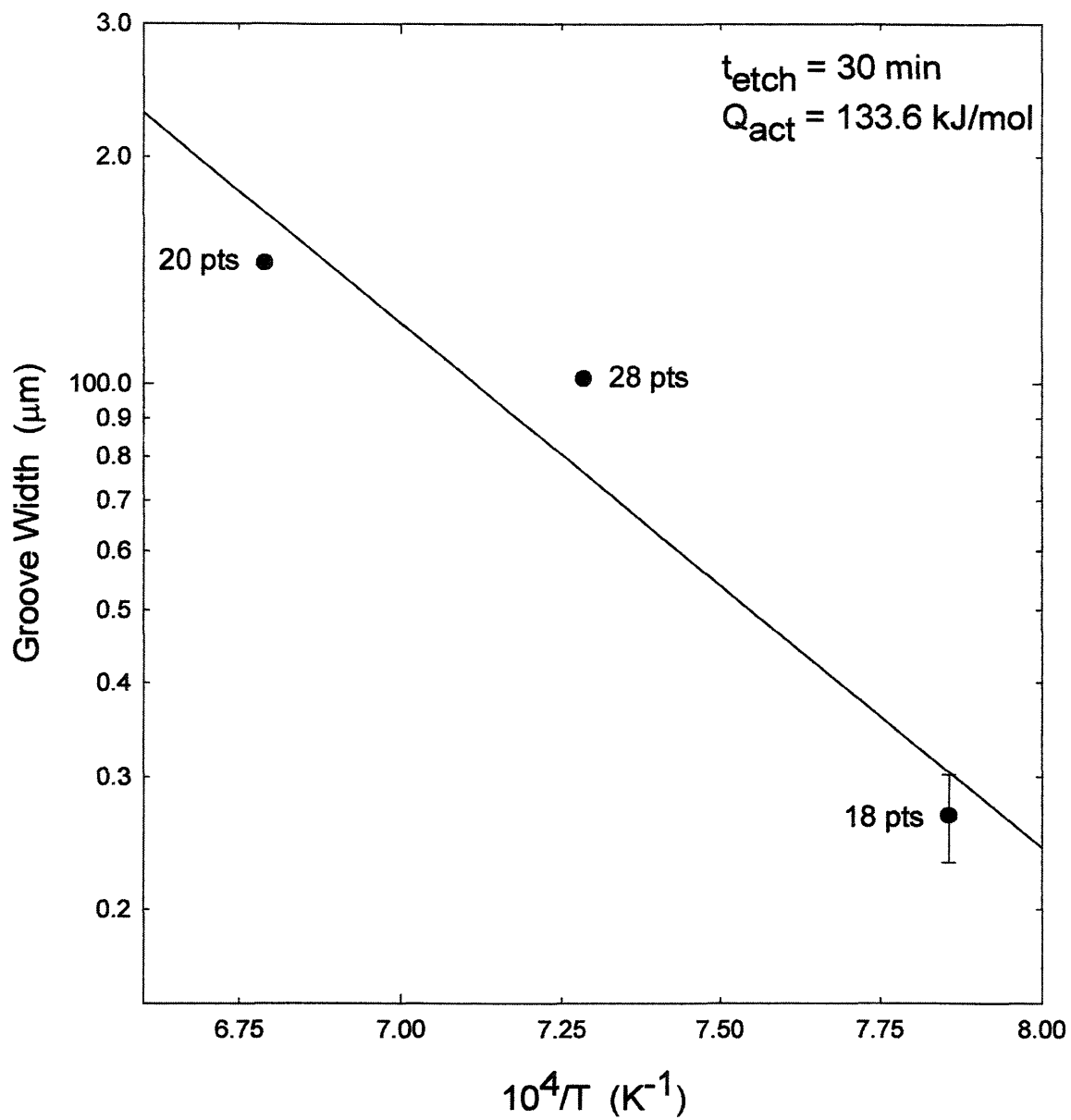


Figure 27: Air Groove Width vs. Temperature for 30 min Etch Time

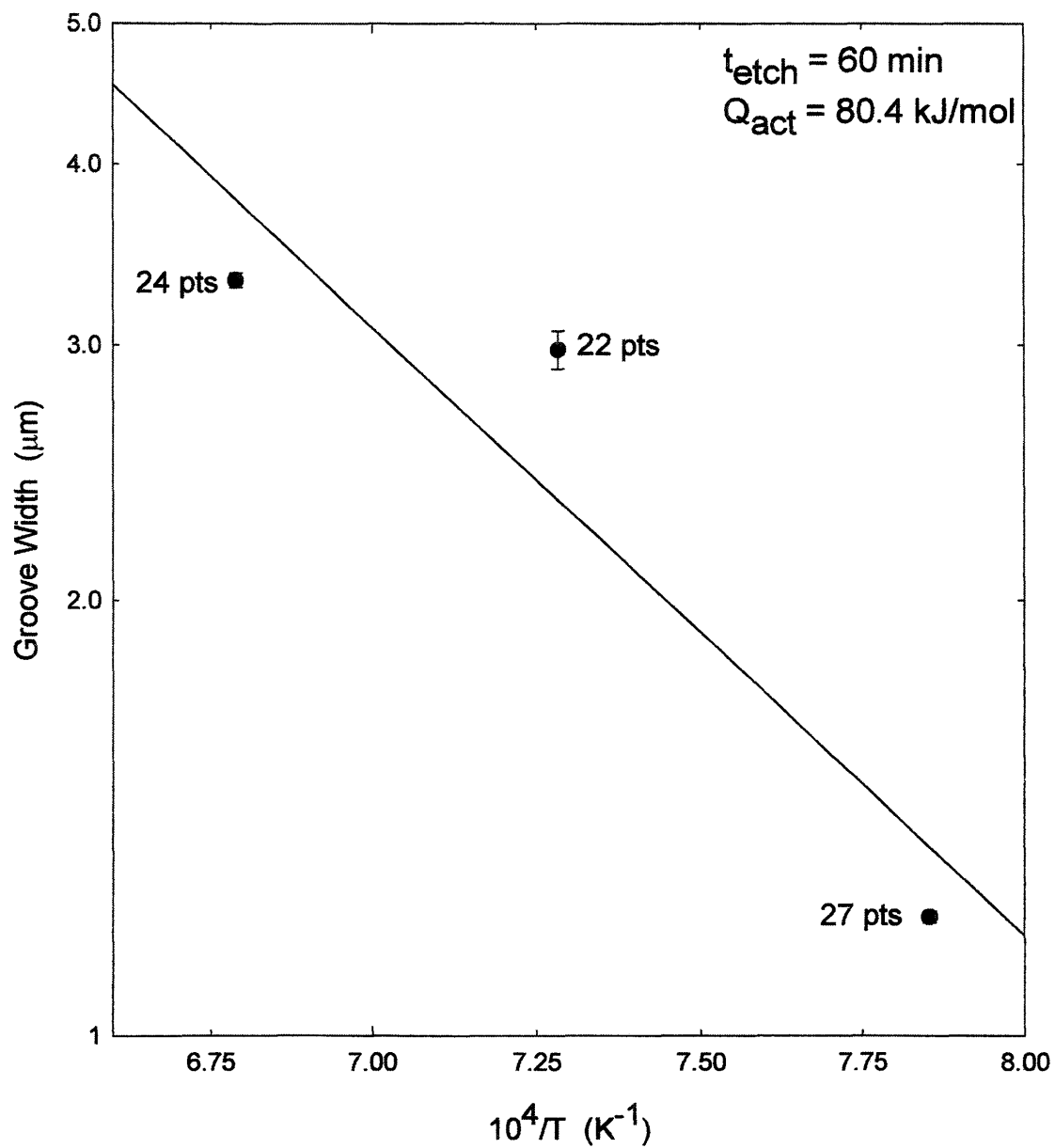


Figure 28: Air Groove Width vs. Temperature for 60 min Etch Time

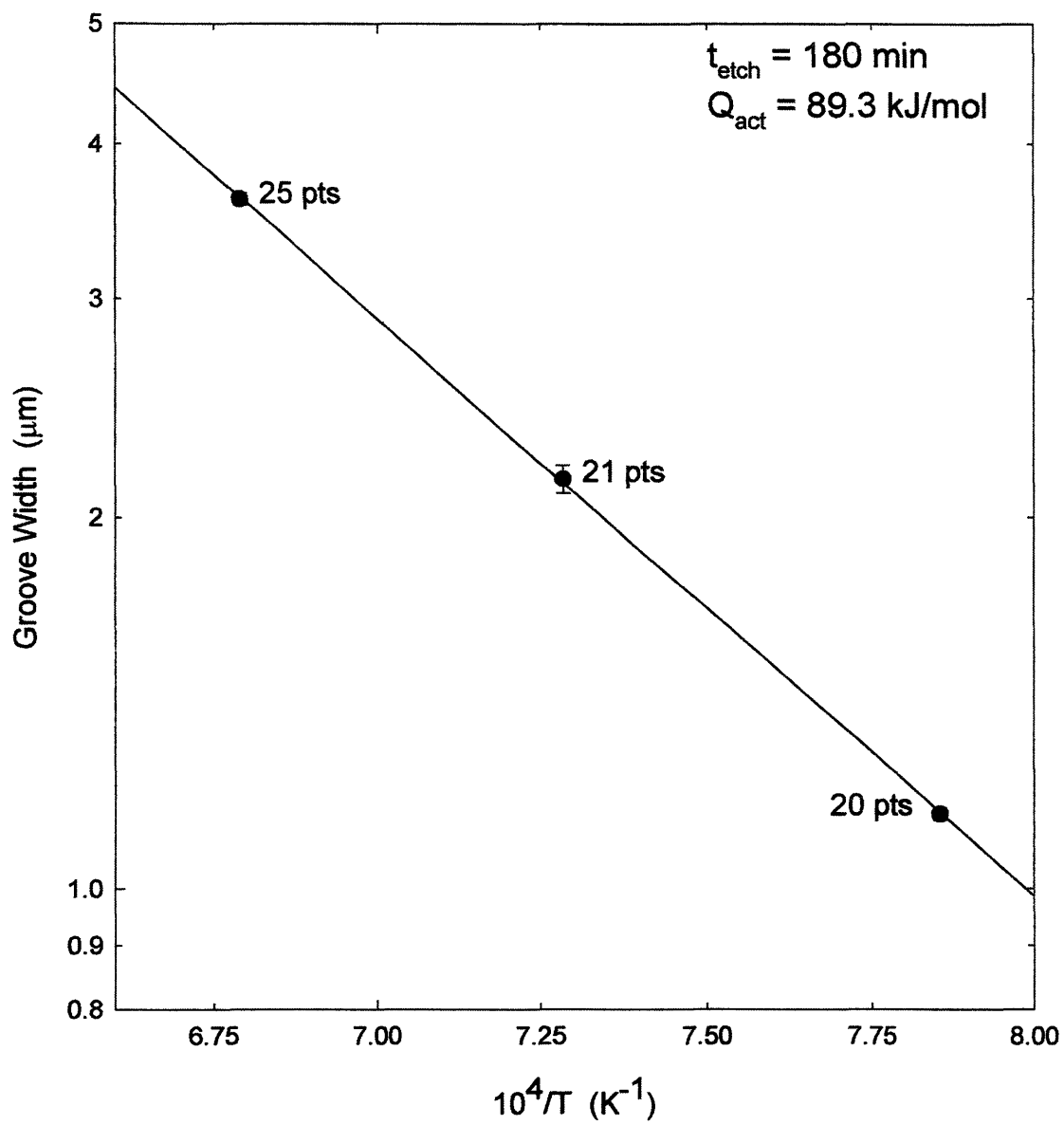


Figure 29: Air Groove Width vs. Temperature for 180 min Etch Time

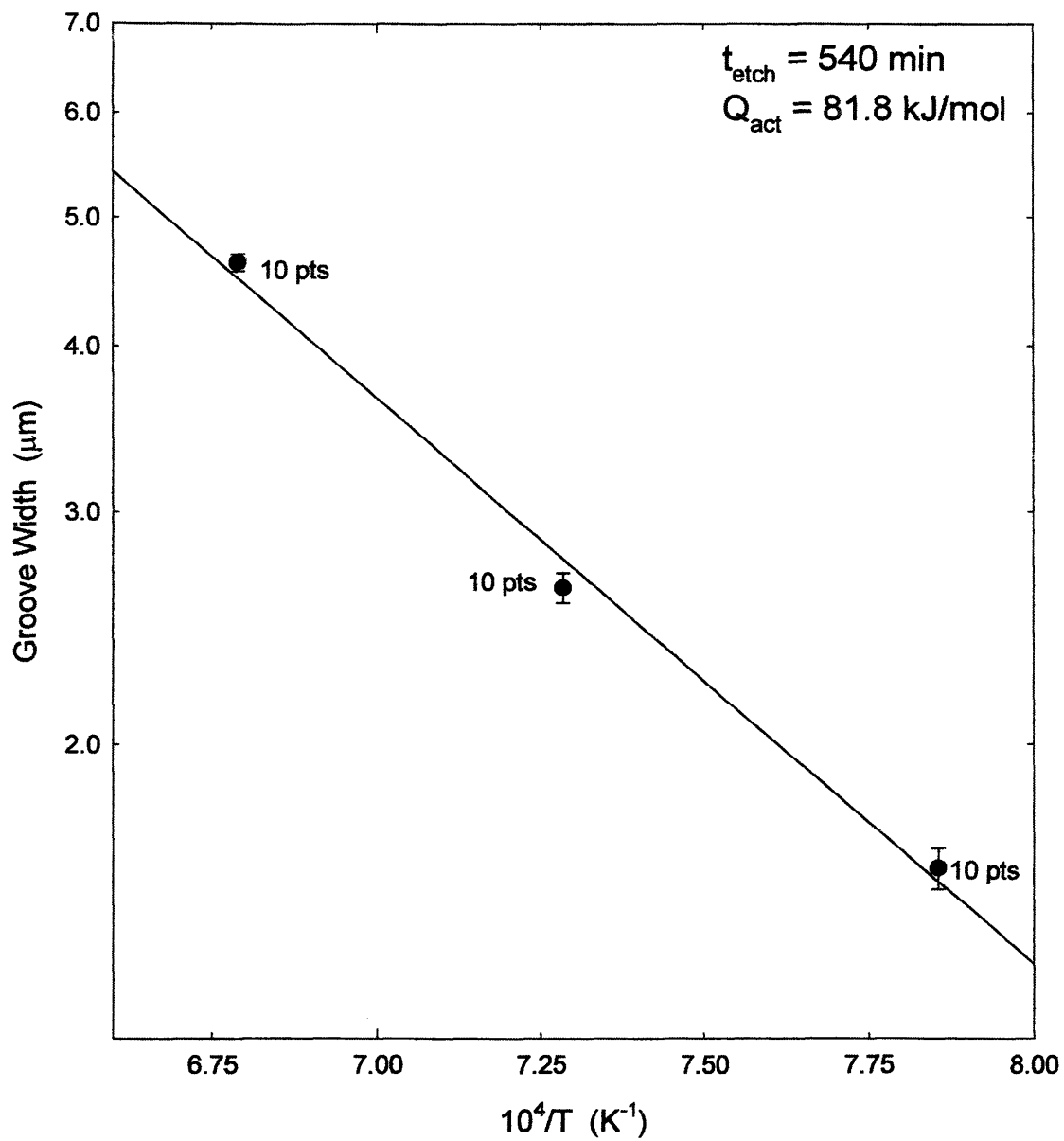


Figure 30: Air Groove Width vs. Temperature for 540 min Etch Time

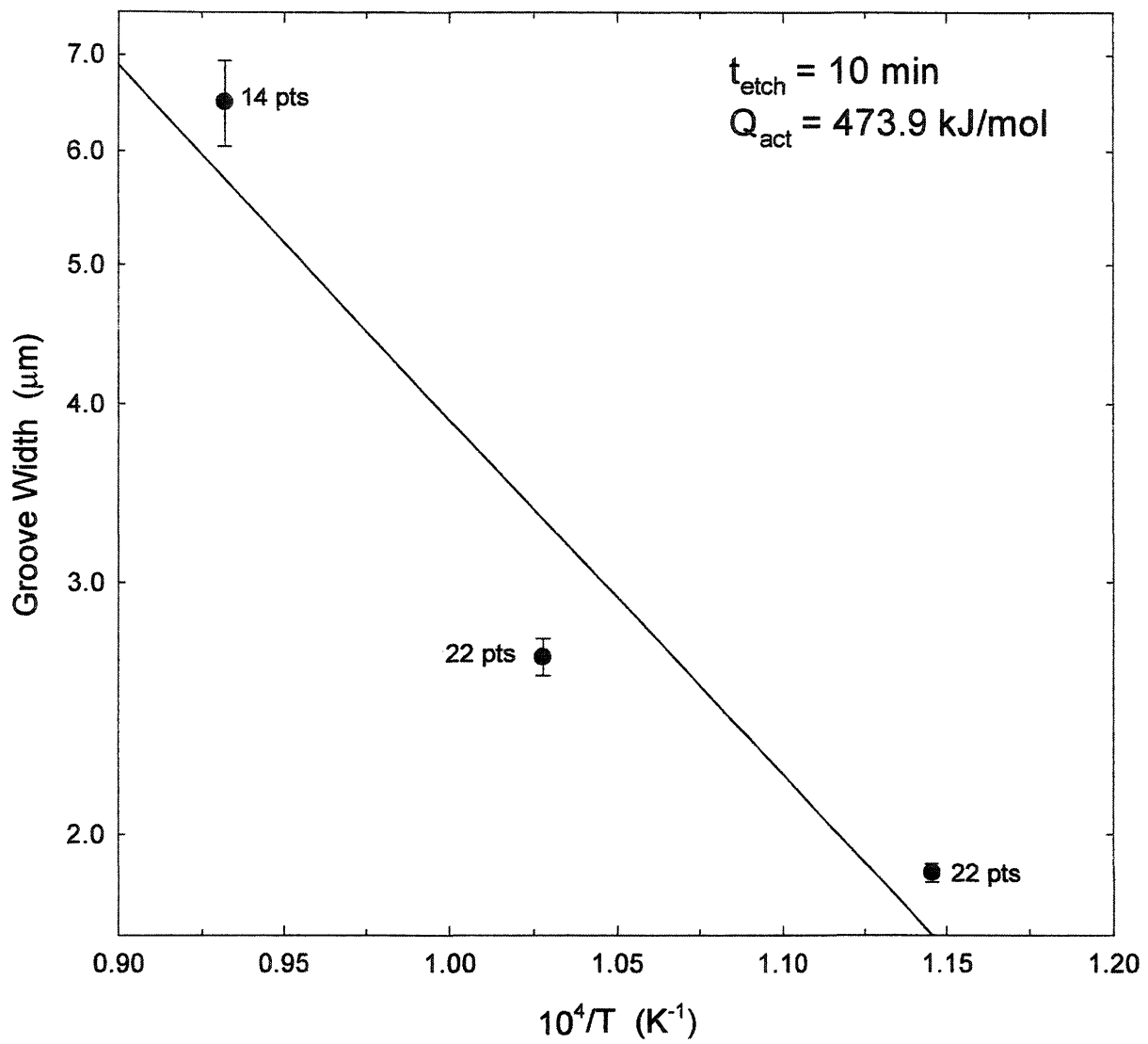


Figure 31: HCl Groove Width vs. Temperature for 10 min Etch Time

## CHAPTER 6

### DISCUSSION

#### 6.1 Groove Widths in Air

Recall from Table 1 that the time dependency of groove widths vary with the rate-controlling mechanisms:  $t^{1/2}$  for evaporation-condensation,  $t^{1/4}$  for surface diffusion, and  $t^{1/3}$  for volume diffusion. In addition, concurrent mechanisms can create dependencies ranging between these values. Linear regressions for log-log plots (as seen in Figures 23 through 25) of groove widths in air atmosphere corrosion possess slopes, which indicate the time dependencies at several temperatures. As confirmed from the partial pressures plot for  $\text{Fe}_2\text{O}_3$  in 1 atm of air (Figure 2), there are no Fe-containing gaseous species that would produce vapor transport at the temperatures that were tested; therefore, it can be concluded that the mechanism controlling is either surface diffusion or volume diffusion. With this in mind, at a corrosion temperature of 1273 K the time power dependence is observed to be 0.51, at 1373 K the dependence is 0.23, and at 1473 K the dependence is 0.35. These slopes are not very conclusive at first glance so the experimental mean groove widths were compared to predicted widths. (See Table 2.) The predicted groove widths were calculated from Mullins solid-state diffusion model of grain boundary grooving [21]; namely,

$$w^3 = \frac{125\gamma D\Omega}{RT} t$$

**TABLE 2: Groove Widths in Air Calculated From Literature Volume Diffusior**

Molar Volume = 30.47  
 Surface energy = 1.00E-04  
 R = 8.314

Time	Temperature	w, meas	Calculated (micron)				kJ/mole
			1	2	3	4	
		Reference	[42]	[43]	[44]	[45]	
		Q(diffusion)	419.2	468.6	405.0	325.9	kJ/mole
		Qapp	139.7	156.2	135.0	108.6	kJ/mole
			D(1)	D(2)	D(3)	D(4)	
30	1273	0.266	8.145E-12	2.361E-14	1.515E-18	8.614E-14	w(1)
30	1373	1.02	1.458E-10	5.938E-13	2.460E-17	8.115E-13	w(2)
30	1473	1.45	1.765E-09	9.638E-12	2.735E-16	5.638E-12	w(3)
60	1273	1.21	8.145E-12	2.361E-14	1.515E-18	8.614E-14	w(4)
60	1373	2.98	1.458E-10	5.938E-13	2.460E-17	8.115E-13	
60	1473	3.33	1.765E-09	9.638E-12	2.735E-16	5.638E-12	
180	1273	1.15	8.145E-12	2.361E-14	1.515E-18	8.614E-14	
180	1373	2.15	1.458E-10	5.938E-13	2.460E-17	8.115E-13	
180	1473	3.61	1.765E-09	9.638E-12	2.735E-16	5.638E-12	
540	1273	1.61	8.145E-12	2.361E-14	1.515E-18	8.614E-14	
540	1373	2.63	1.458E-10	5.938E-13	2.460E-17	8.115E-13	
540	1473	4.62	1.765E-09	9.638E-12	2.735E-16	5.638E-12	

where  $D$  is the appropriate solid state diffusion coefficient and the other terms were defined earlier. Table 2 gives the calculated and measured widths at various times and temperatures taken from literature values of the diffusion coefficients. The first two sets of calculated widths, references [42] and [43], are for iron diffusion in  $\text{Fe}_2\text{O}_3$  and the other two are for oxygen diffusion. [44, 45] The data from references [42] and [43] are taken from Kofstad. [46, 47]

The comparison of measured and calculated activation energies based on the predicted and experimental groove widths draw inconclusive results (see Figure 32). However, from Table 2, it is obvious that the calculated grain boundary widths are similar to those measured, particularly for iron diffusion. If volume diffusion is indeed controlling the rate of boundary grooving in air, then it might be expected that the iron would have to diffuse through the solid while oxygen could be transported through the gas phase. As a result, for volume diffusion, rate control by solid state diffusion of the iron would be expected.

For purposes of comparison, Figure 32 gives the measured groove widths after 180 minutes as a function of temperature and those calculated with iron diffusion being the rate-controlling species. [42] The measured and calculated values are within roughly a factor of two of each other but the apparent activation energies are different. These activation energies were calculated from the least squares fit to the three data points. The apparent activation energy for the calculated widths is slightly less than that for diffusion because of the " $T$ " term in the denominator of the equation. The measured and calculated



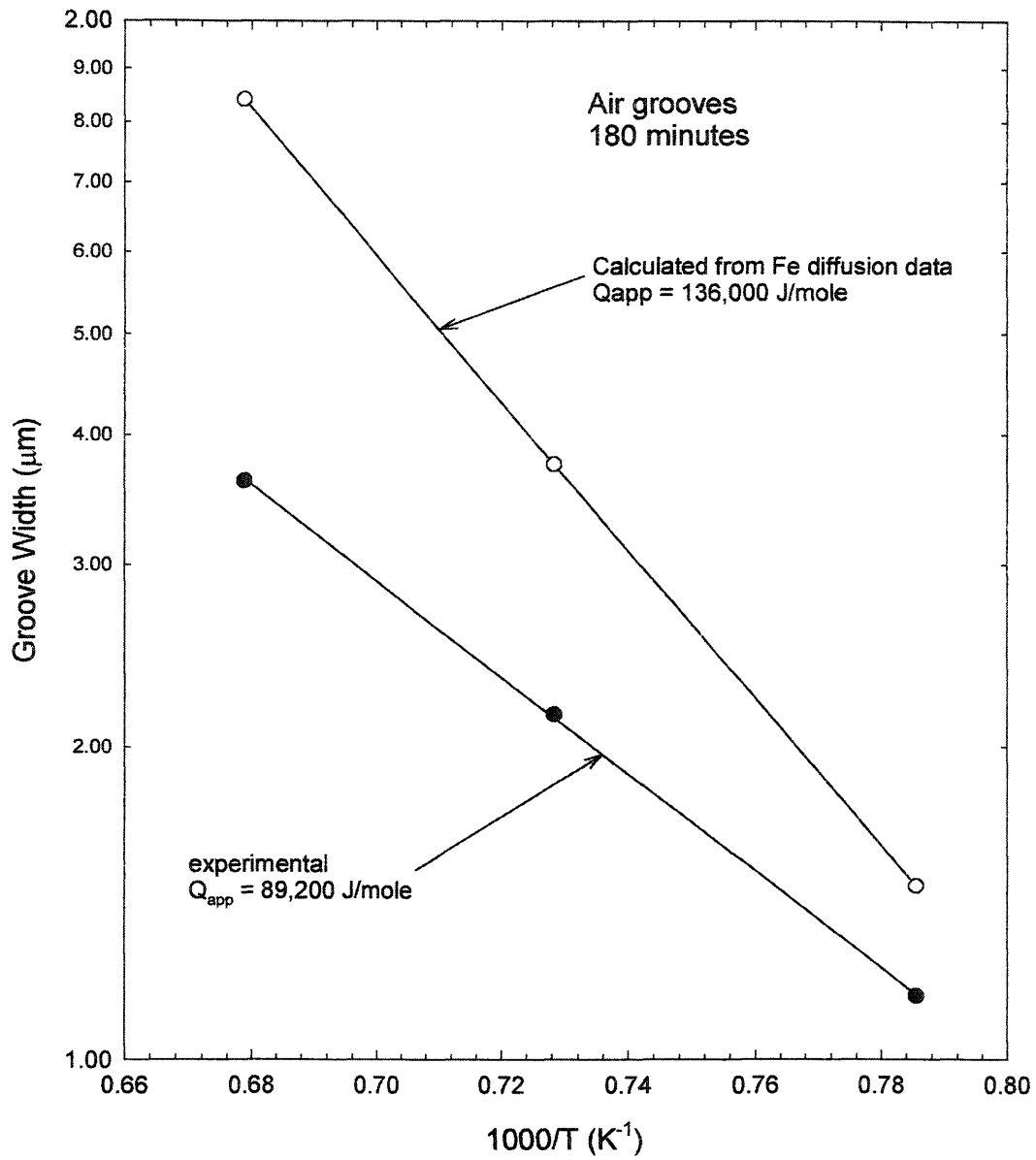


Figure 32: Comparison of Calculated and Experimental Air Groove Data for 180 minutes.

groove values are sufficiently close so that grooving in air by volume diffusion in the solid cannot be ruled out as the rate-controlling mechanism for grooving in  $\text{Fe}_2\text{O}_3$ .

## 6.2 Groove Widths in HCl

The gaseous diffusion coefficient,  $D_{AB}$  for the various product gas species,  $\text{FeCl}_2$ ,  $\text{FeCl}_3$ , and  $\text{H}_2\text{O}$  in argon were calculated from the kinetic theory of gases with the following equation: [2]

$$D_{AB} = \frac{2}{3} \left( \frac{k}{\pi} \right)^3 \left( \frac{1}{2m_A} + \frac{1}{2m_B} \right)^{\frac{1}{2}} \frac{T^{\frac{3}{2}}}{p \left( \frac{d_A + d_B}{2} \right)^2}$$

where  $m_i$  = the molecular masses,  $d_i$  = molecular diameters, and  $p$  = total pressure. The simple kinetic theory of gases was used rather than the Chapman-Enskog modification [p.25, 13] simply because the interaction parameters for the gases are not known in order to apply the latter model. The calculated values are given in Table 3. Two values for the diffusion coefficient for each of the iron chlorides is given based on the different molecular diameters obtained assuming either ionic or covalent bonding in the molecules. The ionic and covalent radii were taken from literature data. [48] A linear molecule was assumed for  $\text{FeCl}_2$  so that the molecular diameter  $d(\text{FeCl}_2) = d(\text{Fe}) + 2 d(\text{Cl})$ . For  $\text{FeCl}_3$  a triangular molecule was assumed which gives the same diameter as for  $\text{FeCl}_2$ .

### 6.2.1 Comparison of Calculated and Measured Groove Widths

Table 3 contains the calculated diffusion coefficients and calculated groove widths based on Mullins' model: [21]

**TABLE 3**  
**Calculation of Gas Diffusion Coefficients of FeCl<sub>2</sub> and FeCl<sub>3</sub> in A**

FeCl <sub>2</sub> -Ar	linear molecule	di(FeCl <sub>2</sub> )=	6.28E-10	M(FeCl <sub>2</sub> )=	1.27E-01 kg/mole			
FeCl <sub>3</sub> -Ar	triangular molecule	dc(FeCl <sub>2</sub> )	8.88E-10	M(Ar)=	3.99E-02			
		d(Ar)=	3.48E-10	M(FeCl <sub>3</sub> )=	1.62E-01			
		di(FeCl <sub>3</sub> )=	6.28E-10	M(H <sub>2</sub> O)=	1.80E-02			
		dc(FeCl <sub>3</sub> )=	8.88E-10					
		d(H <sub>2</sub> O)=	2.64E-10					
T(oC)	T(K)	Ionic Diameter	Covalent Diameter	Ionic Diameter	Covalent Diameter	D(Ar-H <sub>2</sub> O)(m <sup>2</sup> /s)		
500	773	Di(FeCl <sub>2</sub> -Ar)(m <sup>2</sup> /s)	Dc(FeCl <sub>2</sub> -Ar)(m <sup>2</sup> /s)	Di(FeCl <sub>3</sub> -Ar)(m <sup>2</sup> /s)	Dc(FeCl <sub>3</sub> -Ar)(m <sup>2</sup> /s)	6.939E-05		
600	873	1.744E-05	1.087E-05	1.698E-05	1.059E-05	8.329E-05		
700	973	2.093E-05	1.305E-05	2.038E-05	1.270E-05	9.800E-05		
800	1073	2.463E-05	1.536E-05	2.397E-05	1.495E-05	1.135E-04		
900	1173	2.852E-05	1.778E-05	2.776E-05	1.731E-05	1.297E-04		
1000	1273	3.260E-05	2.033E-05	3.173E-05	1.979E-05	1.467E-04		
1100	1373	3.686E-05	2.298E-05	3.588E-05	2.237E-05	1.643E-04		
1200	1473	4.128E-05	2.574E-05	4.019E-05	2.506E-05	1.825E-04		
1300	1573	4.587E-05	2.860E-05	4.466E-05	2.785E-05	2.014E-04		
		5.062E-05	3.157E-05	4.928E-05	3.073E-05			
		Gamma =	1.00E+00 J/m <sup>2</sup>					
		Molar Volume=	3.05E-05 m <sup>3</sup> /mole					
		w air anneal (m)	1.21E-06 m					
T(oC)	T(K)	p(FeCl <sub>2</sub> )	P(FeCl <sub>3</sub> )	Total p	w (FeCl <sub>2</sub> ,c) (m)	w (FeCl <sub>3</sub> ,i) (m)	w (FeCl <sub>3</sub> ,c) (m)	w (FeCl <sub>3</sub> ,c) (m)
500	773	7.37E-06	2.02E-04	2.09E-04	2.86190E-06	2.48162E-06	8.33913E-06	7.12866E-06
600	873	3.67E-05	3.09E-04	3.46E-04	4.69219E-06	4.02242E-06	9.41272E-06	8.04492E-06
700	973	1.21E-04	3.82E-04	5.03E-04	6.83179E-06	5.84306E-06	9.92024E-06	8.47816E-06
800	1073	2.99E-04	4.05E-04	7.04E-04	9.07721E-06	7.75854E-06	9.95182E-06	8.50512E-06
900	1173	6.31E-04	3.76E-04	1.01E-03	1.14670E-05	9.79879E-06	9.56599E-06	8.17575E-06
1000	1273	1.27E-03	3.00E-04	1.57E-03	1.42792E-05	1.22005E-05	8.75405E-06	7.48274E-06

$$w^3 - w_0^3 = 125 \gamma D \left( \frac{\Omega}{RT} \right)^2 p t$$

where  $w_0$  = groove width formed during the air anneal. The surface energy was again assumed to be  $1 \text{ J/m}^2$ .

In Figure 33 are plotted the experimental and calculated results for the groove widths as a function of temperature for a constant time of 10 minutes in 0.025 atm HCl in Ar. The calculated values for the covalently-bonded molecules were chosen simply because they are slightly closer to the experimental values. The most important thing to note about the calculated and experimental data is that the actual groove widths are not too different, only about a factor of two or so. Given the uncertainty in many of the parameters in the Mullins equation this is reasonably good agreement. However, the higher apparent activation energy for the experimental grooves and the fact that they are smaller than those predicted by diffusion in the gas, suggests that perhaps a surface reaction is playing a large role in groove formation. This would not be unexpected at these relatively low temperatures.

On the other hand, the molecular mean free path in argon at 973 K, which can be calculated from: [49]

$$\lambda = \frac{RT}{\sqrt{2}\pi \left( \frac{d}{2} \right)^2 N_A p}$$

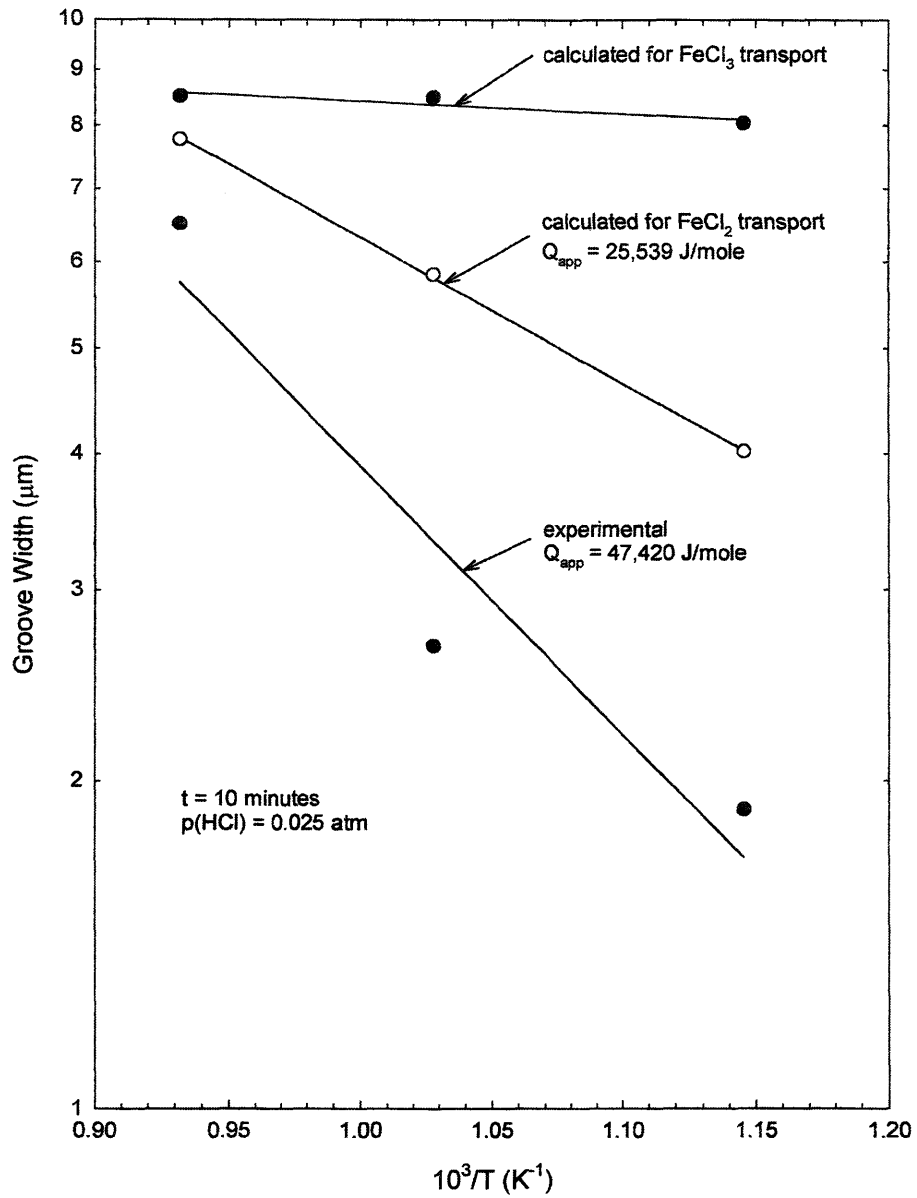


Figure 33: Comparison of Calculated and Experimental HCl Groove Data for 10 minutes

where  $\lambda$  = mean free path and  $N_A$  = Avogadro's number, is on the order of 1  $\mu\text{m}$ . This is on the same order as the groove widths. Therefore, Mullins' model really does not apply since it assumes that the mean free path is small compared to the size of the groove.

However, taking into account a mean free path on the order of the groove size might be expected to make some changes to the details of the groove shape but not affect significantly the groove size. Nevertheless, a model needs to be developed in which the mean free path of the gas is considered.

### 6.3 Comparison of Grain Boundary Grooving and Weight Loss

A more common way to measure the kinetics of active gas corrosion is by weight loss as a function of time. However, measurement of corrosion kinetics by grain boundary grooving can be a much more sensitive way to measure low rates of corrosion. For example, at 600 °C (873 K) in 0.025 atm HCl in Ar, the calculated groove width is about 4  $\mu\text{m}$ . As can be seen from the many AFM scans presented here, a groove of this size is very easily measured. However, in the case of weight loss under the same conditions (0.025 atm HCl in Ar, 10 min. at 873 K) if a spherical sample 3 mm in diameter is considered, then the amount of weight loss,  $\Delta m$ , as derived from Fick's first law of diffusion, is given by:

$$\Delta m = -\frac{2\pi d D M}{RT} p t$$

where  $M$  is the molecular weight and  $p$  is the pressure of the diffusing iron chloride. For  $\text{FeCl}_2$  diffusion and the data in Table 3, a weight loss of about 1  $\mu\text{g}$  is predicted. This is

about the limit of measurement for a microbalance. At this elevated temperature and in the corrosive atmosphere of HCl, making good measurements to a 1  $\mu\text{g}$  accuracy is extremely difficult. Therefore, grain boundary grooving is a far easier technique to implement to measure low corrosion rates.

## CHAPTER 7

### CONCLUSIONS

#### 7.1 Summary

Several conclusions were formed from the comparison of experimental with predicted data and thermodynamic analysis for grain boundary grooving.

Despite first impressions of the grooves of  $\text{Fe}_2\text{O}_3$  formed in air, when comparing the data to literature, the values were sufficiently close to Fe diffusion through solid phase predictions (oxygen would most likely be transported through the gas phase). Consequently, grain boundary grooving was most likely controlled by solid phase volume diffusion (of the Fe).

Grain boundary grooves formed in the 0.025 atm HCl atmosphere were compared to calculated data, which gave way to the following deductions:

- 1) The experimental data is relatively close, within a factor of two, to that calculated by Mullins model for gas diffusion control. This strongly suggests diffusion is playing an important rate in grooving kinetics, which is surprising at such low temperatures.
- 2) Because the experimental activation energy is higher and the grooves are smaller than that predicted by Mullins gas diffusion model, indicates that a surface reaction may also be involved in groove formation in combination with gas diffusion.



- 3) Mullins model is not exactly applicable in the groove formation of  $\text{Fe}_2\text{O}_3$  because the mean free path (in argon) is on the same order of magnitude as the actual groove widths.

Finally, with respect to other methods, grain boundary grooving is a practical and relatively sensitive technique for measuring low corrosion rates of ceramics.

## 7.2 Recommendations for Future Work

In light of the above, further steps should be taken to better understand grooving and corrosion kinetics.

- 1) It is obvious that more ceramic systems should be investigated under similar conditions.
- 2) Experimental efforts can be directed towards insight to groove width variation with time in HCl.
- 3) Also, weight loss measurements, in conjunction with groove data, would prove to be valuable.
- 4) Moreover, a model which includes the mean free path of the gas needs to be developed.

## REFERENCES CITED

1. B. Piasecki, D. Rainey, and K. Fletcher, "Is Combustion Of Plastics Desirable?," *American Scientist* **86** 364-373 (1998).
2. R. B. Bird, W. E. Stewart, and E. N. Lightfoot, Transport Phenomena, New York: Wiley, 1960.
3. D. W. Readey and A. R. Cooper, Jr., "Molecular Diffusion with a Moving Boundary and Spherical Symmetry," *Chem. Eng. Sci.*, **21** 917 (1966).
4. J. W. Evans, "Gas-Solid Reactions: The Viscous Flow Term," *Canad. J. Chem. Eng.*, **50** [12] 811-814 (1972).
5. J. W. Evans and S. Song, "Gas-Solid Reactions: The Viscous Flow Term (Non-Equimolar Fluxes)," *Canad. J. Chem. Eng.*, **51** [10] 616-617 (1973).
6. Landolt-Bornstein, Numerical Data and Functional Relationships in Science and Technology, **26**, ed. by Mehrer, 1990.
7. A. R. Cooper, Jr. and W. D. Kingery, Kinetics of High Temperature Processes, ed. by W. D. Kingery, M.I.T., Cambridge, 1959.
8. W. M. Rohsenow and H. Choi, "Heat, Mass and Momentum Transfer," p. 148, Prentice Hall, 1961.
9. V. Bheemineni, "Gaseous Corrosion of Magnesium Oxide in Hydrogen," Ph.D. Thesis, The Ohio State University, Columbus, OH (1984).

10. W. W. Mullins, "Theory of Thermal Grooving," *J. Appl. Phys.*, **28** [3] 333-339 (1957).
11. A. W. Adamson, Physical Chemistry of Surfaces, 4<sup>th</sup> ed., New York: Wiley, 1982.
12. R. J. Fruehan, "The Rate of Chlorination of Metals: Part I. Fe, Ni, Sn, in Chlorine," *Met. Trans.*, **31** 2585 (1972).
13. C. J. Geankoplis, Mass Transport Phenomena, Columbus: C. Geankoplis, 1972.
14. D. R. Stull and H. Prophet, H. JANAF Thermochemical Tables, 2<sup>nd</sup> ed., Washington, D.C.: National Bureau of Standards, June 1971; Report No. NSRDS-NB537.
15. J. P. Hirth, Evaporation and Sublimation Mechanisms in Margrave, J. L., ed. The Characterization of High Temperature Vapors, New York: Wiley, 1967:43.
16. K. J. Laidler, Chemical Kinetics, 3<sup>rd</sup> ed., New York: Harper and Row, 1987.
17. J. W. Moore and R. G. Pearson, Kinetics and Mechanisms, 3<sup>rd</sup> ed., New York: Wiley, 1981.
18. F. A. Cotton and G. Wilkinson, Advanced Inorganic Chemistry, 4<sup>th</sup> ed., New York: Wiley, 1980: 1183-1233.
19. B. Douglas, D. H. McDaniel, and J. J. Alexander, Concepts and Models of Inorganic Chemistry, 2<sup>nd</sup> ed., New York: Wiley, 1983.
20. B. C. Allen, "Kinetics of Grain Boundary Grooving in Chromium, Molybdenum, and Tungsten," *Trans. of the Metallurgical Soc. of AIME* **245** 1621-1632 (1969).

21. W. W. Mullins, "Grain Boundary Grooving by Volume Diffusion," *Trans. AIME*, **218** 354-361 (1960).
22. D. W. Readey and R. E. Jech, "Energies and Grooving Kinetics of [001] Tilt Boundaries in Nickel Oxide," *J. Am. Ceram. Soc.*, **51** [4] 201-208 (1968).
23. R. T. King and W. W. Mullins, "Theory of the Decay of a Surface Scratch to Flatness," *Acta Metallurgica*, **10** 601-606 (1962).
24. W. W. Mullins, "Flattening of a Nearly Planar Solid Surface due to Capillarity," *J. Appl. Phys.*, **30** [1] 77-83 (1959).
25. W. W. Mullins, "Theory of Linear Facet Growth During Thermal Etching," *Phil. Mag.*, 1313-1341 (1961).
26. W. W. Mullins, "The Effect of Thermal Grooving on Grain Boundary Motion," *Acta Metallurgica*, **6** 414-427 (1958).
27. F. Y. Genin, W. W. Mullins, and P. Wynblatt, "The Effect of Stress on Grain Boundary Grooving," *Acta Metallurgica*, **41** [12] 3541-3547 (1993).
28. D. J. Aldrich, "Microstructural Effects in Vapor Phase Sintering," Ph.D. Thesis, Colorado School of Mines, Golden, CO (1997).
29. D. S. Park, M. J. McNallan, C. Park and W. W. Liang, "Active Corrosion of Sintered  $\alpha$ -Silicon Carbide in Oxygen-Chlorine Gases at Elevated Temperatures," *J. Am. Ceram. Soc.*, **73** [5] 1323-1329 (1990).
30. R. R. Sickafoose, Jr. and D. W. Readey, "Active Gaseous Corrosion of Porous Silicon Carbide," *J. Am. Ceram. Soc.*, **76** [2] 316-324 (1993).

31. W. C. Say and S. C. Liu, "Gaseous Corrosion Mechanisms of Silicon Carbides in  $\text{Na}_2\text{SO}_4$  and  $\text{V}_2\text{O}_5$  Environments," *J. Materials Science*, **31** 3003-3008 (1996).
32. D. W. Readey, "High Temperature Gas Corrosion of Ceramic Composites," unpublished.
33. D. W. Readey, "Modeling Corrosion of Ceramics in Halogen-Containing Atmospheres," unpublished.
34. W. M. Robertson, "Grain-Boundary Grooving by Surface Diffusion for Finite Surface Slopes," *J. Appl. Phys.*, **42** [1] 463-467 (197-1).
35. W. M. Robertson, "Thermal Etching and Grain-Boundary Grooving of Silicon Ceramics," *J. Am. Ceram. Soc.*, **64** [1] 9-13 (1981).
36. C. A. Handwerker, J. M. Dynys, R. M. Cannon, and R. L. Coble, "Metal Reference Line Technique for Obtaining Dihedral Angles from Surface Thermal Grooves," *J. Am. Ceram. Soc.*, **73** [5] 1365-1370 (1990).
37. C. A. Handwerker, J. M. Dynys, R. M. Cannon, and R. L. Coble, "Dihedral Angles in Magnesia and Alumina: Distributions from Surface Thermal Grooves," *J. Am. Ceram. Soc.*, **73** [5] 1371-1377 (1990).
38. A. Tsoga and P. Nikolopoulos, "Groove Angles and Surface Mass Transport in Polycrystalline Alumina," *J. Am. Ceram. Soc.*, **77** [4] 954-960 (1994).
39. D. J. Aldrich, D. W. Readey and A. Roshko, "Grain Boundary Grooving in a Reactive Atmosphere," submitted for publication.

40. M. Jin, E. Shimada, and Y. Ikuma, "Grain Boundary Grooving by Surface Diffusion in SrTiO<sub>3</sub> Bicrystal," *J. Mater. Res.*, **14** [6] 2548-2553 (1999).
41. HSC Chemistry for Windows, Outokumpu Research, PO Box 60, FIN-28101 Pori, FINLAND.
42. I. Izvekov, *Sov. Phys.-Solid State*, **8** 706 (1996).
43. R. Lindner, "Diffusion of Radioactive Iron in Iron (III) Oxide and Zinc-Iron Spinel," *Ark. Kemi*, **4** [4] 381-384 (1952).
44. W. C. Hagel, "Oxygen-Ion Diffusion in Hematite," *Trans. AIME*, **236** [2] (1966).
45. K. P. R. Reddy and A. R. Cooper, "Oxygen Diffusion in MgO and  $\alpha$ -Fe<sub>2</sub>O<sub>3</sub>," *J. Am. Ceram. Soc.*, **66** [9] 664-666 (1983).
46. P. Kofstad, *High Temperature Corrosion*, (Elsevier, NY), 113-114 (1988).
47. P. Kofstad, *Nonstoichiometry, Diffusion, and Electrical Conductivity in Binary Metal Oxides*, (Wiley, NY) 235-237 (1972).
48. J. Emsley, *The Elements*, 3<sup>rd</sup> Ed., (Clarendon Press, Oxford), 1988.
49. D. A. McQuarrie and J. D. Simon, *Physical Chemistry, A Molecular Approach*, (University Science Books, Sausalito), 1033 (1997).
50. Dr. Dennis W. Readey, Colorado School Mines, Metallurgical and Materials Department, Colorado Center for Advanced Ceramic Research, Golden, CO 80401

## APPENDIX A

### Error Analysis of Groove Measurements

As displayed in the groove width plots provided in figures 28 through 35, the error of groove measurements was presented in terms of standard error. The figure on the following page illustrates single measurements taken along a groove. As seen from the digital readout (right hand side), the width measurements, “horizontal distance,” are all equal, thus reaffirming the accuracy of measurement. With that in mind, the standard error represents the range of the groove width values across a sample surface *and not the error in measurement*. Standard error was determine by:

$$\text{Std error} = [ \Sigma(x_i - \bar{x})^2 / (n-1) ]^{1/2} / n^{1/2}$$

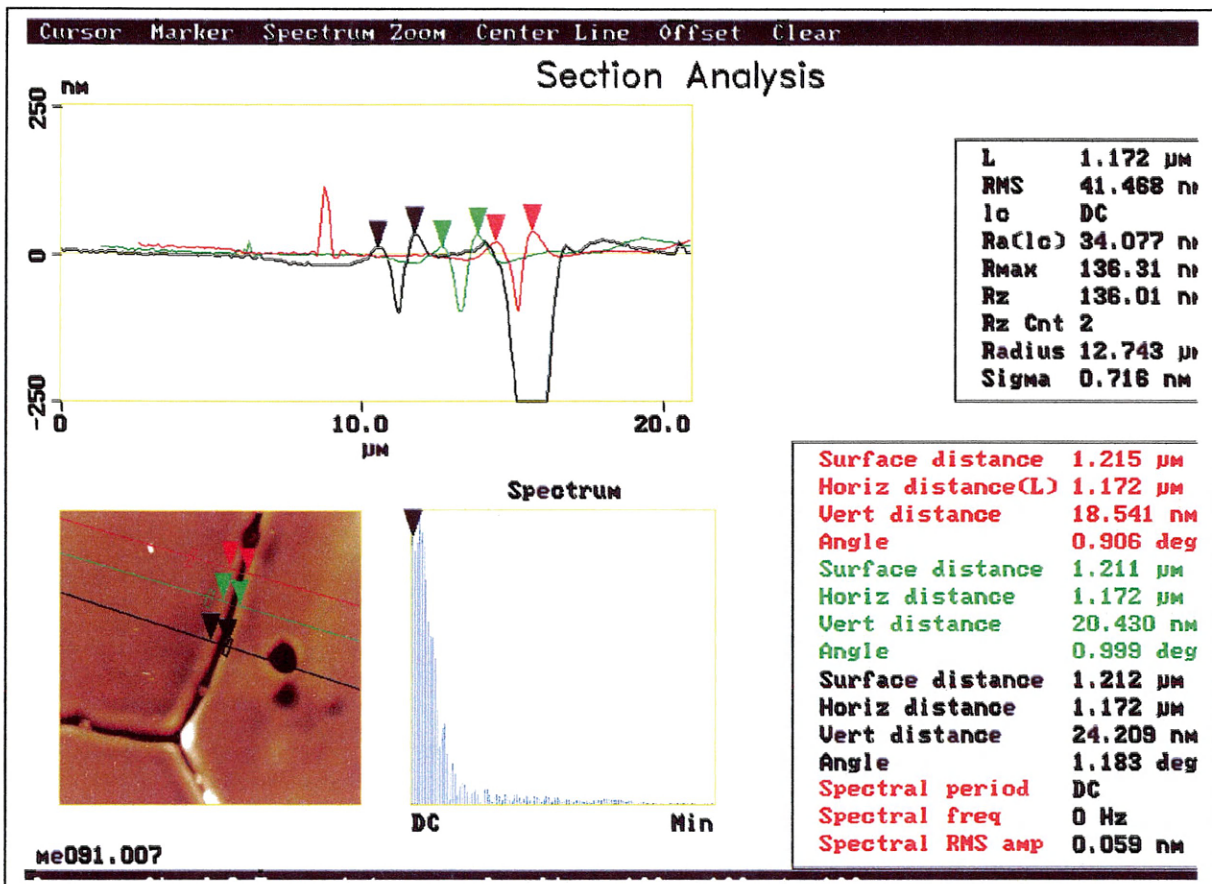
Where  $x_i$  is a width value,  $\bar{x}$  is the sample mean, and  $n$  is the sample size.

$$\text{Mean} (\bar{x}) = \Sigma x_i / n$$

Furthermore, there are a couple of limitations identified in the AFM equipment that can cause error. Within the hardware, the piezoelectric scanner tube, which propels the AFM tip back and forth across the sample surface, has an “uncorrected Z-bow” at large scan sizes. The bow is an error in the tip height measurement of roughly 2 nm at a 10  $\mu\text{m}$  scan size and 50 nm at a 90  $\mu\text{m}$  scan size. This should be noted because the width measurements are taken between the grooves’ peaks. The other error is due to the geometry of the cantilever tip. The tip is pyramidal in shape and cannot accurately measure angles steeper than 60° leading edges and 72° trailing edges. However, by virtue

of the fact that the measurements being made here are for width and not dihedral angles,  
the error is minor.



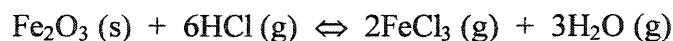


Nanoscope Software analysis of AFM Data. A demonstration in accuracy.

## APPENDIX B

### Thermodynamic Calculations

HSC Chemistry, a copyright computer program, was employed to create partial pressure plots as a function of temperature for all possible product species of reacting  $\text{Fe}_2\text{O}_3$  (s) with  $\text{HCl}$  (g). The program operated under the following assumptions: 1) constant volume, 2) 1 atm of  $\text{HCl}$  (g), and 3) equilibrium conditions (ex: activity of  $\text{Fe}_2\text{O}_3$  is 1). Also, thermodynamic data in the HSC database can be used to assess the  $\Delta G^\circ$  values, seen below. Succeeding is an example reaction, which was deemed dominant in the temperature range that was investigated.



$$K_e = [ p(\text{FeCl}_3)^2 p(\text{H}_2\text{O})^3 ] / [ a(\text{Fe}_2\text{O}_3) p(\text{HCl})^6 ]$$

$$\Delta G = \Delta G^\circ + RT \ln Q$$

For equilibrium conditions:  $\Delta G = 0$  and  $Q = K_e$

Thus,  $\Delta G^\circ = -RT \ln K_e$

$$p(\text{FeCl}_3) = [ p(\text{HCl})^3 / p(\text{H}_2\text{O})^{3/2} ] \exp ( \Delta G^\circ / 2RT )$$

## APPENDIX C

### Groove Width Data

For 10 minutes of etch time in a HCl atmosphere

Temperature (K)	1073	973	873
Groove Width ( $\mu\text{m}$ )	8.379	3.281	1.777
	8.438	2.305	1.816
	6.973	2.539	2.012
	5.977	3.242	2.012
	6.27	2.695	1.992
	4.492	2.344	1.836
	9.961	2.891	1.719
	6.055	2.461	2.031
	6.055	2.148	1.797
	5.078	3.047	1.758
	5.039	3.32	1.914
	6.797	2.461	1.875
	4.922	2.852	1.992
	6.27	2.539	2.109
		3.086	2.031
		2.695	1.836
		2.5	1.719
		2.461	1.797
		1.992	1.602
		2.773	1.875
	2.227	1.836	
	2.734	2.031	
Width Mean	6.49508	2.66332	1.88032
Standard Error	0.44562	0.07919	0.02793

For 30 minutes etch time in air atmosphere.

Temperature (K)	1273	1373	1473
Groove Width ( $\mu\text{m}$ )	0.23438	1.016	1.445
	0.1563	0.9375	1.406
	0.3516	0.9375	1.406
	0.3516	1.016	1.406
	0.1953	0.9375	1.484
	0.23438	1.016	1.406
	0.3125	1.094	1.484
	0.23438	1.016	1.406
	0.15625	0.9375	1.484
	0.54688	1.016	1.484
	0.15625	1.016	1.484
	0.3516	1.094	1.406
	0.23438	0.9375	1.406
	0.1953	1.094	1.484
	0.3516	1.016	1.484
	0.3125	1.016	1.484
	0.1953	1.016	1.484
	0.1563	1.016	1.406
		1.094	1.484
		1.016	1.406
		1.016	
		0.9375	
		1.094	
		1.016	
		1.016	
		1.094	
		1.016	
		1.016	
Width Mean	0.26635	1.01589	1.44695
Standard Error	0.03565	0.00986	0.00871

For 60 minutes of etch time in an air atmosphere

Temperature (K)	1273	1373	1473
Groove Width ( $\mu\text{m}$ )	1.172	2.656	3.203
	1.172	2.813	3.125
	1.25	2.891	3.359
	1.25	2.813	3.516
	1.25	3.203	3.672
	1.016	3.672	3.594
	1.25	2.813	3.359
	1.172	3.672	3.203
	1.25	3.203	3.125
	1.172	3.438	3.359
	1.25	2.734	3.125
	1.25	2.656	3.203
	1.172	3.359	3.281
	1.172	2.813	3.672
	1.172	3.672	3.438
	1.25	2.266	3.125
	1.25	2.578	3.203
	1.25	2.188	3.125
	1.25	2.891	3.594
	1.25	3.125	3.516
	1.172	3.281	3.164
	1.25	2.734	3.281
	1.25		3.281
	1.172		3.281
	1.172		
1.172			
1.172			
Width Mean	1.20667	2.97595	3.32517
Standard Error	0.01048	0.09019	0.0373

For 180 minutes of etch time in an air atmosphere

Temperature (K)	1273	1373	1473
Groove Width ( $\mu\text{m}$ )	1.172	1.953	3.281
	1.172	1.953	3.984
	1.016	2.344	3.281
	1.172	1.406	3.672
	1.094	2.266	3.594
	1.25	2.109	3.75
	1.172	2.109	3.672
	1.25	2.266	3.281
	1.094	2.266	3.672
	1.094	2.188	3.672
	1.094	1.953	3.672
	1.094	2.422	3.438
	1.094	1.797	3.75
	1.172	2.5	3.672
	1.172	2.266	3.828
	1.172	2.344	3.75
	1.172	2.344	3.672
	1.172	1.875	3.828
	1.172	2.344	3.672
	1.172	2.266	3.516
		2.109	3.75
			3.594
			3.672
		3.281	
		3.281	
Width Mean	1.1486	2.14667	3.6094
Standard Error	0.01278	0.05544	0.03933

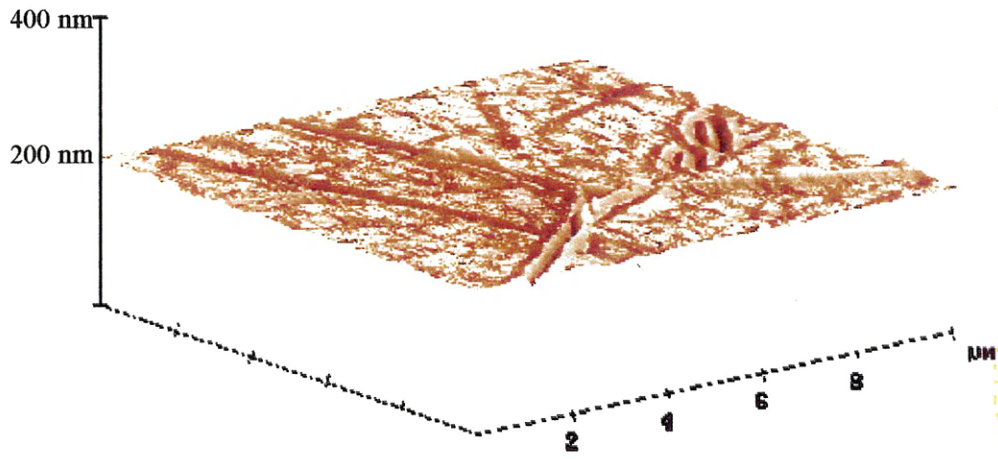
For 540 minutes of etch time in an air atmosphere

Temperature (K)	1273	1373	1473
Groove Width ( $\mu\text{m}$ )	1.563	2.422	4.453
	1.719	2.656	4.844
	1.719	2.266	4.297
	1.406	2.734	4.453
	1.406	2.891	4.609
	1.875	2.656	4.766
	1.563	2.734	4.766
	1.641	2.656	4.766
	1.406	2.656	4.609
	1.719	2.266	4.766
Width Mean	1.6115	2.62688	4.61925
Standard Error	0.0571	0.06911	0.06999

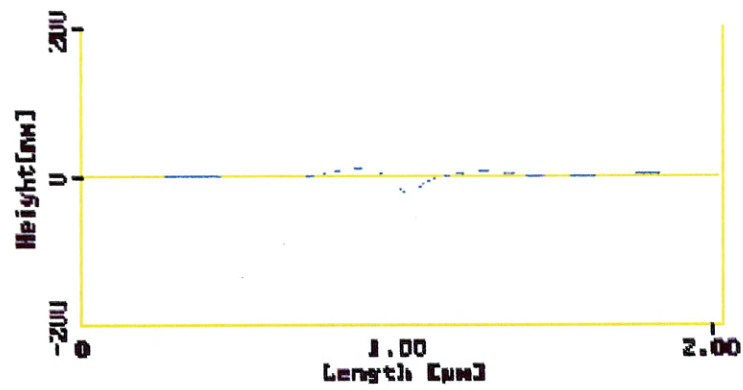
## APPENDIX D

Following are AFM three-dimensional images, AFM groove profiles, and SEM images representative of each air-etched sample between 1273 K and 1473 K for etching times varying between 30 to 540 minutes. These samples were polished prior to etching for an initially flat surface. This minimized preferential etching and, thus, a smaller variation of groove widths along a given sample's surface.

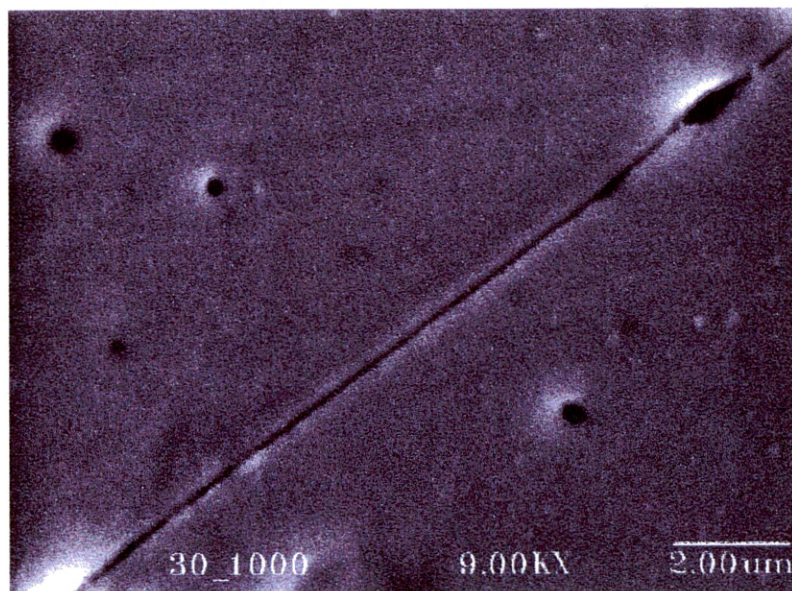




a) 3-dimensional AFM

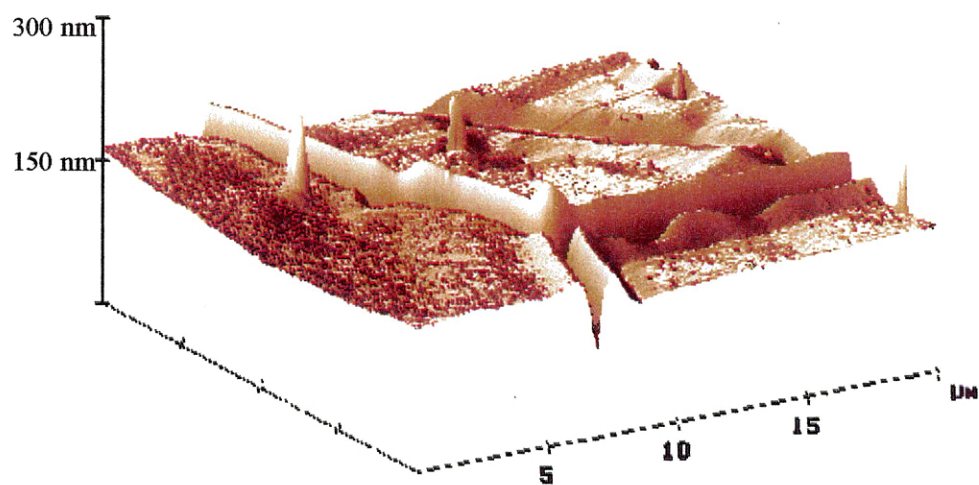


b) AFM groove profile

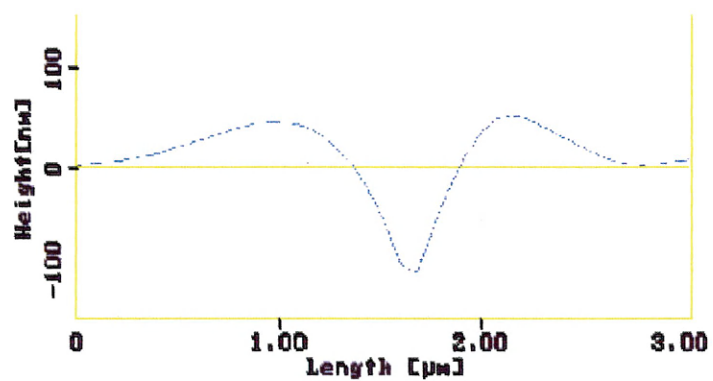


c) SEM

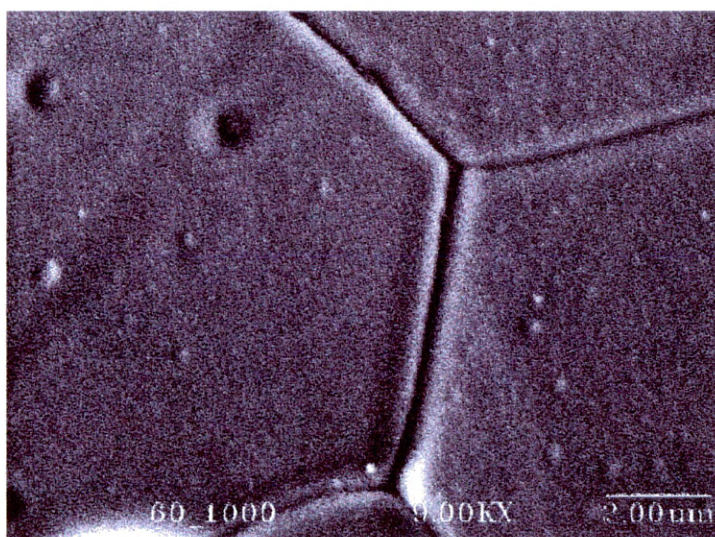
**Air Etched Sample at 1273 K for 30 minutes**



a) 3-dimensional AFM

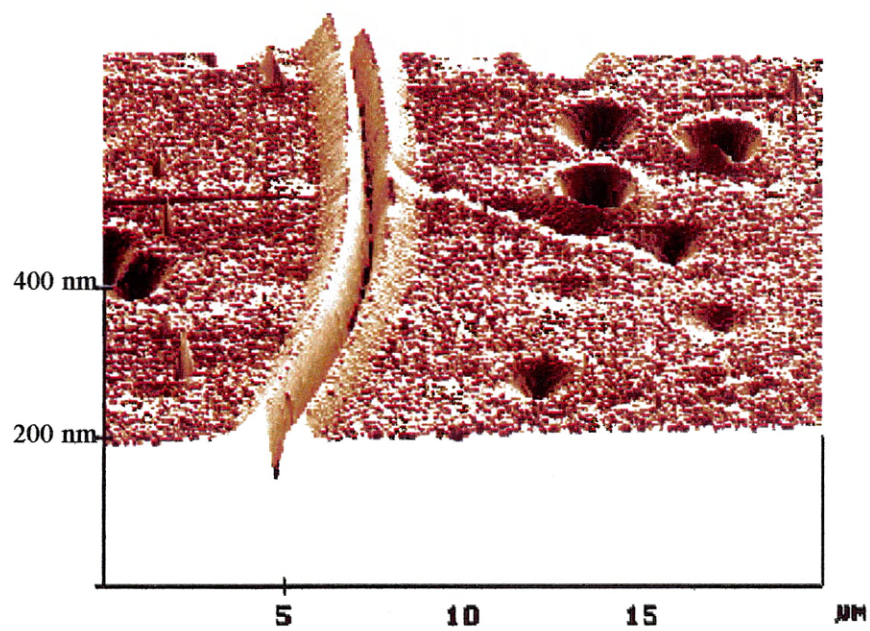


b) AFM groove profile

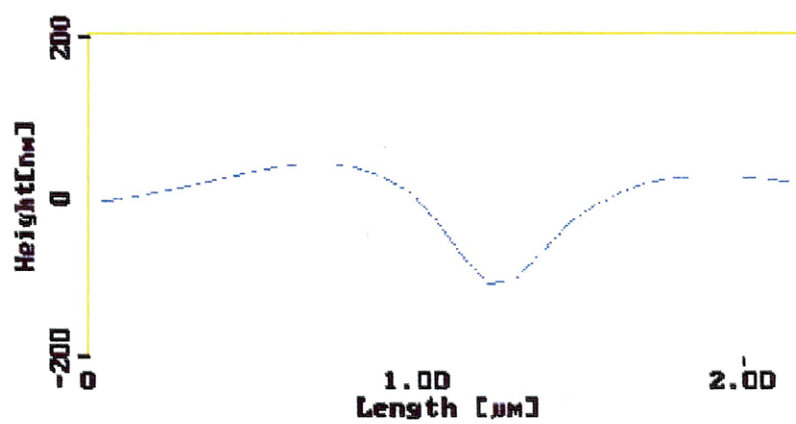


c) SEM

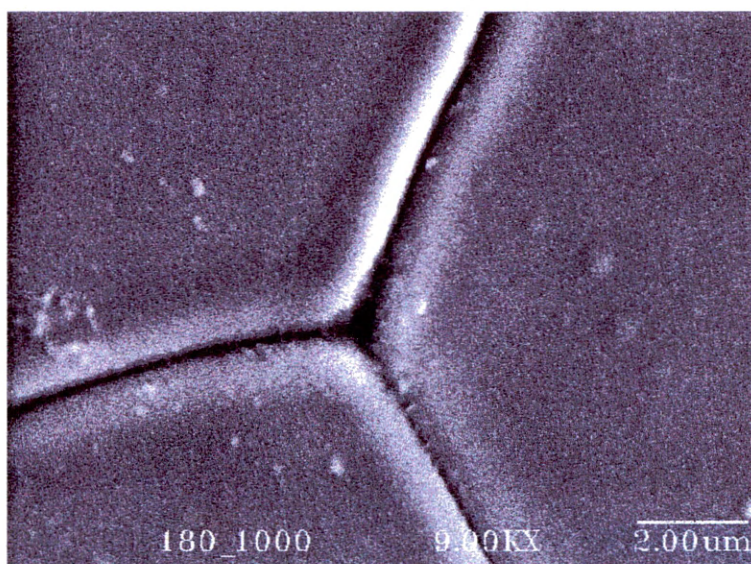
**Air Etched Sample at 1273 K for 60 minutes**



a) 3-dimensional AFM

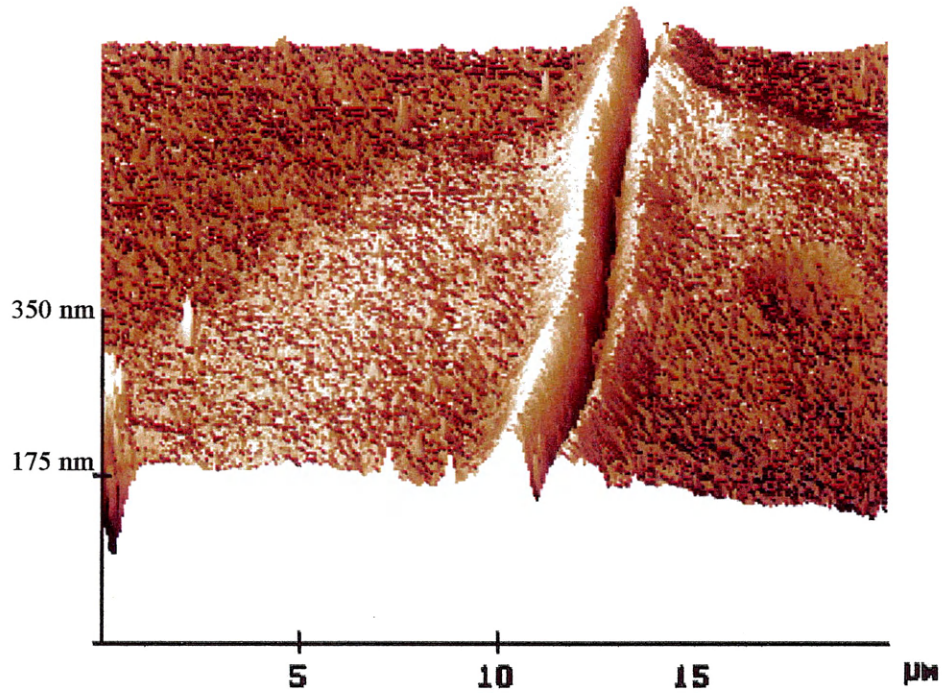


b) AFM groove profile

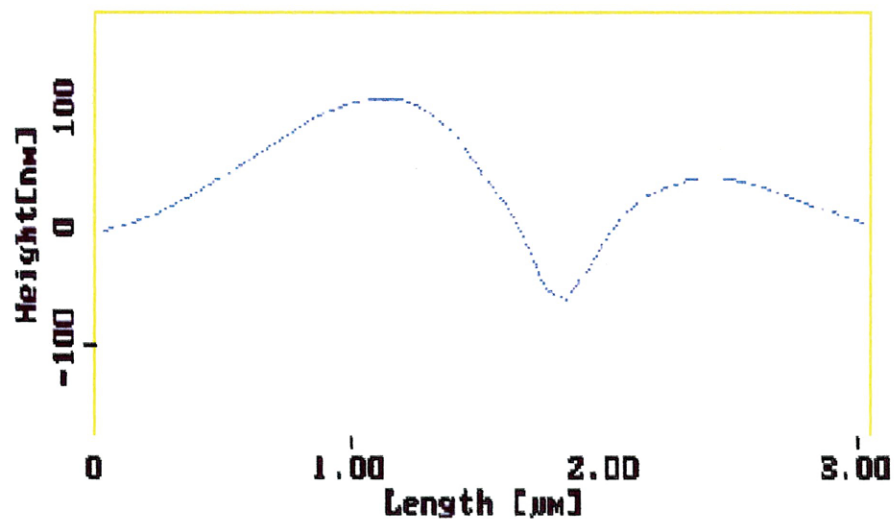


c) SEM

**Air Etched Sample at 1273 K for 180 minutes**

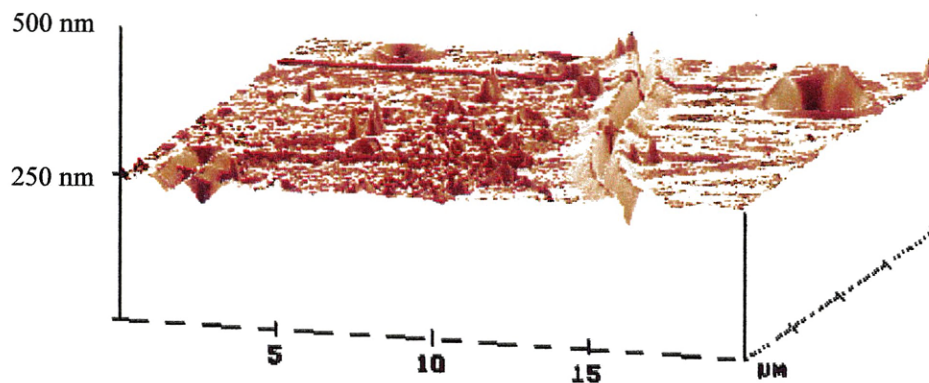


a) 3-dimensional AFM

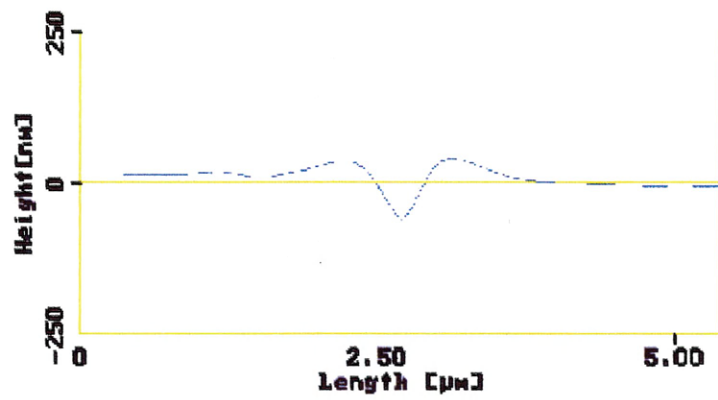


b) AFM groove profile

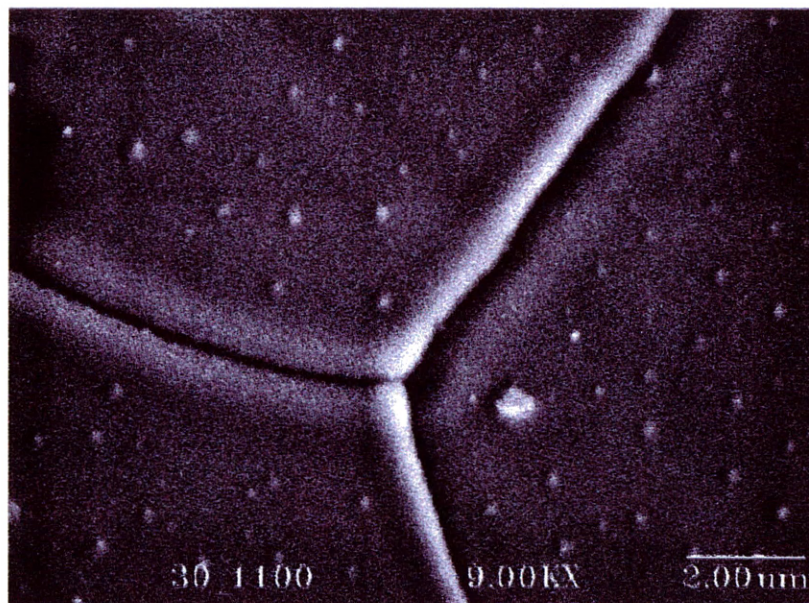
Air Etched Sample at 1273 K for 540 minutes



a) 3-dimensional AFM

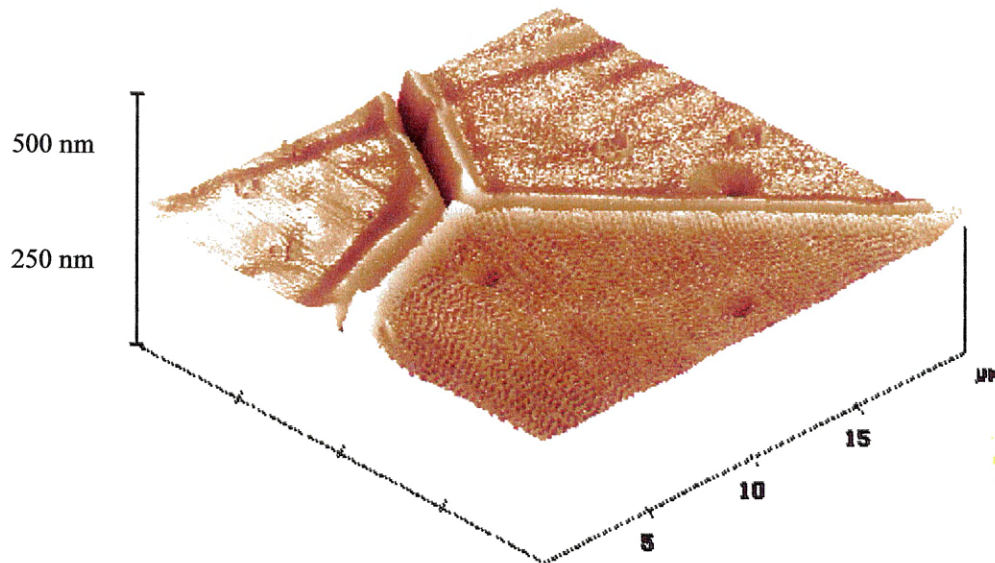


b) AFM groove profile

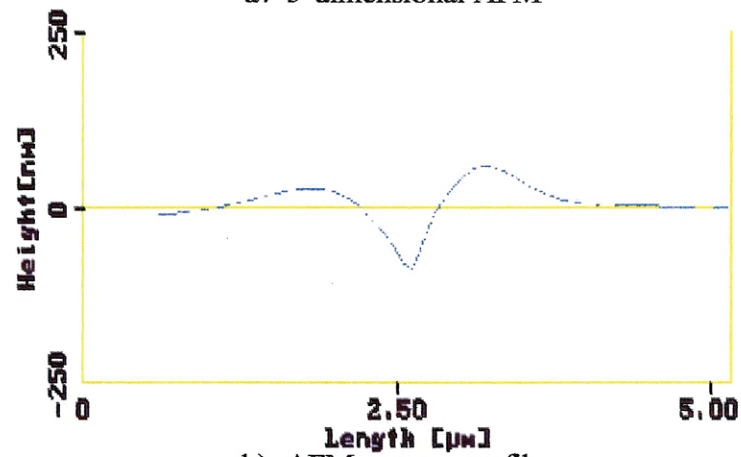


c) SEM

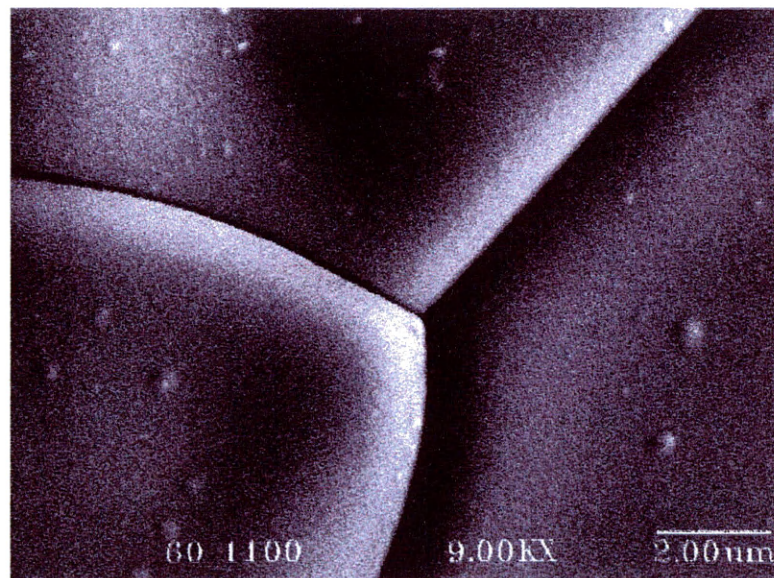
**Air Etched Sample at 1373 K for 30 minutes**



a) 3-dimensional AFM

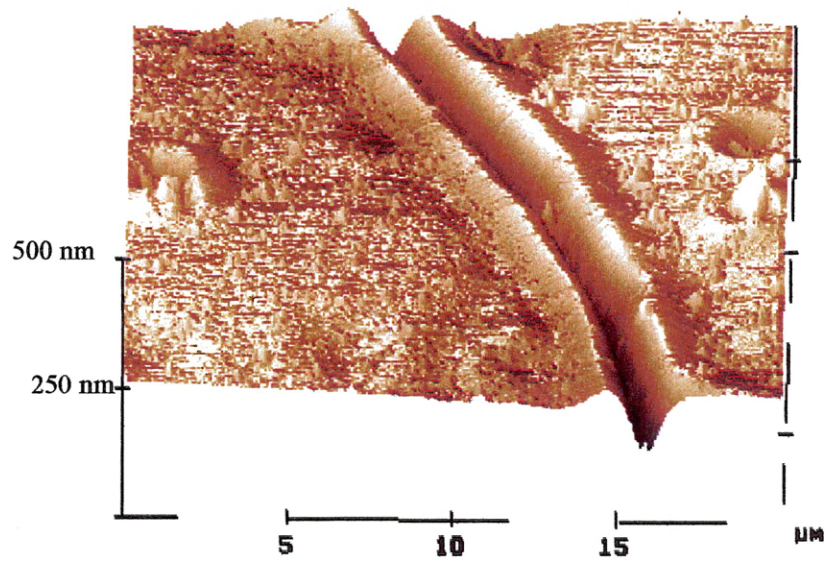


b) AFM groove profile

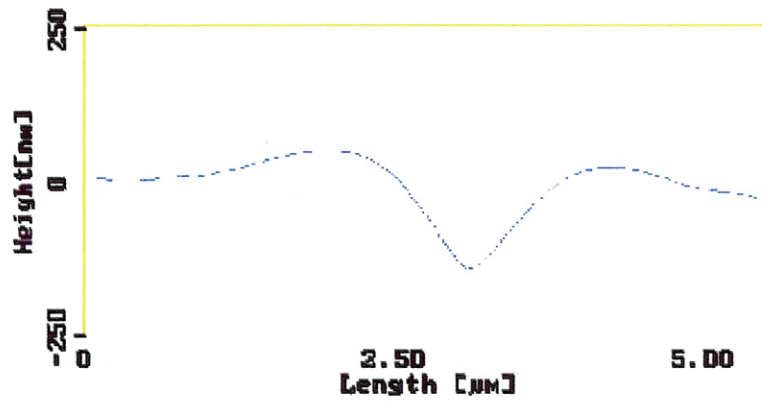


c) SEM

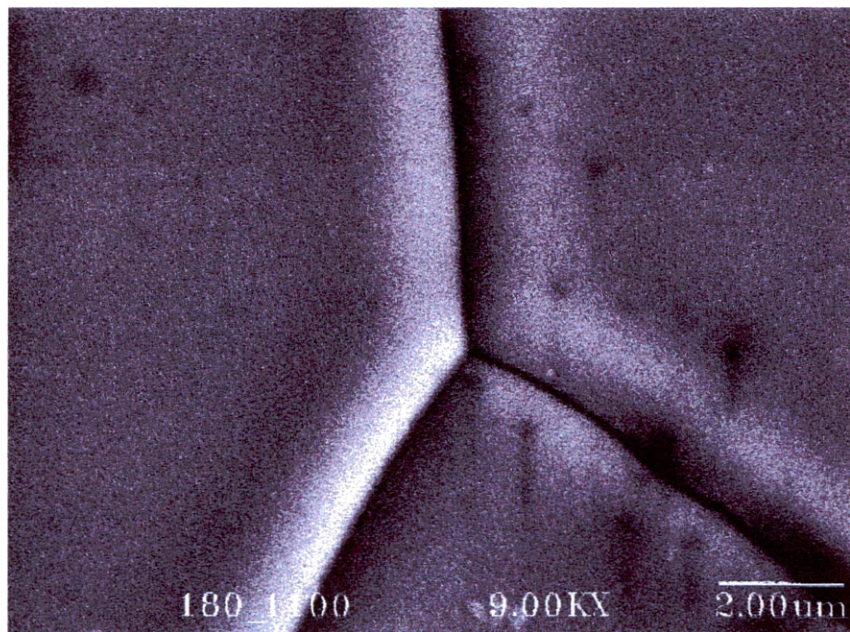
Air Etched Sample at 1373 K for 60 minutes



a) 3-dimensional AFM

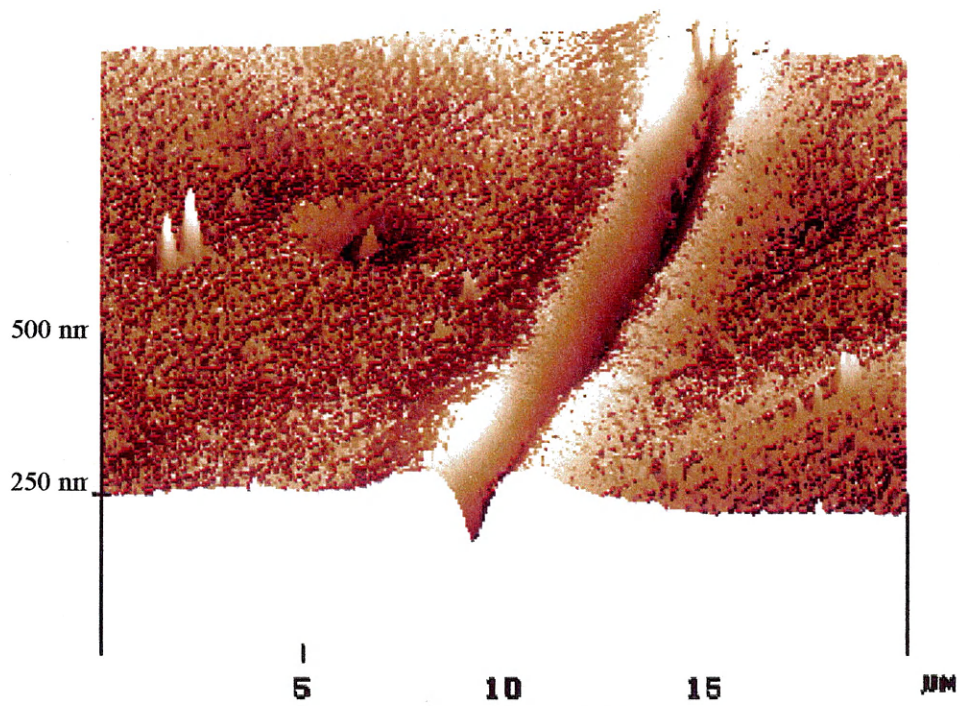


b) AFM groove profile

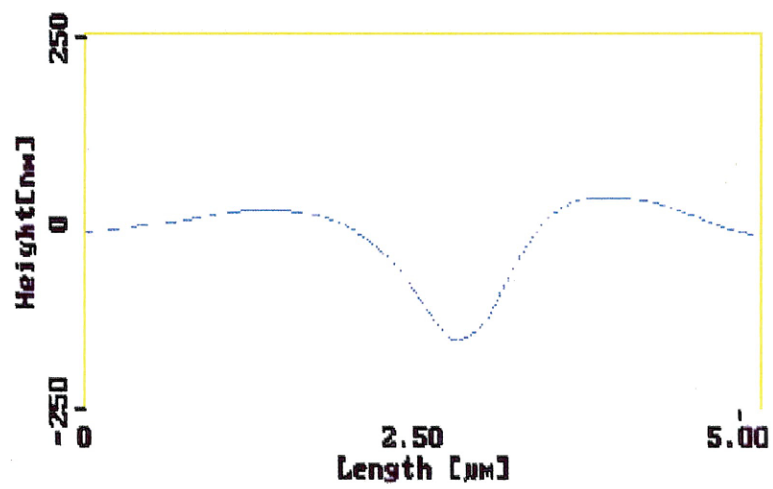


c) SEM

**Air Etched Sample at 1373 K for 180 minutes**



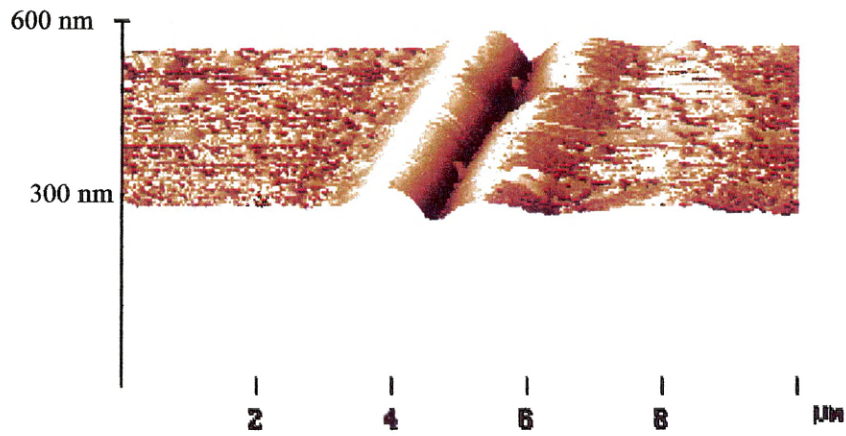
a) 3-dimensional AFM



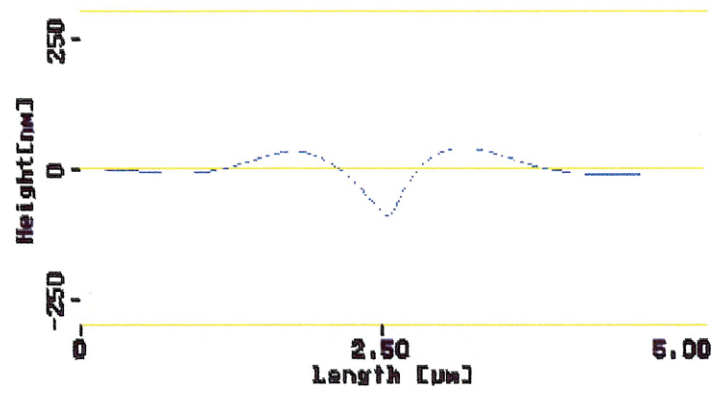
b) AFM groove profile

**Air Etched Sample at 1373 K for 540 minutes**

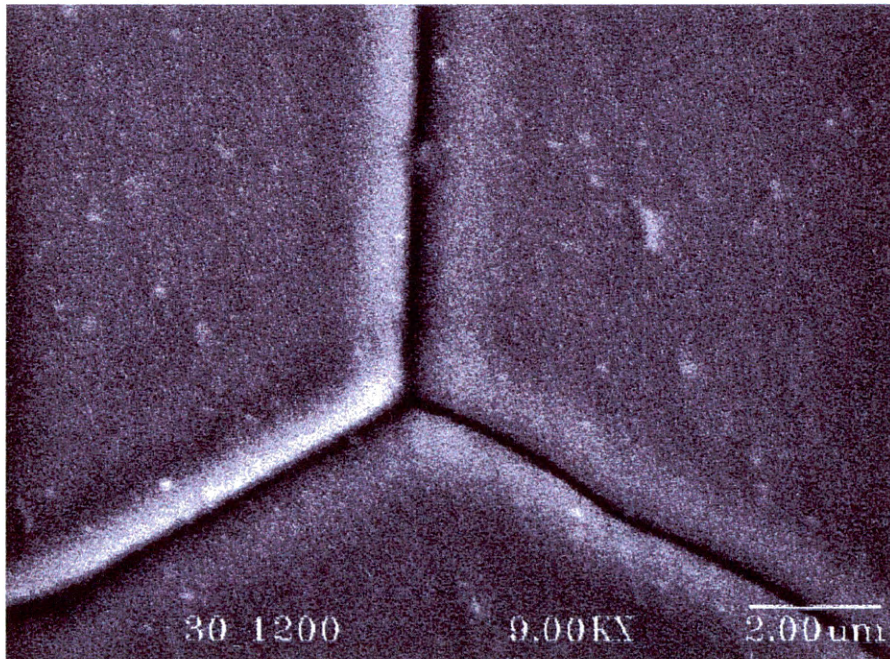




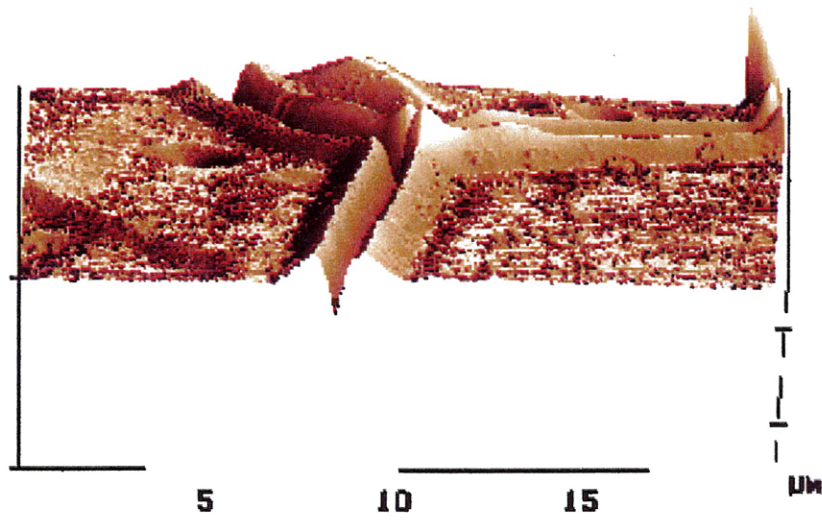
a) 3-dimensional AFM



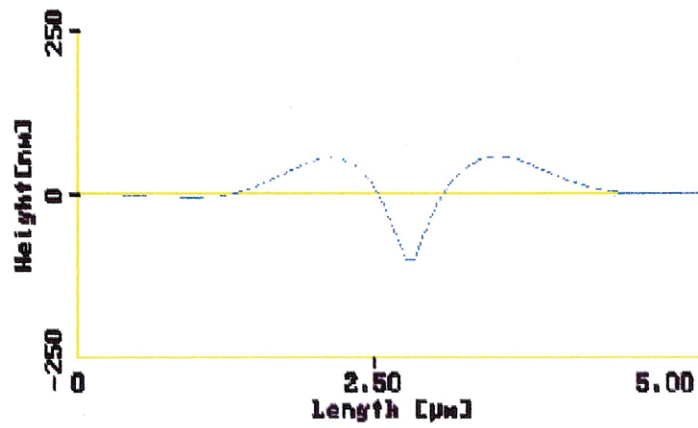
b) AFM groove profile



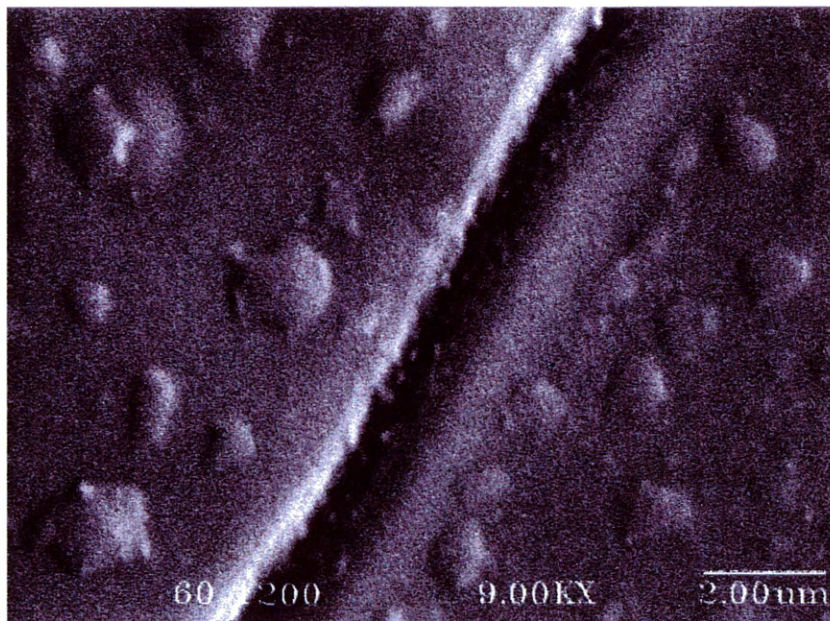
c) SEM



a) 3-dimensional AFM

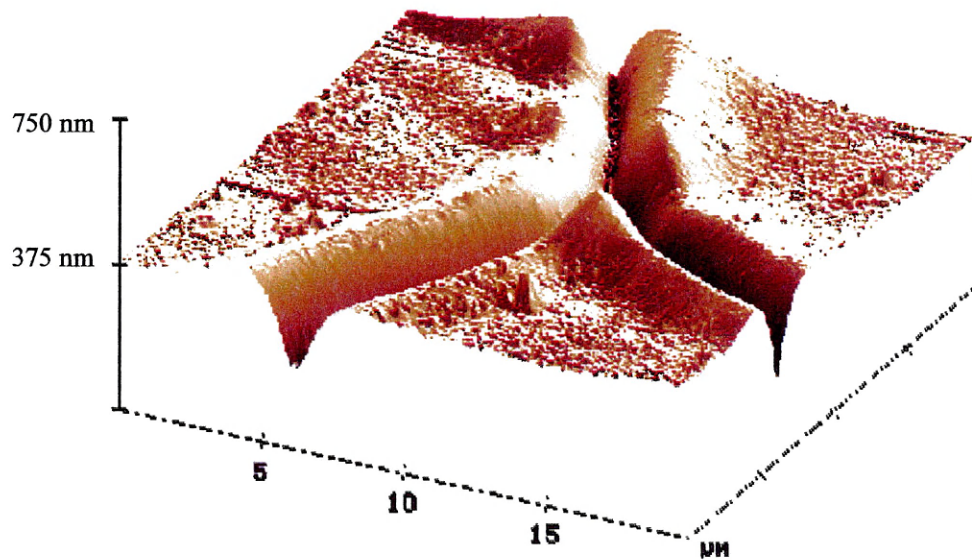


b) AFM groove profile

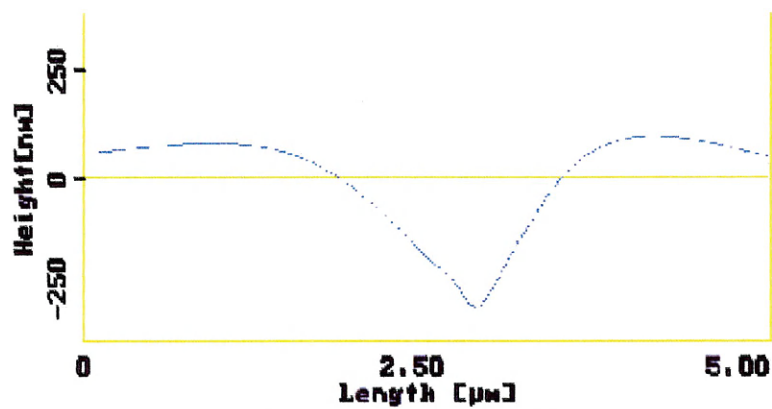


c) SEM

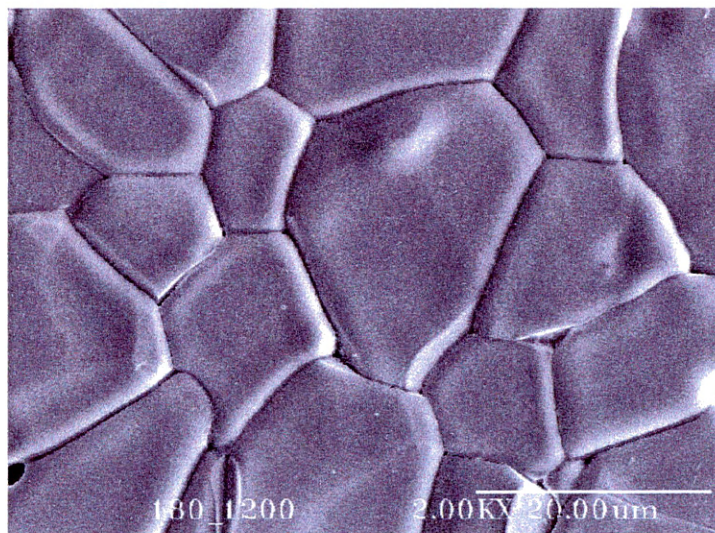
Air Etched Sample at 1473 K for 60 minutes



a) 3-dimensional AFM

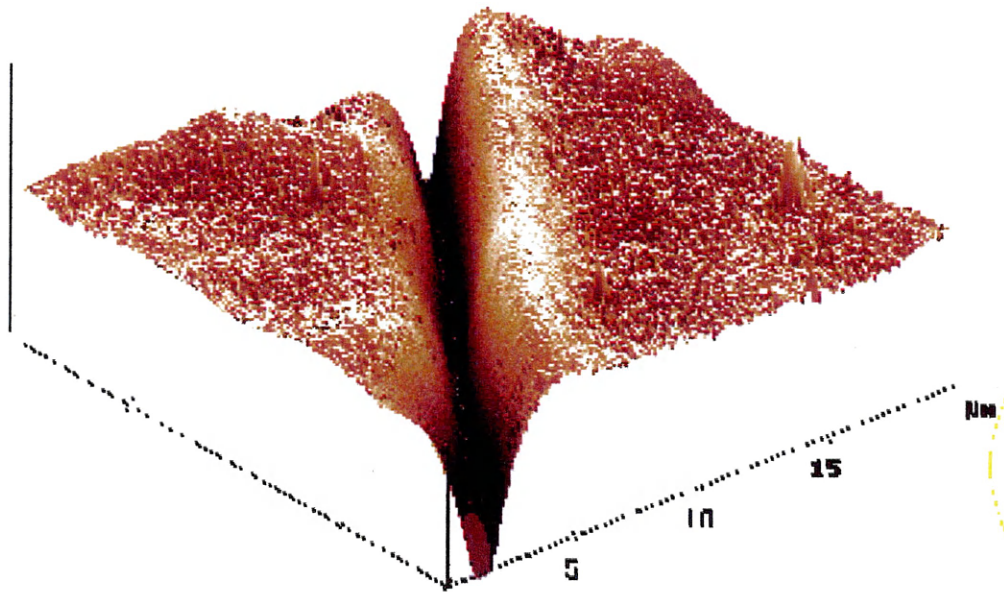


b) AFM groove profile

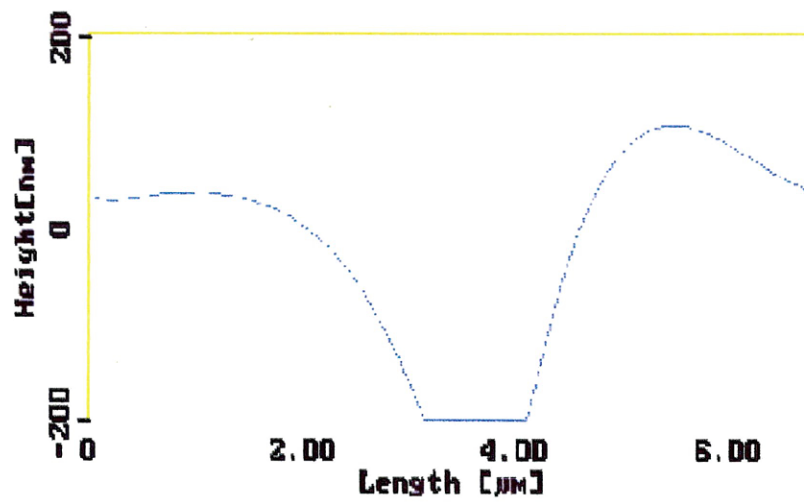


c) SEM

**Air Etched Sample at 1473 K for 180 minutes**



a) 3-dimensional AFM



b) AFM groove profile

Air Etched Sample at 1473 K for 540 minutes